TECHNISCHE UNIVERSITÄT WIEN
Vienna | Austria

DIPLOMARBEIT

Search for scalar top quark pair production in the dilepton final state in 13 TeV pp collisions with the CMS experiment

im Rahmen des Studiums

Technische Physik

eingereicht von

Markus Doppler BSc

Matrikelnummer 01325689

ausgeführt am Atominstitut der Technischen Universität Wien
in Verbindung mit dem Institut für Hochenergiephysik (HEPHY) der
Österreichischen Akademie der Wissenschaften

Betreuung

Betreuer: Univ.Prof. Dipl.-Phys. Dr.rer.nat. **Jochen Schieck**

Mitwirkung: Dipl.-Ing. Dr.techn. **Robert Schöfbeck**

Ort, Datum	Unterschrift Verfasser	Unterschrift Betreuer

Abstract

The Standard Model of particle physics is one of the most successful and well-tested scientific theories. It encapsulates humankinds' best understanding of how fundamental particles and forces are related to each other. However, the Standard Model of particle physics is found to be incomplete, as it does not provide explanations for cosmological observations such as dark matter and dark energy. Supersymmetry is a promising candidate for a theory beyond the Standard Model. For example, in many supersymmetric extensions of the Standard Model the lightest supersymmetric particle is weakly interacting and stable which makes it an excellent candidate for dark matter. So far, however, physics experiments have not been able to detect any supersymmetric signatures. A search for events with two charged leptons (electrons or muons) in the final state, arising from supersymmetric processes, is presented in this thesis. The analysis is based on proton-proton collision data taken by the CMS experiment at the CERN LHC in the operational period from 2016 to 2018 with a center of mass energy of 13 TeV. This amounts to an integrated luminosity of 137 fb^{-1}. In particular, scalar top quark pair production is considered. The tested models involve two jets originating from bottom quarks as well as the lightest neutralino in the final state, supplying a significant amount of missing transverse energy. The hypothetical supersymmetry events are efficiently separated from the dominant $t\bar{t}$ background with requirements on the significance of $p_{\text{T}}^{\text{miss}}$ and transverse mass variables. No significant deviation from the expected background is observed. The results are used to set limits on the production cross section of pair-produced top squarks. For the case where top squarks decay exclusively into a top quark and a neutralino, the exclusion limits on the mass of the lightest top squark are placed at up to 900 GeV and up to 440 GeV on the lightest neutralino at a 95% confidence level. For the decay involving an intermediate chargino, the mass limits at a 95% confidence level reach up to 850 GeV for the lightest top squark and up to 400 GeV for neutralino masses. For the top squark pair undergoing a cascade decay via charginos and sleptons, the exclusion limits reach up to 1.4 TeV for top squark masses and up to 900 GeV for the masses of the lightest neutralino at 95% confidence level. All in all, mass limits from previous analyses are improved by roughly 100 GeV.

Kurzfassung

Das Standardmodell der Teilchenphysik is eines der erfolgreichsten und am besten getesten Theorien der Wissenschaft. Es umfasst eine Beschreibung wie Elementarteilchen und fundamentale Kräfte miteinander wechselwirken. Das Standardmodell ist jedoch keineswegs vollständig, zumal es beispielsweise keine Erklärung zu den kosmologischen Beobachtungen von dunkler Materie und dunkler Energie liefert. Supersymmetrie ist eine vielversprechende Kandidatin für eine Theorie für Physik jenseits des Standardmodells. Beispielsweise stellt sich in vielen supersymmetrischen Erweiterungen des Standardmodells das leichteste supersymmetrische Teilchen als schwach wechselwirkend und stabil heraus, was es zu einem hervorragenden Kandidaten für dunkle Materie macht. Zum heutigen Stand ist es jedoch noch keinem physikalischen Experiment gelungen Anzeichen für Supersymmetrie zu finden. In dieser Arbeit wird eine Suche nach Ereignissen, die von supersymmetrischen Prozessen herrühren, mit zwei geladenen Leptonen (Elektronen oder Myonen) im Endzustand präsentiert. Die Analyse basiert auf Daten von Proton-Proton Kollisionen, die von 2016 bis 2018 vom CMS Experiment am CERN LHC bei einer Schwerpunktsenergie von 13 TeV aufgenommen worden sind. Diese Datenmenge umfasst eine integrierte Luminosität von 137 fb^{-1}. Im Speziellen wird skalare Top-Quark Paarproduktion untersucht. Die getesteten Modelle umfassen jeweils zwei Teilchenjets, die von Bottom-Quarks ausgehen, sowie das leichteste Neutralino im Endzustand, das eine beachtliche Menge an fehlender transverseller Energie mit sich bringt. Die hypothetischen supersymmetrischen Ereignisse werden äußerst effektiv vom dominierenden $t\bar{t}$-Hintergrund getrennt. Dies passiert mittels Bedingungen an die $p_{\text{T}}^{\text{miss}}$-Signifikanz und transverselle Massenvariablen. Alles in allem werden keine signifikanten Unterschiede vom erwarteten Standardmodell-Hintergrund beobachtet. Die Resultate werden im Anschluss dafür verwendet, um Grenzwerte für die Produktionswirkungsquerschnitte von paarproduzierten Top-Squarks zu bestimmen. Für den Fall, wo ein skalares Top-Quark in ein Top-Quark und ein Neutralino zerfällt, ergeben sich für ein 95%-Konfidenzintervall Grenzwerte, die die leichtesten Top-Squarks mit Massen bis zu 900 GeV und Neutralinomassen bis zu 440 GeV ausschließen. Ein Zerfall, der außerdem ein Chargino als Zwischenzustand enthält, bekommt Massengrenzwerte von bis zu 850 GeV für das Top-Squark und für das Neutralino maximal 400 GeV zugeschrieben. Falls ein Top-Squark-Paar in einer Kaskade mittels Charginos und Sleptonen zerfällt, reichen die Grenzwerte bis 1.4 TeV für Top-Squark-Massen und bis 900 GeV für Neutralinomassen. Zusammenfassend können die Massen-Grenzwerte von vorausgehenden Analysen um ungefähr 100 GeV verbessert werden.

Contents

1 Introduction **1**

1.1 Theoretical framework of the Standard Model 2

1.1.1 Electromagnetic interaction 5

1.1.2 Strong interaction 6

1.1.3 Weak interaction 7

1.1.4 Electroweak unification 8

1.1.5 Higgs mechanism 9

1.2 Shortcomings of the Standard Model 11

1.3 Supersymmetry 12

1.3.1 Solution to the hierarchy problem 12

1.3.2 Minimal Supersymmetric Standard Model 13

1.3.3 Dark matter candidate 15

1.3.4 Unification of gauge couplings 16

1.3.5 Search for top squarks 16

1.3.6 Simplified models 17

2 Large Hadron Collider **21**

2.1 CERN's accelerator complex 21

2.2 LHC magnets 22

2.3 LHC physics 24

3 Compact Muon Solenoid **25**

3.1 Superconducting solenoid magnet 27

3.2 Pixel and Strip Trackers 28

3.3 Electromagnetic Calorimeter 29

3.4 Hadronic Calorimeter . . . 31
3.5 Muon system . . . 32
3.6 Trigger and data acquisition system . . . 32

4 Reconstructing physics objects **35**
4.1 Muons . . . 36
4.2 Electrons and photons . . . 36
4.3 Jets . . . 37
4.3.1 b-tagged jets . . . 38
4.4 Missing transverse energy . . . 38

5 Search for supersymmetry in dilepton final state **41**
5.1 Data and simulated samples . . . 41
5.2 Event selection . . . 45
5.2.1 Search strategy . . . 45
5.2.2 Preselection . . . 56
5.3 Signal and control regions . . . 59
5.4 Systematic uncertainties . . . 61
5.5 Background estimation . . . 64
5.5.1 $t\bar{t}$ background . . . 65
5.5.2 Drell-Yan and Multiboson background . . . 72
5.5.3 $t\bar{t} + Z$ background . . . 73
5.5.4 Rare backgrounds . . . 75
5.6 Results . . . 76
5.6.1 Statistical methods . . . 76
5.6.2 Control region fits . . . 78
5.6.3 Combined fit and limit setting . . . 80
5.6.4 Exclusion limits . . . 83
5.6.5 Comparison with other results . . . 85

6 Conclusion **87**

A Background modelling check in sideband selections **89**

B Pulls, nuisances and correlations **91**

List of Figures **95**

List of Tables **99**

Bibliography **101**

1 Introduction

Humankind has been interested in the fundamental structure of matter for a long time. This dates back as far as the fifth century BC when the ancient Greek philosophers Leucippus and Democritus brought forward their idea that matter is comprised of elementary particles. Over the centuries – especially during the last one hundred years – physicists have made plentiful discoveries and refined their theories accordingly. The result is a remarkable insight into the fundamental structure of matter. Everything in the universe is thought to be made from a few basic building blocks, still taking up the age-old notion of elementary particles. The interaction between those fundamental particles is governed by four fundamental forces: electromagnetism, the weak and strong interaction, and gravity. The Standard Model (SM) of particle physics is humankind's most successful theory which describes three out of the four fundamental forces to great accuracy. Besides, it classifies all known elementary particles. On 4th July 2012 a breakthrough discovery was announced by the ATLAS and CMS experiments at CERN. The collaborations had detected the last remaining undiscovered piece of the SM, the Higgs boson, with a mass of roughly 125 GeV [1, 2]. Since the SM has been developed in the early 1970s, it has successfully explained almost all experimental results and precisely predicted a wide variety of phenomena. Indeed, it is now an established, well-tested theory of interactions between fundamental particles.

However, the SM is not a complete theory, in the sense that it does not describe all phenomena observed in our universe. First of all, it does not incorporate gravitation, which is described by the theory of general relativity. As the SM is formulated as a quantum field theory (QFT), one would like to also phrase a theory of gravity in this framework. Yet, when applying the usual prescriptions of QFTs to the gravitational force one encounters non-renormalisabilities, i.e. infinite values for observable properties such as particle masses. Therefore, joining the phenomena described by the SM and gravity together within a single framework is still an active field of research.

Furthermore, observations of the cosmic microwave background show that matter, as it is described by the SM, makes up only $(4.93 \pm 0.06)\%$ of the matter-energy content of the universe, according to the latest results by the Planck Consortium [3]. The nature of the remaining matter and energy content of the universe is largely unknown, with $(26.42 \pm 0.36)\%$ coming from dark matter and dark energy comprising the largest part at $(68.65 \pm 0.7)\%$ [4, 3]. In addition, the observation of a neutrino mass [5, 6] stands in contradiction to the SM neutrino which is massless.

Over the years, many extensions of the SM have been proposed in an attempt to rid the SM of its problems and provide a unified theory of all four fundamental forces. One proposed theory that can simultaneously solve some of the SM's problems is supersymmetry (SUSY). Throughout this chapter an overview of the theoretical formulation of the SM as a QFT, the problems that arise in the SM, as well as an introduction to SUSY and its implications will be given.

1.1 Theoretical framework of the Standard Model

The SM of particle physics is formulated as a relativistic QFT and is based on local gauge symmetries. More specifically, the SM is invariant under local gauge transformations of the symmetry group $\mathrm{SU(3)_C} \otimes \mathrm{SU(2)_L} \otimes \mathrm{U(1)}_Y$. This successfully describes the fundamental interactions of particles, i.e. the strong, weak and the electromagnetic interactions, at the highest energy scales probed by particle physics experiments to date with the exception of gravity. Gravitational interactions are predicted to be negligible at microscopic scales. Therefore, their missing description in the SM is of no qualitative concern in particle physics.

The theoretical framework of the SM relies on the concept of gauge invariance. Gauge invariance originates from the assumption that the laws of physics should not depend on arbitrarily chosen coordinate systems or gauges. Assuming, for instance, a Lagrangian formulation, the invariance of a free QFT under some local gauge transformation introduces new interaction terms containing the gauge fields that correspond to the generators of the gauge symmetry. This way, the gauge fields that describe the strong, weak and electromagnetic interactions are introduced, as will be described in some detail in the following. Furthermore, Noether's theorem states [7] that for every local symmetry of a (field) theory there exists a conserved current. Such a current is intimately linked to a particle's charge. As a result, different fields can be organised with respect to their charges, and their interactions can be determined from the underlying symmetries.

Experimental observations [8, 9, 10, 11] show that the W and Z bosons, the mediators of the weak force, have large masses. Photons and gluons, on the other hand, are experimentally compatible with being massless. As introduced above, gauge invariance results in the gauge fields being massless. Therefore, in order to explain the observation of massive gauge bosons, the SM incorporates the spontaneous breaking of electroweak symmetry. However, fundamental masses of vector bosons are no longer gauge invariant. Furthermore, the spontaneous symmetry breaking mechanism in the SM not only provides mass for the gauge bosons, but also gives mass to fermions. Spontaneous symmetry breaking of the electroweak symmetry also brings about a special particle, the Higgs boson, which was theoretically predicted and has finally been discovered in 2012 at CERN's LHC.

One can divide the SM particles into two categories according to their spin: fermions, which are the matter particles and bosons, that carry the forces between them. Fermions

are described by half integer spin fields and accordingly obey Fermi-Dirac statistics. All SM fermions are spin-$\frac{1}{2}$ particles. Bosons, on the other hand, are integer spin fields and hence obey Bose-Einstein statistics. All SM gauge fields are spin-1 vector bosons, while the only spin-0 scalar boson in the SM is the Higgs boson. A summary of all SM bosons is displayed in Fig. 1.1.

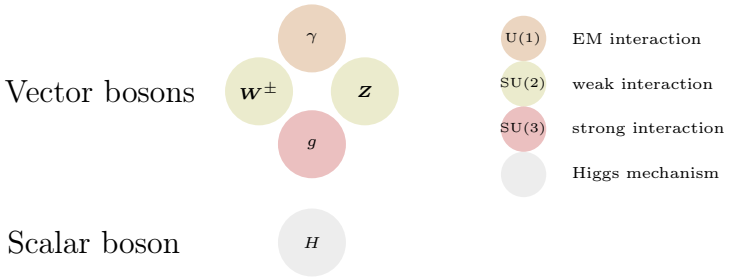

Figure 1.1: SM gauge bosons and the interactions they mediate.

The fundamental interactions described in the SM are closely related to their corresponding symmetry group. In particular, the gauge bosons that mediate the interactions emerge as the generators of the symmetry group. The electromagnetic force is mediated by photons and is closely related to the group U(1). Since U(1) is a one dimensional group[1] there is only one boson responsible for this interaction, namely the photon. The symmetry group of the strong force is SU(3). Hence, there are eight vector bosons which mediate the strong force, which are called gluons. The strong interaction only applies to particles carrying colour charge, as will be discussed momentarily. The W and Z bosons are responsible for the weak force. They interact with weakly charged particles, which all fermions are in the SM. Since the gauge group of the weak interaction is SU(2), there are supposed to be three vector bosons, namely the neutral Z boson as well as the charged W^+ and W^- bosons. $W^\pm$ and Z bosons are the only vector bosons that carry mass, which is why the the weak interaction is very short ranged. Furthermore, the weak and electromagnetic forces can be unified in the SM, as will be discussed in Section 1.1.4.

The fermionic matter fields of the SM can be grouped into quarks and leptons. Furthermore, fermions form three generations of matter, where corresponding particles in different generations (i.e. each line in Fig. 1.2) possess the same kinds of charges with respect to the gauge fields with which they interact. Each generation of particles consists of a charged lepton, a neutrino, as well as an up-type and a down-type quark. Moreover, the masses of the particles increase with the generation. For reference, the masses of SM fermions and gauge bosons are displayed in Table 1.1. Antiparticles are denoted by a bar, e.g. $\bar{u}$ stands for the anti-up quark.

Quarks are massive particles that carry electric, weak, and colour charges. Therefore, quarks are the only type of elementary particles subject to all fundamental forces. The

[1]The one dimensional unitary group U(1) has one generator. An n dimensional special unitary group SU(n) has $n^2 - 1$ generators, which corresponds to the dimension of the adjoint representation of the group [12].

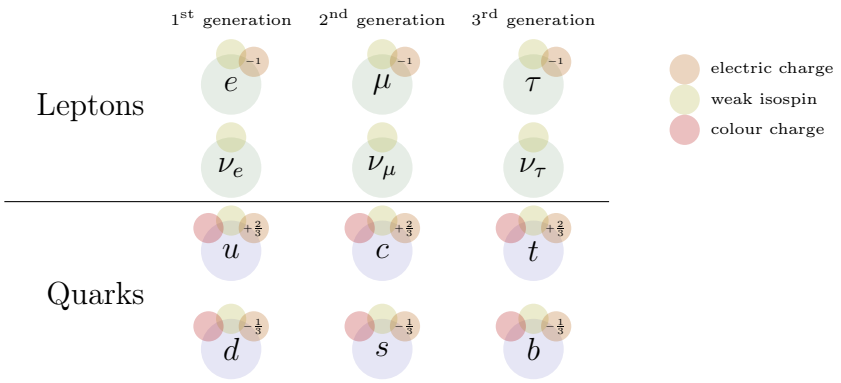

Figure 1.2: Different generations of SM fermions. The small coloured circles symbolise each particle's charges under the fundamental forces in the SM.

first generation quarks, i.e. up and down quarks, form the stable hadrons in the nuclei of atoms. Leptons are divided into charged and neutral (under the electromagnetic interaction) leptons. Charged leptons, i.e. the electron, muon and tau lepton, are often just denoted by "leptons", whereas neutral leptons are called "neutrinos". All leptons are massive and participate in the weak interaction. However, in the SM neutrinos are massless. This is a reasonable approximation, as neutrino masses are very small compared to the other particles in the SM, yet neutrino masses and their origin are still unknown. Electrons, the lightest (charged) leptons, are found in atoms.

Table 1.1: SM particle masses and their electric charges [13].

particle	**mass**		**charge**
u	$2.2^{+0.5}_{-0.4}$	MeV	$+\frac{2}{3}e$
d	$4.7^{+0.5}_{-0.3}$	MeV	$-\frac{1}{3}e$
s	95^{+9}_{-3}	MeV	$-\frac{1}{3}e$
c	$1.275^{+0.025}_{-0.035}$	GeV	$+\frac{2}{3}e$
b	$4.18^{+0.04}_{-0.03}$	GeV	$-\frac{1}{3}e$
t	173 ± 0.4	GeV	$+\frac{2}{3}e$
e	0.511	MeV	$1e$
μ	105.658	MeV	$1e$
τ	1776.86 ± 0.12	MeV	$1e$
ν_e	$0.02 - 2$	eV	0
ν_μ	$0.02 - 2$	eV	0
ν_τ	$0.02 - 2$	eV	0
Z	91.188 ± 0.002	GeV	0
W	80.379 ± 0.012	GeV	$\pm 1e$
g	0		0
γ	0		0
H	125.18 ± 0.16	GeV	0

1.1.1 Electromagnetic interaction

The electromagnetic interaction is described within the framework of quantum electrodynamics (QED). A fermion with mass m is described by a Dirac spinor ψ. The equation of motion for spin-$\frac{1}{2}$ fermions is given by the Dirac equation[2],

$$(i\gamma^\mu\partial_\mu - m)\,\psi = 0. \tag{1.1}$$

Since Eq. (1.1) is essentially the Euler-Lagrange equation, the Lagrangian density of the free field theory is given by

$$\mathcal{L}_{\text{free}} = \bar{\psi}\,(i\gamma^\mu\partial_\mu - m)\,\psi, \tag{1.2}$$

with $\bar{\psi} = \psi^\dagger\gamma^0$ being the conjugate field. This Lagrangian density is invariant under global U(1) transformations, i.e.

$$\psi(x) \to \psi'(x) = \mathrm{e}^{-iq\theta}\psi(x),$$

where q and θ are real constants.

Since the choice of the reference point for a coordinate system must not change the physics, one requires local U(1) gauge invariance of Eq. (1.2). A local gauge transformation, where $\theta \equiv \theta(x)$ depends on the space-time coordinates, would produce a new term in the Dirac equation, hence breaking the local symmetry. In order to offset that term, one introduces a covariant derivative

$$\mathcal{D}_\mu = \partial_\mu + iqA_\mu \qquad (\text{with } \; (\mathcal{D}_\mu\psi)' = \mathrm{e}^{-iq\theta(x)}\mathcal{D}_\mu\psi)$$

that replaces the ordinary derivative ∂_μ in Eqs. (1.1) and (1.2). The constant q is now called a coupling constant and A_μ is a spin-1 gauge field that describes the electromagnetic field. The behaviour of the gauge field under a local U(1) transformation is given by

$$A_\mu(x) \to A'_\mu(x) = A_\mu(x) + \partial_\mu\theta(x).$$

Substituting in the covariant derivative in Eq. (1.2) as well as adding the terms for the massless photon field, one obtains the full QED Lagrangian density

$$\mathcal{L}_{\text{QED}} = \bar{\psi}\,(i\gamma^\mu\mathcal{D}_\mu - m)\,\psi - \frac{1}{4}F_{\mu\nu}F^{\mu\nu} - J^\mu_{\text{ext}}A_\mu. \tag{1.3}$$

The field strength tensor $F_{\mu\nu}$ is defined as $F_{\mu\nu} = \partial_\mu A_\nu - \partial_\nu A_\mu$ and the last term corresponds to external currents J^μ_{ext}. It is especially noteworthy that, expanding the covariant derivative, there is a term $q\bar{\psi}\gamma^\mu A_\mu\psi$ in Eq. (1.3) which indicates the interaction between the fermion field and gauge field.

The Euler-Lagrange equations of Eq. (1.3) with respect to electromagnetic field A_μ and the conjugate fermion field $\bar{\psi}$ yield the inhomogeneous Maxwell equations and the

[2]Throughout this chapter natural units are used, i.e. $\hbar = c = 1$. Besides, the space-time metric is $\eta_{\mu\nu} = \text{diag}(1, -1, -1, -1)$.

Dirac equation in the electromagnetic field, respectively. Furthermore, since Eq. (1.3) is now invariant under the local U(1) gauge symmetry, there is a conserved current of the form

$$J^\mu = q\bar{\psi}\gamma_\mu\psi + J^\mu_{\text{ext}},$$

as implied by Noether's theorem. The coupling constant q is defined by the fermion's charge, e.g. for electrons $q = -e$.

1.1.2 Strong interaction

Quantum chromodynamics (QCD) is the gauge theory which describes the interactions between quarks. Quarks have colour charge[3] which is mediated by gluons. The symmetry group of QCD is SU(3), which is a non-abelian group (i.e. the generators of the group do not commute which each other). This has the consequence that gluons not only interact with quarks but also among themselves. Furthermore, SU(3) has eight generators which correspond to eight colour degrees of freedom.

The Lagrangian density for the dynamics of the six quark flavours (f $= u, d, c, s, t, b$) reads

$$\mathcal{L}_{\text{quark}} = \sum_{\text{f}=1}^{6} \bar{q}_\text{f} \left(i\gamma^\mu \mathcal{D}_\mu - m_\text{f}\right) q_\text{f} \tag{1.4}$$

and is invariant under local SU(3) transformations. The covariant derivative is defined as

$$\mathcal{D}_\mu = \partial_\mu + i g_\text{s} \boldsymbol{G}_\mu, \tag{1.5}$$

where g_s is the strong coupling constant and $\boldsymbol{G}_\mu \in$ SU(3) the gauge field. The latter can be expanded in terms of the generators F^a of SU(3) and the corresponding gluon fields G^a_μ as

$$\boldsymbol{G}_\mu = \sum_{a=1}^{8} G^a_\mu F^a. \tag{1.6}$$

Besides, the generators F^a and the quark fields q_f can be respresented as 3×3 matrices and three-vectors in colour space, respectively. SU(3) being a non-abelian group, its generators fulfill the Lie algebra

$$[F_a, F_b] = i f_{abc} F_c,$$

with the structure constants f_{abc}. The gluonic part of the QCD Lagrangian density is

$$\mathcal{L}_{\text{gluon}} = -\frac{1}{4} \sum_{a=1}^{8} G^a_{\mu\nu} G^{a\,\mu\nu}. \tag{1.7}$$

[3]Of course, this is not a *real* colour in the optical sense. It is merely a good analogy, since there are three different colour charges akin the three primary colours (red, green and blue) in optics. Composite particles (made up of coloured ones) are found to always be colourless. This can be achieved by having three differently coloured particles or a colour and anti-colour particle.

Here, $G^a_{\mu\nu}$ are the gluon field strength tensors, given by

$$G^a_{\mu\nu} = \partial_\mu G^a_\nu - \partial_\nu G^a_\mu + g_\mathrm{s} f^{abc} G^b_\mu G^c_\nu. \tag{1.8}$$

The full QCD Lagrangian density is then simply the sum of the quark and gluon parts (Eqs. (1.4) and (1.7), respectively)

$$\mathcal{L}_\mathrm{QCD} = \mathcal{L}_\mathrm{quark} + \mathcal{L}_\mathrm{gluon}. \tag{1.9}$$

It is worth noting that the interaction between quarks and gluons is decribed by a term of the form $g_\mathrm{s}\bar{q}_\mathrm{f}\gamma^\mu \boldsymbol{G}_\mu q_\mathrm{f}$ resulting from the covariant derivative in Eq. (1.4). The gluon-gluon interaction, on the other hand, comes about due to the third term $g_\mathrm{s} f^{abc} G^b_\mu G^c_\nu$ in Eq. (1.8) since SU(3), being non-abelian, has non-vanishing structure constants.

The most alluring feature of QCD is undoubtably the mechanism of quark confinement. Hadrons found in nature, which are particles formed as a bound state of quarks, are colourless. The two most prominent types of hadrons are mesons (bound state of a quark-antiquark pair) and baryons (contain three valence quarks). Colour confinement is the reason that the strong interaction has a very short range despite gluons being considered massless. If two quarks are spatially separated, new hadrons are formed. This process is called hadronisation. At very short ranges, on the other hand, the interaction between quarks actually gets smaller, a feature termed asymptotic freedom. In this high-energy regime, perturbative calculations can be performed [14, 15].

1.1.3 Weak interaction

The mediators of the weak interaction, i.e. the $W^\pm$ and Z bosons, are experimentally found to be massive. For that reason, the formulation of a gauge invariant Lagrangian is not quite as straight forward as for QED and QCD, since a mass term for the gauge bosons would break gauge invariance. Furthermore, only left-handed fermions and right-handed anti-fermions interact with the W^+ and W^- bosons. Dirac fermions ψ can be projected onto their left-handed and right-handed components via

$$\psi_L = \frac{1}{2}\left(1 - \gamma^5\right)\psi\,, \text{ and}$$
$$\psi_R = \frac{1}{2}\left(1 + \gamma^5\right)\psi\,,$$

where $\gamma^5 := i\gamma^0\gamma^1\gamma^2\gamma^3$. After discussing these peculiarities of the weak interaction, an overview of the unification of electromagnetism and the weak interaction will be given, in conjunction with the Higgs mechanism, which provides masses for the weak gauge bosons, quarks, and leptons.

Left-handed SM matter multipletts are charged under SU(2). The third component T_3 of the weak isospin T serves as a quantum number (analogous to electric charge in QED or colour charge in QCD) and governs how that particle behaves under the weak

interaction. Another important property that connects charge Q and weak isospin T_3 of a particle is the weak hypercharge Y which defined as

$$Y = Q - T_3.$$

The left-handed fermions are described by $\mathrm{SU}(2)_\mathrm{L}$ doublets of the form

$$\psi_\mathrm{L} = \begin{pmatrix} \text{weak isospin } +\frac{1}{2} \\ \text{weak isospin } -\frac{1}{2} \end{pmatrix}, \text{ such as } \begin{pmatrix} u_\mathrm{L} \\ d_\mathrm{L} \end{pmatrix}, \begin{pmatrix} c_\mathrm{L} \\ s_\mathrm{L} \end{pmatrix}, \begin{pmatrix} t_\mathrm{L} \\ b_\mathrm{L} \end{pmatrix}, \begin{pmatrix} \nu_e \\ e_\mathrm{L} \end{pmatrix}, \begin{pmatrix} \nu_\mu \\ \mu_\mathrm{L} \end{pmatrix}, \begin{pmatrix} \nu_\tau \\ \tau_\mathrm{L} \end{pmatrix},$$

with $T_3 = \pm\frac{1}{2}$ for the respective components. Right-handed fermions, which are neutral under SU(2), form singlets ($T_3 = 0$), i.e.

$$\psi_\mathrm{R} = u_\mathrm{R},\ d_\mathrm{R},\ c_\mathrm{R},\ s_\mathrm{R},\ t_\mathrm{R},\ b_\mathrm{R},\ e_\mathrm{R},\ \mu_\mathrm{R},\ \tau_\mathrm{R},$$

with the exception of right handed neutrinos that apparently do not exist in nature. Furthermore, W^+ and W^- bosons carry a weak isospin of $T_3 = \pm 1$, respectively. The Z^0 boson and the photon have $T_3 = 0$. In any given interaction, weak isospin is conserved. Hence, a quark never decays through the weak interaction into a quark of the same weak isospin. A valid decay, for instance, is a down quark decaying into an up quark by sending off a W^- boson.

Certain weak phenomena can be described in the low energy limit, such as the β decay, muon decay and neutrino scattering [16]. For these cases effective Lagrangians suffice for the mathematical description, in particular the weak force is then described by a two-vector current interaction. This can either be a neutral current interaction involving a Z boson, or a charged current interaction, for instance, changing the flavour of quarks via $W^\pm$ bosons.

1.1.4 Electroweak unification

It turns out that the electromagnetic and weak interaction can be unified with $\mathrm{SU}(2)_\mathrm{L} \times \mathrm{U}(1)_Y$ as the gauge group. Assuming massless fermions, the free Lagrangian for leptons or quarks of a given family can be expressed as

$$\mathcal{L}_\text{fermion} = \bar{\psi}_\mathrm{L} \gamma_\mu \mathcal{D}^\mu \psi_\mathrm{L} + \bar{\psi}_\mathrm{R} \gamma_\mu \mathcal{D}^\mu \psi_\mathrm{R}, \tag{1.10}$$

where ψ_L is a doublet and ψ_L a singlet. The respective covariant derivatives are defined as such

$$\mathcal{D}_\mu \psi_\mathrm{L} = \left(\partial_\mu + \frac{i}{2} g\, \boldsymbol{W}_\mu + \frac{i}{2} g' B_\mu \right) \psi_\mathrm{L}, \tag{1.11}$$

$$\mathcal{D}_\mu \psi_\mathrm{R} = \left(\partial_\mu + \frac{i}{2} g' B_\mu \right) \psi_\mathrm{R}, \tag{1.12}$$

using the two fields $\boldsymbol{W}_\mu \in \mathrm{SU}(2)_\mathrm{L}$ and $B_\mu \in \mathrm{U}(1)_Y$. More specifically, $\boldsymbol{W}_\mu$ can be expanded in terms of the generators σ^a of SU(2), as

$$\boldsymbol{W}_\mu = \sum_{a=1}^{3} W_\mu^a \cdot \sigma^a.$$

The full electroweak Lagrangian density then contains in addition to Eq. (1.10) the dynamic terms for the gauge fields

$$\mathcal{L}_{\text{electroweak}} = \mathcal{L}_{\text{fermion}} - \frac{1}{4}\sum_{a=1}^{3} W^a_{\mu\nu} W^{a\,\mu\nu} - \frac{1}{4} B_{\mu\nu} B^{\mu\nu}, \tag{1.13}$$

where the $W^a_{\mu\nu}$ and $B_{\mu\nu}$ are the corresponding field strength tensors. Note that the three $\mathrm{SU}(2)_\mathrm{L}$ gauge bosons W^1, W^2, and W^3 couple to the weak isospin T_3 and the $\mathrm{U}(1)_Y$ gauge boson couples to hypercharge Y.

The $W^\pm$ bosons, which contribute to the charged current terms, can then be constructed as

$$W^\pm_\mu = \frac{1}{\sqrt{2}} \left(W^1_\mu \mp W^2_\mu \right).$$

The photon field A_μ and the Z boson field, which form the neutral current terms, employ a more complicated kind of mixing of the remaining gauge field components

$$\begin{pmatrix} A_\mu \\ Z_\mu \end{pmatrix} = \begin{pmatrix} \cos\theta_\mathrm{w} & \sin\theta_\mathrm{w} \\ -\sin\theta_\mathrm{w} & \cos\theta_\mathrm{w} \end{pmatrix} \begin{pmatrix} B_\mu \\ W^3_\mu \end{pmatrix},$$

with the weak mixing angle (or Weinberg angle) θ_w. This was shown by Glashow, Salam and Weinberg in [17, 18, 19].

So far, fermions have been considered massless. A fermion mass term of the form $-m\bar{\psi}_\mathrm{L}\psi_\mathrm{R}$ in Eq. (1.13) would break the $\mathrm{SU}(2)_\mathrm{L}$ symmetry, since doublets and singlets transform differently under the gauge group. The Higgs mechanism, which will be described in the next section, will provide mass for these fermions and also for the weak gauge bosons.

1.1.5 Higgs mechanism

The Higgs or BEH mechanism (named after Robert Brout, François Englert, and Peter Higgs) [20, 21] describes the breaking of the symmetry of the underlying gauge group of the electroweak interaction and in turn provides mass terms for the bosons. To spontaneously break the symmetry, a complex scalar field $\Phi \in \mathrm{SU}(2)_\mathrm{L}$ is introduced

$$\Phi = \begin{pmatrix} \phi_+ \\ \phi_0 \end{pmatrix}. \tag{1.14}$$

The scalar Higgs part of the Lagrangian density is given by

$$\mathcal{L}_{\text{Higgs}} = \left(\mathcal{D}_\mu \Phi^\dagger \right) \mathcal{D}^\mu \Phi - V\left(\Phi^\dagger \Phi \right). \tag{1.15}$$

The covariant derivative is defined analogous to Eq. (1.11) as

$$\mathcal{D}_\mu \Phi = \left(\partial_\mu + \frac{i}{2} g\, \boldsymbol{W}_\mu + \frac{i}{2} g' B_\mu \right) \Phi, \tag{1.16}$$

with the $\mathrm{SU(2)_L}$ gauge field $\boldsymbol{W}_\mu$, the $\mathrm{U(1)}_Y$ gauge boson B_μ and the respective coupling constants g and g'. Furthermore, the potential in Eq. (1.15) must be of the general form

$$V\left(\Phi^\dagger\Phi\right) = -\mu^2\,\Phi^\dagger\Phi + \lambda\left(\Phi^\dagger\Phi\right)^2,$$

with the real constants μ^2 and λ, in order to guarantee renormalisability of the theory and $\mathrm{SU(2)_L}\otimes\mathrm{U(1)}_Y$ invariance. It turns out that by requiring $\lambda > 0$ and $\mu^2 > 0$, the scalar field acquires a non trivial vacuum expectation value

$$\langle\Phi\rangle = \sqrt{\frac{\mu^2}{2\lambda}} \equiv \frac{v}{\sqrt{2}},$$

which spontaneously breaks the symmetry. In this case, the potential somewhat resembles the shape of a mexican hat with a degenerate ground state in the gouge of the hat's brim. Using gauge freedom, one can set

$$\langle\Phi\rangle = \frac{1}{\sqrt{2}}\begin{pmatrix}0\\ v\end{pmatrix},$$

which compared with Eq. (1.14) implies the component ϕ_0 to be electrically neutral, since only a neutral scalar field can aquire a vacuum expectation value, i.e. $Q(\Phi) = 0$, and electric charge is conserved. Therefore, despite the sponteous breaking [20, 21] of the $\mathrm{SU(2)_L}\otimes\mathrm{U(1)}_Y$ symmetry, electromagnetism, which is associated with $\mathrm{U(1)}_Q$, remains unbroken. Inserting the expansion

$$\Phi = \frac{1}{\sqrt{2}}\begin{pmatrix}0\\ v+h\end{pmatrix}, \tag{1.17}$$

with the real Higgs field h into Eq. (1.15) one can read off the boson masses. The W mass is $m_W = \frac{g\,v}{2}$, while the Z boson mass results in $m_Z = \frac{v}{2}\sqrt{g^2+g'^2}$. The photon is massless.

The last missing piece are the fermion masses. Fermions acquire mass via so-called Yukawa couplings between the Higgs field Φ and the fermions. For example, the Yukawa part of the Lagrangian density for the first fermion generation can be written as

$$\mathcal{L}_{\text{Yukawa}} = c_e\,\psi_{\mathrm{L}}^\dagger\Phi e_{\mathrm{R}} + c_u\,q_{\mathrm{L}}^\dagger\tilde{\Phi}u_{\mathrm{R}} + c_d\,q_{\mathrm{L}}^\dagger\Phi d_{\mathrm{R}} + \text{h.c.},$$

with $\Phi = \binom{\phi_+}{\phi_0}$, $\tilde{\Phi} = \binom{\phi_0^*}{-\phi_-}$, $\psi_{\mathrm{L}} = \binom{\nu_e}{e_{\mathrm{L}}}$, $q_{\mathrm{L}} = \binom{u_{\mathrm{L}}}{d_{\mathrm{L}}}$ and the coupling constants c_e, c_u, and c_d to the Higgs field. Choosing a gauge for the Higgs field, e.g. as in Eq. (1.17), one can read off the fermion masses as

$$m_i = -\frac{c_i\,v}{\sqrt{2}} \quad \text{with } i = e, u, d.$$

Note that, as the neutrino has no right-handed partner in the SM, it can not acquire a mass term through Yukawa coupling.

Summing up, the electromagnetic and weak interaction can be unified using local gauge invariance and spontaneous symmetry breaking. The $W^\pm$, Z vector bosons and

fermions (except neutrinos) of the SM acquire mass from coupling to the Higgs field. As a result the full SM Lagrangian density is given by

$$\mathcal{L}_{\mathrm{SM}} = \mathcal{L}_{\mathrm{QCD}} + \mathcal{L}_{\mathrm{electroweak}} + \mathcal{L}_{\mathrm{Higgs}} + \mathcal{L}_{\mathrm{Yukawa}}.$$

1.2 Shortcomings of the Standard Model

The SM predictions very accurately describe observations at the high energy physics experiments conducted over the last decades. Observed quantities, such as various production cross sections of particles or the magnetic dipole moment of the electron [22], match the predicted values from SM calculations with an outstanding precision. There are, however, unanswered questions the SM does not address as well as limitations of the theory, which will be the topic of the rest of the chapter. These problems suggest that the SM can only be an effective field theory (EFT). If that is the case, the SM has to be replaced by a more fundamental theory at energy scales much higher than the electroweak scale. After discussing some problems with the SM, solutions in the context of supersymmetry will be presented in the next chapter.

The observation of a neutrino mass [5] by the SuperKamiokande collaboration demonstrates that the SM is incomplete, since within the context of SM, neutrinos are massless. To provide neutrino mass terms, an extension of the SM Lagrangian density is needed.

Another failure is that the SM does not provide for a dark matter candidate. The power spectrum of the cosmic microwave background, rotation curves of galaxies, and the effect of gravitational lensing of distant objects indicate the existence of an unknown mass source [23, 24, 25]. Since this source not correspond to any of the known forms of matter described by the SM, it is known as dark matter. Recent measurements by the Planck Collaboration [3] declare the relative contribution of dark matter density to be about 26% of the total matter and energy content of the universe. That means the SM describes only about 19% of the total mass in the universe that is ordinary matter. Furthermore, the Planck Collaboration specifies that roughly 69% of the current energy content of the universe are an unknown form of energy referred to as dark energy. Dark energy is responsible for the acceleration in the expansion of the universe. However, to date, neither dark matter nor dark energy has been directly detected in physics experiments.

The SM also cannot fully explain the asymmetry between matter and antimatter in the universe. This imbalance is determined from the power spectrum of the CMB and the abundance of light elements in the universe.

Furthermore, the SM obviously does not incorporate a description of the gravitational interaction. Especially at high energies close to the planck mass, quantum gravitational effects become increasingly important. It is therefore essential for a theory beyond the SM (BSM) to be able to explain gravity within the same framework as the SM.

Another problem with the SM, if accepted as an EFT, is that the Higgs mechanism

gives rise to the hierarchy problem (naturalness problem). This issue refers to the fact that the observed mass of the Higgs boson is roughly 16 orders of magnitude smaller than the value expected from the cutoff scale Λ at which the SM EFT necessarily becomes invalid. A fine-tuned renormalisation has to stabilise the Higgs mass.

1.3 Supersymmetry

SUSY introduces an additional symmetry which relates fermionic states to bosonic states with an operator Q, such that

$$\begin{aligned} Q|\text{boson}\rangle &= |\text{fermion}\rangle, \\ Q|\text{fermion}\rangle &= |\text{boson}\rangle. \end{aligned}$$

While the SM symmetries are gauge symmetries that involve transformations of the fields themselves, SUSY is a spacetime symmetry. The operator Q and its hermitian conjugate $Q^\dagger$ are fermionic operators and as such carry spin angular momentum 1/2. Therefore, Q turns fermions with spin 1/2 into spin 0 scalars and bosons with spin 1 into spin 1/2 fermions. [26]

SUSY has interesting properties that will be discussed in the following.

1.3.1 Solution to the hierarchy problem

SUSY can offer a natural solution to the electroweak hierarchy problem, which was discussed at the end of Section 1.2. The quantum corrections to the mass of the Higgs boson Δm_H are predominately coming from fermion and scalar loops. The corresponding Feynman diagrams are pictured in Fig. 1.3. Assuming a coupling term

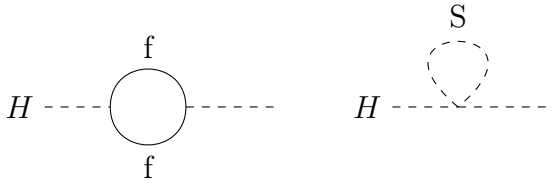

(a) Dirac fermion f (b) scalar S

Figure 1.3: One-loop corrections to the Higgs mass parameter Δm_H^2.

like $-\lambda_\text{f} \bar{\text{f}}\, H\, \text{f}$ in the Langrangian density with a Yukawa coupling λ_f, the contribution of a Dirac fermion f to the Higgs mass correction (Fig. 1.3a) is [26]

$$\Delta m_H^2 = \frac{|\lambda_\text{f}|^2}{8\pi^2}\left[-\Lambda_\text{UV}^2 + 3m_\text{f} \ln\left(\frac{\Lambda_\text{UV}}{m_\text{f}}\right) + ...\right]. \tag{1.18}$$

The largest corrections are coming from the top and bottom quarks, the heaviest known particles the Higgs couples to. Here a cutoff scale Λ_UV at which new physics becomes

non-negligible is needed to regulate the loop integral. Λ_{UV} is usually expected to be close to the Planck mass or GUT scale. A Higgs boson mass of $m_H \approx 125$ GeV, as measured by the ATLAS and CMS collaborations [1, 2], therefore requires an unnatural fine tuning of the bare mass

$$m_{\mathrm{H}}^2\big|_{\mathrm{physical}} = m_{\mathrm{H}}^2\big|_{\mathrm{bare}} - \Delta m_{\mathrm{H}}^2.$$

Taking Λ_{UV} to be near the Planck scale for example, the corrections to the Higgs mass Δm_H^2 would be 32 orders of magnitude larger than the physical Higgs mass.

Unbroken SUSY circumvents this fine tuning predicting a heavy scalar with mass m_{S}, that couples to the Higgs boson. For example, a $-\lambda_{\mathrm{S}} \left|H\right|^2 \left|\mathrm{S}\right|^2$ term in the Lagrangian density, induces a correction from the Feynman diagram in Fig. 1.3b [26]

$$\Delta m_H^2 = \frac{\lambda_{\mathrm{S}}}{16\pi^2}\left[\Lambda_{\mathrm{UV}}^2 - 2m_{\mathrm{S}}^2 \ln\left(\frac{\Lambda_{\mathrm{UV}}}{m_{\mathrm{S}}}\right) + ...\right],$$

where the quadratic term has an opposite sign compared to Eq. (1.18).

However, since SUSY particles have not been found, their Yukawa couplings differ from their SM partners. If SUSY is realised by nature, it must be a broken symmetry. For a broken SUSY to still provide a solution to the hierarchy problem, the relationship between dimensionless couplings (i.e. $\lambda_{\mathrm{S}} = \left|\lambda_{\mathrm{f}}\right|^2$) must be upheld. Otherwise, the total radiative corrections will still contain quadratic divergences

$$\Delta m_H^2 = \frac{1}{8\pi^2}\left[\left(\lambda_{\mathrm{S}} - \left|\lambda_{\mathrm{f}}\right|^2\right)\Lambda_{\mathrm{UV}}^2 + ...\right].$$

Therefore, "soft" supersymmetry breaking is considered. In this case, the effective Lagrangian can be written as $\mathcal{L} = \mathcal{L}_{\mathrm{SUSY}} + \mathcal{L}_{\mathrm{soft}}$, where the SUSY breaking terms are collected in $\mathcal{L}_{\mathrm{soft}}$. Since loop momentum integrals in general always diverge either quadratically or logarithmically, the corrections are of the form

$$\Delta m_H^2 = m_{\mathrm{soft}}^2\left[\frac{\lambda}{16\pi^2}\ln\left(\frac{\Lambda_{\mathrm{UV}}}{m_{\mathrm{soft}}}\right) + ...\right],$$

where λ is schematic for various dimensionless couplings and m_{soft} denotes the largest mass scale associated with the soft terms in $\mathcal{L}_{\mathrm{soft}}$. The splittings between the known Standard Model particles' and their superpartners' masses are controlled by m_{soft}. This implies that supersymmetric particles cannot not be too heavy [26], with the top squark, the supersymmetric partner of the top quark, leading the way. Therefore, it is plausible that SUSY particles are accessible at the LHC.

1.3.2 Minimal Supersymmetric Standard Model

The Minimal Supersymmetric Standard Model (MSSM) is a supersymmetric extension of the SM with the minimum number of new particles and degrees of freedom, which

already more than doubles the SM parameters. Supersymmetric partners (superpartners) of SM fermions receive an additional "s" in front. For example, the superpartner of any of the SM quarks is called a *squark*[4]. The mathematical symbols for the squarks and sleptons are discerned from their fermion counterparts with a tilde, e.g. $\widetilde{q}$. SM particles and their superpartners have the same electric charges, weak isospin, and colour charges. In the case of an unbroken SUSY, this applies to the mass of superpartners as well. Table 1.2 summarises all SM fermions and their corresponding scalar SUSY particles, also called *sparticles*. Vice versa, the superpartner of the scalar SM Higgs

Table 1.2: Chiral supermultiplets in the MSSM [26].

Names		**spin-0**	**spin-1/2**
squarks, quarks	Q	$\begin{pmatrix}\tilde{u}_{\mathrm{L}}\\ \tilde{d}_{\mathrm{L}}\end{pmatrix}$	$\begin{pmatrix}u_{\mathrm{L}}\\ d_{\mathrm{L}}\end{pmatrix}$
($\times$3 families)	$\bar{u}$	$\widetilde{u}^*_{\mathrm{R}}$	$u^\dagger_{\mathrm{R}}$
	$\bar{d}$	$\widetilde{d}^*_{\mathrm{R}}$	$d^\dagger_{\mathrm{R}}$
sleptons, leptons	L	$\begin{pmatrix}\widetilde{\nu}_e\\ \widetilde{e}_{\mathrm{L}}\end{pmatrix}$	$\begin{pmatrix}\nu_e\\ e_{\mathrm{L}}\end{pmatrix}$
($\times$3 families)	$\bar{e}$	$\widetilde{e}^*_{\mathrm{R}}$	$e^\dagger_{\mathrm{R}}$
Higgs, Higgsino	H_u	$\begin{pmatrix}H^+_u\\ H^0_u\end{pmatrix}$	$\begin{pmatrix}\tilde{H}^+_u\\ \tilde{H}^0_u\end{pmatrix}$
	H_d	$\begin{pmatrix}H^0_d\\ H^-_d\end{pmatrix}$	$\begin{pmatrix}\widetilde{H}^0_d\\ \widetilde{H}^-_d\end{pmatrix}$

boson is a spin 1/2 fermion. Note that the Higgs sector contains five Higgs bosons in two chiral supermultiplets in order to avoid gauge anomalies. The superpartners of SM gauge bosons are spin 1/2 fermions. Together they form gauge supermultiplets, as summarised in Table 1.3. Superpartners of bosons are given the name of their SM

Table 1.3: Gauge supermultiplets in the MSSM [26].

Names	**spin-1/2**	**spin-1**
gluinos, gluons	$\widetilde{g}$	g
winos, W bosons	$\widetilde{W}^{\pm}$, $\widetilde{W}^0$	$W^{\pm}$, W^0
bino, B boson	$\widetilde{B}^0$	B^0

partner with an added "ino" at the end.

Tables 1.2 and 1.3 showcase the particle content of the MSSM. However, since SUSY is a broken symmetry, these states mix to different mass eigenstates shown in Table 1.4. The neutral higgsinos, winos and binos mix to four so-called neutralinos $\widetilde{\chi}^0_1$ to $\widetilde{\chi}^0_4$. The charged winos and higgsinos, on the other hand, mix to two charginos $\widetilde{\chi}^{\pm}_1$ and $\widetilde{\chi}^{\pm}_2$. The goldstino $\widetilde{G}$ arises from global SUSY breaking. SUSY allows the

[4]In physics jargon, when talking about specific squarks, their names are often abbreviated by putting the "s" in front of the flavour, such as *stop* or *sbottom* instead of top or bottom squark.

Table 1.4: The MSSM particle content (with sfermion mixing for the first two families assumed to be negligible) [26].

Names	Spin	P_R	Gauge eigenstates	Mass eigenstates
Higgs boson	0	$+1$	$H_u^0\ H_d^0\ H_u^+\ H_d^-$	$h^0\ H^0\ A^0\ H^\pm$
squarks	0	-1	$\widetilde{u}_\mathrm{L}\ \widetilde{u}_\mathrm{R}\ \widetilde{d}_\mathrm{L}\ \widetilde{d}_\mathrm{R}$ $\widetilde{s}_\mathrm{L}\ \widetilde{s}_\mathrm{R}\ \widetilde{c}_\mathrm{L}\ \widetilde{c}_\mathrm{R}$ $\widetilde{t}_\mathrm{L}\ \widetilde{t}_\mathrm{R}\ \widetilde{b}_\mathrm{L}\ \widetilde{b}_\mathrm{R}$	$\widetilde{u}_\mathrm{L}\ \widetilde{u}_\mathrm{R}\ \widetilde{d}_\mathrm{L}\ \widetilde{d}_\mathrm{R}$ $\widetilde{s}_\mathrm{L}\ \widetilde{s}_\mathrm{R}\ \widetilde{c}_\mathrm{L}\ \widetilde{c}_\mathrm{R}$ $\widetilde{t}_1\ \widetilde{t}_2\ \widetilde{b}_1\ \widetilde{b}_2$
sleptons	0	-1	$\widetilde{e}_\mathrm{L}\ \widetilde{e}_\mathrm{R}\ \widetilde{\nu}_e$ $\widetilde{\mu}_\mathrm{L}\ \widetilde{\mu}_\mathrm{R}\ \widetilde{\nu}_\mu$ $\widetilde{\tau}_\mathrm{L}\ \widetilde{\tau}_\mathrm{R}\ \widetilde{\nu}_\tau$	$\widetilde{e}_\mathrm{L}\ \widetilde{e}_\mathrm{R}\ \widetilde{\nu}_e$ $\widetilde{\mu}_\mathrm{L}\ \widetilde{\mu}_\mathrm{R}\ \widetilde{\nu}_\mu$ $\widetilde{\tau}_1\ \widetilde{\tau}_2\ \widetilde{\nu}_\tau$
neutralinos	1/2	-1	$\widetilde{B}^0\ \widetilde{W}^0\ \widetilde{H}_u^0\ \widetilde{H}_d^0$	$\widetilde{\chi}_1^0\ \widetilde{\chi}_2^0\ \widetilde{\chi}_3^0\ \widetilde{\chi}_4^0$
charginos	1/2	-1	$\widetilde{W}^\pm\ \widetilde{H}_u^+\ \widetilde{H}_d^-$	$\widetilde{\chi}_1^\pm\ \widetilde{\chi}_2^\pm$
gluino	1/2	-1	$\widetilde{g}$	$\widetilde{g}$
goldstino gravitino	1/2 3/2	-1	$\widetilde{G}$	$\widetilde{G}$

incorporation of gravity as a local symmetry. However, supergravity theories are not renormalisable. The superpartner of the hypothetical spin 2 graviton is the spin 3/2 gravitino. In an unbroken SUSY the graviton and the gravitino would both be massless. However, a symmetry breaking mechanism similar to that in electroweak theory (called super-Higgs mechanism) causes the goldstino to disappear and the gravitino to become massive.

In total the MSSM contains 124 free parameters compared to the 19 parameters of the SM. Imposing a number of symmetries on top of MSSM heavily constrains the set of free parameters. Searches for SUSY generally use simplified models which consider only a few particles and interactions as will be discussed in some detail in Section 1.3.6.

1.3.3 Dark matter candidate

SUSY can also offer a dark matter candidate [27], given that R-parity conservation holds. R-parity, or matter parity, is an additional symmetry imposed on the MSSM, which does not contain baryon and lepton number conservation by itself. A violation of baryon and lepton number conservation leads to proton decay [28]. There is, however, no experimental evidence of proton decay, hence justifying the use of this symmetry. R-parity is defined as

$$P_R = (-1)^{3(B-L)+2s},$$

where B is the baryon number, L the lepton number and s the spin of the particle. R takes the value $+1$ for all Standard Model particles, while it is -1 for supersymmetric particles. The conservation of R-parity ensures that SUSY particles are produced in pairs, since only an even number conserves the R-parity of $+1$ of a SM particle at each vertex. Furthermore, SUSY particles always decay into other SUSY particles and a SM

particle. This necessitates the existence of a lightest supersymmetric particle (LSP) which is stable if R-parity conservation holds. The LSP can be a viable dark matter candidate.

As of this writing, none of the supersymmetric particles in Table 1.4 has been discovered. If found, however, the neutralino $\widetilde{\chi}_1^0$, which is often considered to be the LSP, is a promising candidate for dark matter.

1.3.4 Unification of gauge couplings

The gauge coupling strengths of the fundamental forces are dependent on the energy scale. While in the SM the evolution of the renormalisation group of inverse gauge couplings does not lead to a unified value, the the modifications in the MSSM can achieve it. Many MSSM models allow for the convergence of the three forces at the GUT scale, as shown in Fig. 1.4.

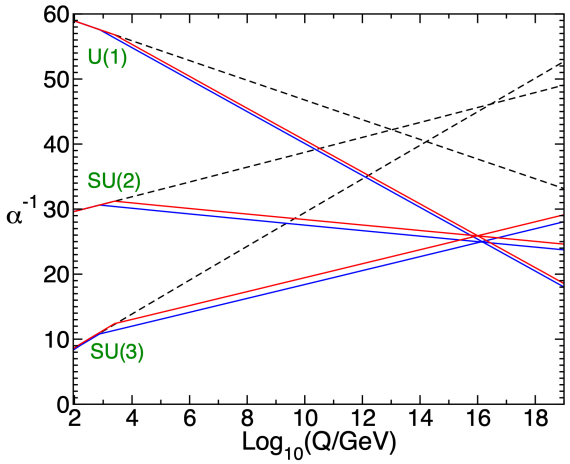

Figure 1.4: Two-loop renormalisation group evolution of the inverse gauge couplings $\alpha^{-1}(Q)$ in the Standard Model (dashed lines) and the MSSM (solid lines) [26].

1.3.5 Search for top squarks

As can be seen in Table 1.4, the superpartners of the heavy SM particles (the left and right handed top and bottom quarks and tau leptons, respectively) mix into mass eigenstates. The mixing between the superpartners of the lighter quarks and leptons, on the other hand, is negligible. This is due to the fact that the masses of these light SM particles are much lighter than their superpartners', which otherwise would long have been discovered. Considering the large mass of the top quark, its superpartners can mix into mass eigenstates $\tilde{t}_1$ and $\tilde{t}_2$ where the former is much lighter than the latter. It might actually make $\tilde{t}_1$ the lightest squark in the MSSM mass hierarchy. Therefore, the search for $\tilde{t}_1$ squark production is well motivated.

In order to explore the possible decay channels for the top squark, one considers the mass difference between top squark and LSP

$$\Delta m = m_{\tilde{t}} - m_{\tilde{\chi}_1^0} \,.$$

For $\Delta m > m_t$ the stop could decay into an on-shell top quark and the $\tilde{\chi}_1^0$, i.e. $\tilde{t} \to t\tilde{\chi}_1^0$. If $m_W < \Delta m < m_t$, on the other hand, a top quark could only enter the decay off-shell, resulting in the three-body decay, $\tilde{t} \to bW\tilde{\chi}_1^0$. Furthermore, a mass gap $\Delta m < m_W$ requires both an off-shell top quark and W boson in the decay chain with the result of a four body decay, $\tilde{t} \to b\mathrm{ff}'\tilde{\chi}_1^0$. This last region of parameter space is referred to as "compressed".

The conservation of R-parity, as discussed in Section 1.3.3, requires top squarks to be pair-produced. To leading order, top squark pair production in pp collisions [29] happens via quark-antiquark annihilation and gluon-gluon fusion at LHC energies. Figure 1.5 shows the relevant Feynman diagrams.

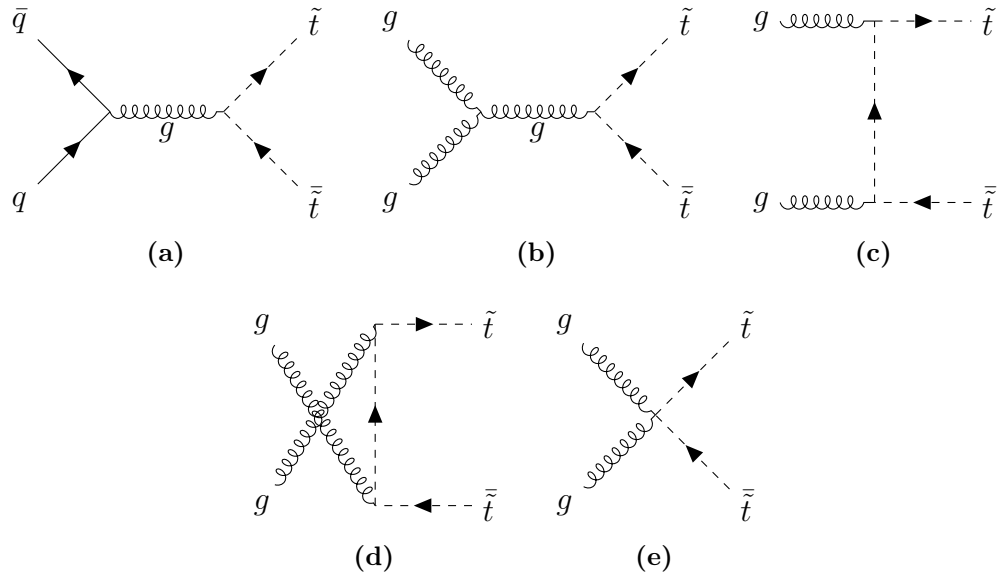

Figure 1.5: Leading order Feynman diagrams (quark-antiquark annihilation and gluon-gluon fusion) for top squark pair production.

1.3.6 Simplified models

Searches for SUSY are designed to be sensitive to only a relatively narrow sector of the parameter space of the MSSM which allows the use of simplified models. Simplified Model Spectra (SMS) utilise simplified topologies for particle production and decay. In particular, only a few SUSY particles and interactions are considered in a given SMS. All other SUSY particles are assumed to be decoupled, considering them to have large enough masses as to not affect production or decay modes of the lighter

particles. Besides, branching ratios are usually sset to 100%. Mixed decays can then be considered with a linear combination of models. The remaining parameters in a given SMS, namely masses, cross sections and branching ratios of the light particles, can be determined from experimental signatures. Of course, several SMS can produce the same experimental signatures. SUSY analyses aim to put limits on production cross sections and branching ratios to constrain specific models.

In the present thesis, a search for scalar top superpartners is discussed. Focussing only on R-parity conserving models, top squarks, denoted as $\tilde{t}$, must be produced in pairs $\tilde{t}\bar{\tilde{t}}$. In principle, top squarks can have a variety of decay modes, depending on the mass hierarchy of the SUSY particles. In the analysis that is discussed in Section 5, three top squark decay modes are considered. The first one is $\tilde{t} \to t\tilde{\chi}_1^0$, where t and $\tilde{\chi}_1^0$ are the top quark and the lightest neutralino, respectively. This decay mode (`T2tt`) is shown in Fig. 1.6a. Figure 1.6b displays the second model (`T2bW`), which describes the

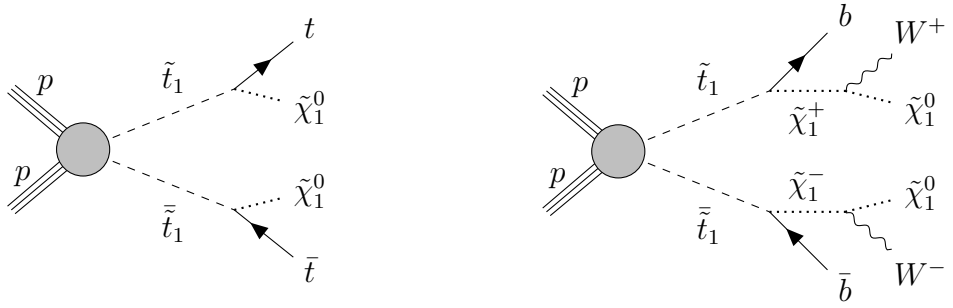

(a) `T2tt` **(b)** `T2bW`

(c) `T8bbllnunu`

Figure 1.6: SUSY Signals

decay mode $\tilde{t} \to b\tilde{\chi}_1^\pm \to W^\pm\tilde{\chi}_1^0$, i.e. two top squarks decaying into a bottom quark and a chargino each. The charginos subsequently decay into a W boson and the lightest neutralino. The chargino mass is set to the arithmetic mean of the top squark and the neutralino, $m_{\tilde{\chi}_1^\pm} = \frac{1}{2}(m_{\tilde{t}} + m_{\tilde{\chi}_1^0})$. The third decay mode (`T8bbllnunu`) features a cascade decay of the top squark, $\tilde{t} \to b\tilde{\chi}_1^\pm \to \nu\tilde{\ell} \to \ell\tilde{\chi}_1^0$, where the top squark decays into the lightest chargino $\tilde{\chi}_1^\pm$, which in turn decays to a slepton $\tilde{\ell}$, which finally results in a neutralino. `T8bbllnunu` is shown in Figure 1.6(c). Similar to `T2bW`, the chargino mass will be assumed as $m_{\tilde{\chi}_1^\pm} = \frac{1}{2}(m_{\tilde{t}} + m_{\tilde{\chi}_1^0})$ in this interpretation. For the slepton

mass, three different scenarios are considered according to

$$m_{\tilde{\ell}} = x \cdot (m_{\tilde{\chi}_1^\pm} - m_{\tilde{\chi}_1^0}) + m_{\tilde{\chi}_1^0},$$

where the slepton mass is either close to the chargino ($x = 0.95$), half way between chargino and neutralino ($x = 0.5$) or close to the neutralino ($x = 0.05$). A visualisation how the chargino and slepton lie in the mass hierarchy set by the stop and neutralino masses is given in Fig. 1.7. It is especially noteworthy that this mode has a

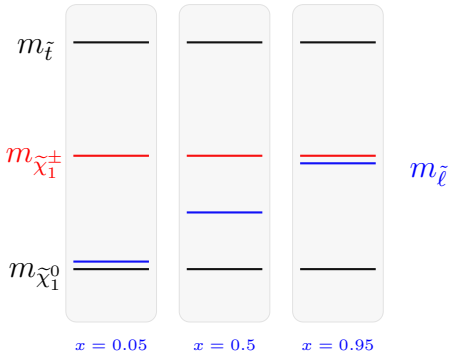

Figure 1.7: Illustration of the masses of the intermediate chargino $\tilde{\chi}_1^\pm$ and slepton $\tilde{\ell}$ for the `T8bbllnunu` model.

100% branching ratio to two opposite-sign leptons in the final state. This exhibits the sensitivity of this analysis nicely.

2 | Large Hadron Collider

The Large Hadron Collider (LHC) is a circular collider that is designed to accelerate and collide two proton beams at a center-of-mass energy of 14 TeV. To date, it is the largest and most powerful particle collider in the world. The LHC was constructed by the European Organization for Nuclear Research (CERN) with the intent to help answer some of the open questions in physics. It was built from 1998 to 2008 in the preexisting tunnels of its predecessor, the Large Electron-Positron Collider (LEP). The LHC's tunnel has 27 kilometres in circumference and lies near the Swiss city of Geneva underneath the border to France at a depth of 45–170 metres. Besides the proton–proton collisions, the LHC's programme also foresees heavy-ion collisions for one month per year. The heavy-ion beams are made of lead ions that reach up to 2.76 TeV per nucleon. They are brought to collisiob with another heavy-ion beam or with a proton beam [30].

2.1 CERN's accelerator complex

Before a proton beam is injected into the LHC, it passes through a series of preacceleration steps where it is shaped and subsequently accelerated. The whole CERN accelerator complex including the experiments is shown in Fig. 2.1. At the initial stage, ionised hydrogen atoms are accelerated via the linear accelerator (LINAC 2) to roughly 50 MeV. Next, the Proton Synchrotron Booster (PSB) accelerates the protons further to 1.4 GeV, before they are injected into the Proton Synchrotron (PS). There, 26 GeV protons are produced which are also separated into packets of 115 billion protons – called bunches. Subsequent bunches have a time spacing of 25 ns. Bunching serves the purpose of having discrete time intervals where interactions between the two beams happen in the LHC's four intersection points. The last stage of preacceleration is the Super Proton Synchrotron (SPS). The SPS was a particle collider by itself. When it was operating, the W and Z bosons were discovered in 1983 by the UA1 experiment [11] Proton bunches are boosted to 450 GeV in the SPS, before injection into the LHC ring. It takes 12 SPS cycles to fill the LHC with a total of 2808 bunches per beam. The oppositely rotating beams are currently accelerated to 6.5 TeV via 8 radio frequency (RF) cavities with a frequency of 400 MHz. They deliver a center-of-mass energy of 13 TeV at the collision points where the experiments are located. LHC's two all purpose detectors are ATLAS (A Toroidal LHC ApparatuS) [31] and CMS (Com-

pact Muon Solenoid) [32], which will be described in detail in the following chapter. The LHCb experiment [33] is designed to probe hadron decays involving bottom and charm quarks. The fourth experiment, ALICE (A Large Ion Collider Experiment) [34], is primarily used to study the quark gluon plasma with lead ion collisions, hence its name.

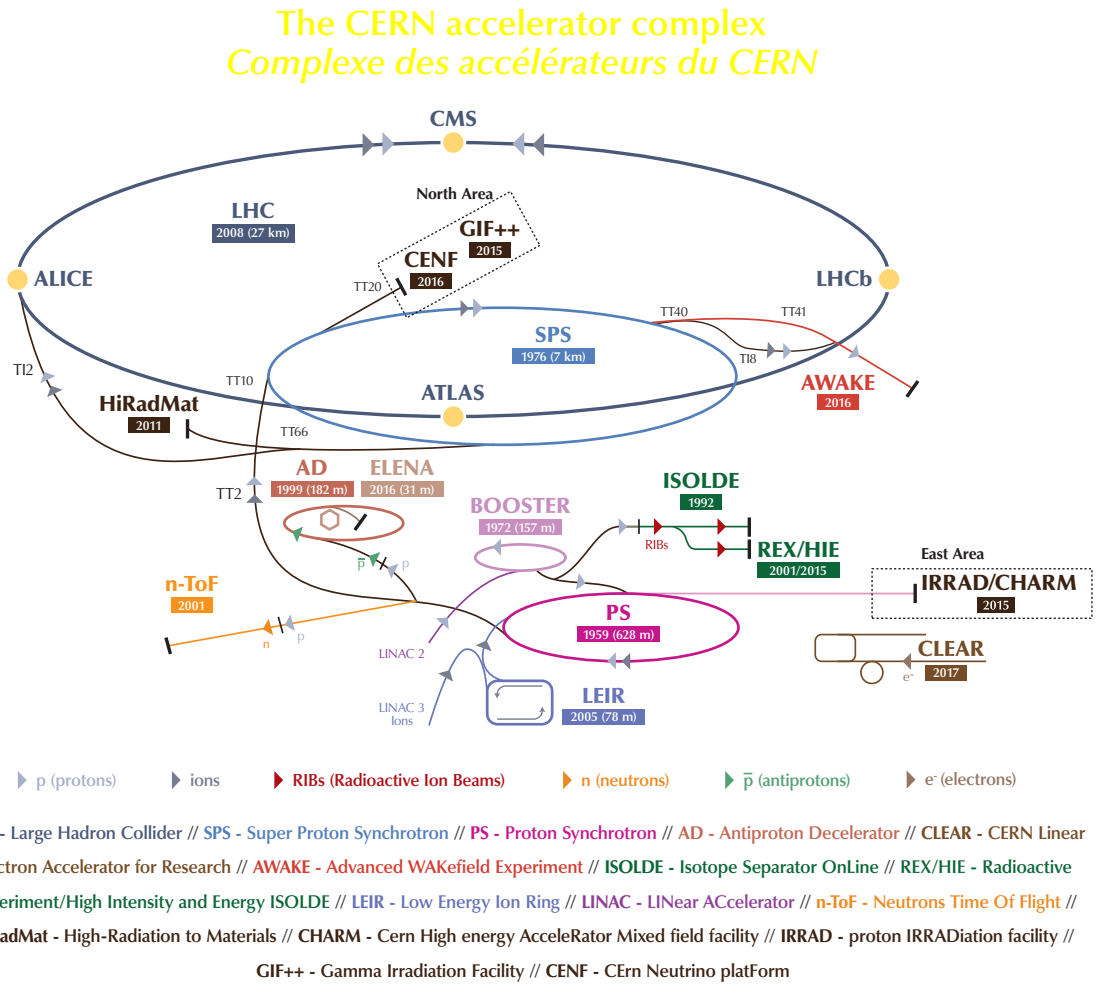

Figure 2.1: Schematic illustration of CERN's accelerator complex [35].

2.2 LHC magnets

A crucial part to make the LHC work is the extensive use of powerful magnets in order to keep the proton or heavy-ion beam on a controlled path within the beamlines as they circle the LHC. In order to fit the LHC into the limited space of the existing LEP tunnels, it has been designed as a single ring accelerator. The two beamlines, each containing one of the beams which travel in opposite directions around the ring, run

parallel and directly adjacent to each other. To minimise accelerated particles colliding with air molecules, the beamlines are held at an ultra-high vacuum. The beams intersect at four points around the ring, which is where the particle collisions take place. At the interaction points, the beam cross section is about 0.06 mm. Since the oppositely rotating beams contain particles of the same charge, they require magnetic fields with opposite direction for steering. This is achieved via superconducting dipole magnets which provide a magnetic field of up to 8.3 T. An illustration of the dipole setup and magnetic flux around the beamlines is displayed in Fig. 2.2. The magnets are cooled down to 1.9 K using superfluid helium in order to keep them functioning properly. For orbital and momentum focusing of the beams, with special emphasis near the intersection regions, quadrupole magnets are used. Furthermore, sextupole and octopole magnets are used for additional fine tuning of the proton beam geometry.

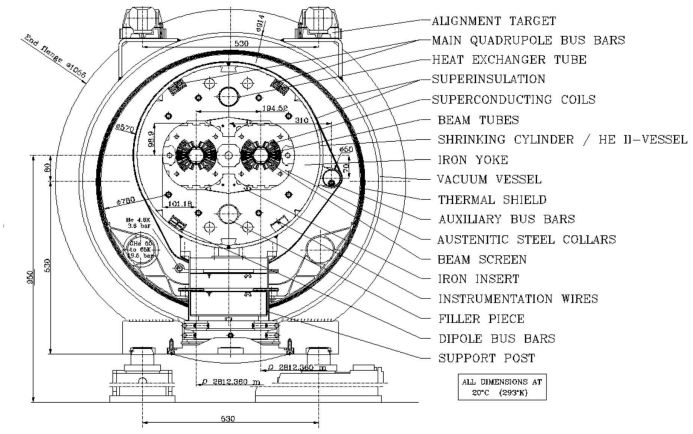

(a) Cross section of cryodipole

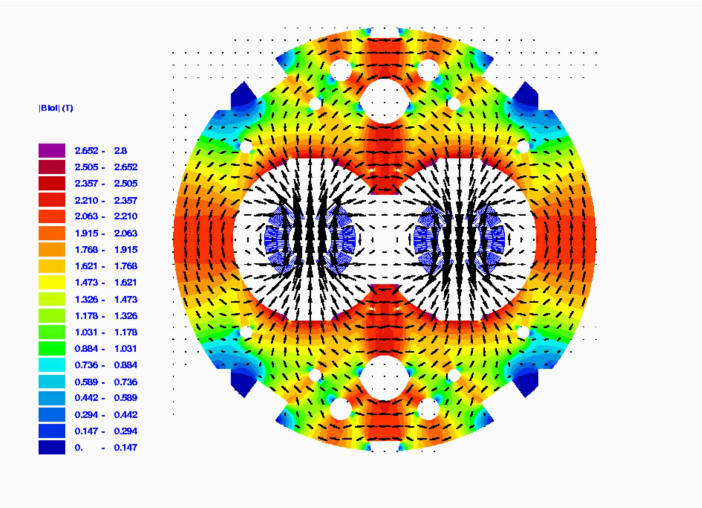

(b) Dipole magnetic flux plot

Figure 2.2: Illustration of LHC dipole magnet [30].

2.3 LHC physics

The LHC has been designed and built to probe the Standard Model and possible extensions to it, such as SUSY. The expected number N_{events} of events for a given process is determined by the relation

$$N_{\text{events}} = \sigma_{\text{process}} \cdot L \,. \tag{2.1}$$

The production cross section of a process σ_{process} is proportional to the probability of the process to take place at the given energy. For BSM processes, the production cross sections are typically much smaller than for SM processes. The second factor, $L = \int \mathcal{L}\,\mathrm{d}t$, is the integrated luminosity, which is the time-integral of the instantaneous luminosity $\mathcal{L}$ registered by the LHC's experiments. Since the production cross section is fixed by the LHC's center-of-mass energy, luminosity determines the achieveable sensitivity of the searches and the measurements. The instantaneous luminosity $\mathcal{L}$ can be calculated by

$$\mathcal{L} = \gamma \frac{N_{\text{p}}^2\, n_{\text{b}}\, \nu_{\text{rev}}}{4\pi\, \epsilon_{\text{n}}\, \beta^*} F \,. \tag{2.2}$$

In this expression, γ is the relativistic Lorentz factor of the accelerated protons. These protons are travelling with a revolution frequency ν_{rev} around the LHC ring. There are n_{b} bunches per beam, with N_{p} particles per bunch. The normalised transverse beam emittance ϵ_{n} is a measure of the spread of beam in the momentum and position phase space, while β^* is the optical beta function at the collision point. Multiplying ϵ and β^* together is a measure for the transverse beam cross section area, $\sigma_x \sigma_y = \epsilon \beta^*$. Finally, the geometric luminosity reduction factor F depends on the total crossing angle at the interaction point. Table 2.1 shows the LHC's design values of the quantities in Eq. (2.2), determining the instantaneous luminosity for the experiments. Using those parameter values, one obtains a design luminosity of $\mathcal{L} = 1.0 \times 10^{34}\,\text{cm}^{-2}\,\text{s}^{-1} = 10\,\text{nb}^{-1}\,\text{s}^{-1}$ for the CMS and ATLAS experiment. This value has been roughly doubled over the course of 2017. During the LHC's last run period between 2016 and 2018, the CMS experiment has recorded roughly $140\,\text{fb}^{-1}$ of integrated luminosity.

Table 2.1: LHC beam parameters relevant for the peak luminosity [30].

parameter	**value**
γ	7461
N_{p}	1.15×10^{11}
n_{b}	2808
ν_{rev}	11.245 kHz
ϵ_{n}	3.75 μm
β^*	0.55 m
F	0.836

3 | Compact Muon Solenoid

The Compact Muon Solenoid (CMS) collaboration runs one of the two general-purpose detectors at the LHC, the other one being run by the ATLAS experiment. The CMS detector was designed to take full advantage of the physics data generated by the proton-proton and heavy-ion collisions at the LHC, with a special emphasis on precisely measuring muon properties. Goals pursued by the experiment have been the accurate measurement of SM properties including a search and, if found, future study of the Higgs boson, as well as the general search for physics beyond the SM from the get-go. In 2012, the CMS collaboration reached one of the major goals, the discovery of the elusive Higgs boson, jointly announced with the ATLAS collaboration [1, 2]. The CMS detector has a length of about 28.7 metres, is 15 m in diameter and weighs roughly 14 thousand tonnes. Figure 3.1 shows an illustration that aims to put the dimensions into context. Starting in 2016, CMS has been used to measure and identify particles coming from proton–proton collisions at a center-of-mass energy of 13 TeV. The data from these collisions will be used in this thesis.

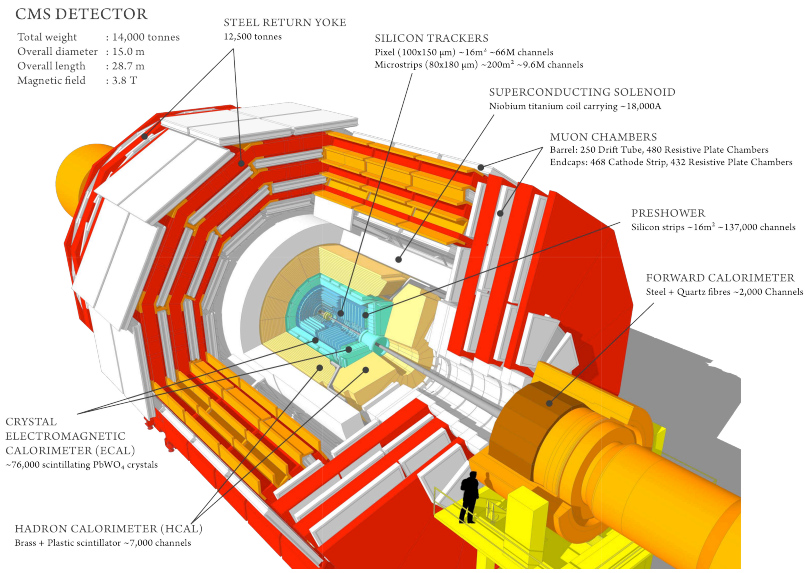

Figure 3.1: Schematic illustration of the CMS detector components. The person next to the forward calorimeter is to get an idea for the size of the detector [36].

The CMS detector is compact. The key component to achieve high precision in a

small space is the superconducting magnet coil, which delivers a magnetic field of 3.8 T. Due to the high magnetic field, the trajectories of charged particles bend, which is the essential feature used in momentum measurements. Figure 3.2 shows how different kinds of particles behave in the magnetic field. Located inside the solenoid are the tracking system and calorimeters. The silicon tracker system is the innermost layer of the CMS detector and is used to reconstruct trajectories of charged particles, such as electrons, muons and charged hadrons. Around the tracker, the electromagnetic and hadronic calorimeters are situated, where energy deposits of electronmagnetically and hadronically interacting particles are measured. Photons and electrons are mostly brought to a halt in the electromagnetic calorimeter, while hadrons pass through to the hadronic calorimeter. The outermost shell of the detector, outside of the solenoid, is a dedicated system for measuring muons. These are the only detectable particles frequently penetrating that far through the detector. The special design of the detector allows for efficiently identifying muons with momenta up to 1 TeV transverse to the beam [32, 37, 38]. Neutrinos are the only SM particles leaving the dector without a trace due to their weakly-interacting nature.

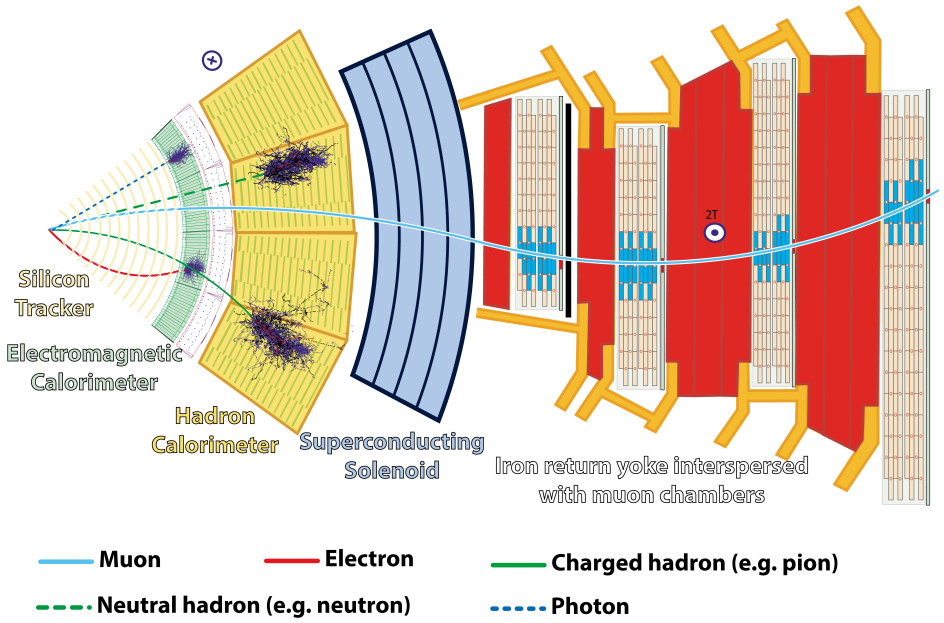

Figure 3.2: Slice of the CMS detector structure [39].

In order to efficiently describe particle trajectories in the CMS detector, there are various sets of coordinates that in use. The origin is always defined at the geometrical origin of the detector. A cartesian-type coordinate system is defined with the z-axis pointing in the direction of the beam that is travelling anticlockwise, while the x-axis points radially inwards to the center of the LHC and the y-axis points vertically upwards. These can also be transformed to spherical coordinates, where the radial distance r denotes the distance from the interaction point. The azimuthal angle ϕ is then measured from the x-axis in the transverse x-y plane and the polar angle θ measures the angle from the z-axis. However, due to the relativistic nature of particle

collisions, it is convenient to trade the polar angle θ for a new angular coordinate called pseudorapidity by $\eta = -\ln\tan\frac{\theta}{2}$. The pseudorapidity η is measured in the y-z plane. In negative z-axis direction η takes negative values. For a particle travelling close to the speed of light, pseudorapidity is a good approximation of the particle's rapidity which is a Lorentz-invariant quantity defined as $y = \frac{1}{2}\log(\frac{E+p_z}{E-p_z})$. The CMS detector can be thought to be split into three main regions with respect to the pseudorapidity, cf. Fig. 3.3. The so-called barrel region ($|\eta| < 1.3$), the endcap region ($1.3 < |\eta| < 3.0$) and the forward region ($3.0 < |\eta| < 5.2$). Particles with η greater than 5.2 cannot be detected.

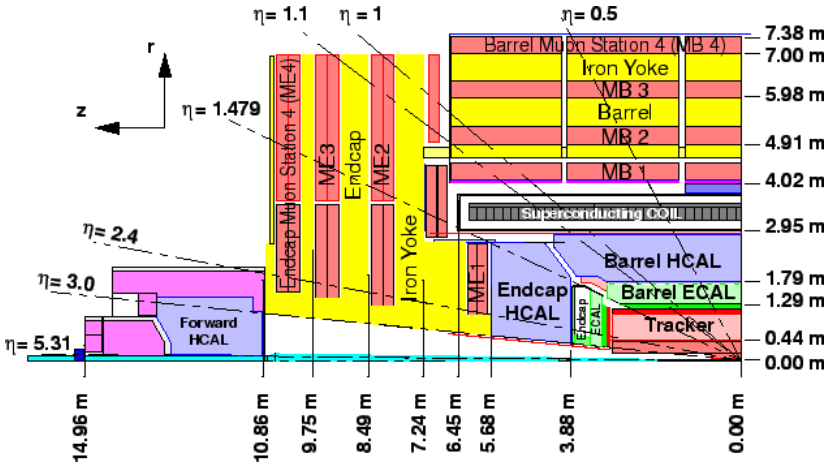

Figure 3.3: Illustration of the detector components and the η region they belong to [40].

The angular separation ΔR between two particles in the η-ϕ plane is given by the separation in η and ϕ as $\Delta R = \sqrt{\Delta\phi^2 + \Delta\eta^2}$. As the initial momentum $|\boldsymbol{p}_0| = p_z$ of the colliding system is not known, the transverse component of the momentum $\boldsymbol{p}_T$ is used. This is useful, since the initial p_T of the incoming partons can be neglected. Using the conservation of energy and momentum, one can identify imbalances in the energy distribution around the interaction point. This is quantified in the $p_\mathrm{T}^\mathrm{miss}$ variable which, if not equal to zero, is characteristic of either imprecisely measured particles or non-detectable particles, such as neutrinos, or possible BSM particles.

3.1 Superconducting solenoid magnet

The heart of the CMS detector is a superconducting solenoid magnet which produces a 3.8 T magnetic field, needed for the precise measurements of charged particles produced in LHC beam collisions. The magnet is designed to produce a 4 T field, but is operated at 3.8 T to maximise its lifetime. The high field is achieved by a superconducting coil that is operated at 4.5 K. The cryogenic temperatures are provided by liquid He which is injected into the cryostat. A nominal electric current of over 18 kA runs through the solenoid, resulting in a stored energy of 2.3 GJ. The inner bore of the magnet,

where the magnetic field is homogeneous, has a diameter of 6.3 m and is 12.5 m long. It houses the tracking and calorimeter systems. A 10k tonne iron yoke is used to contain the magnetic fields within the detector volume. Its effect on the magnetic field is displayed in Fig. 3.4.

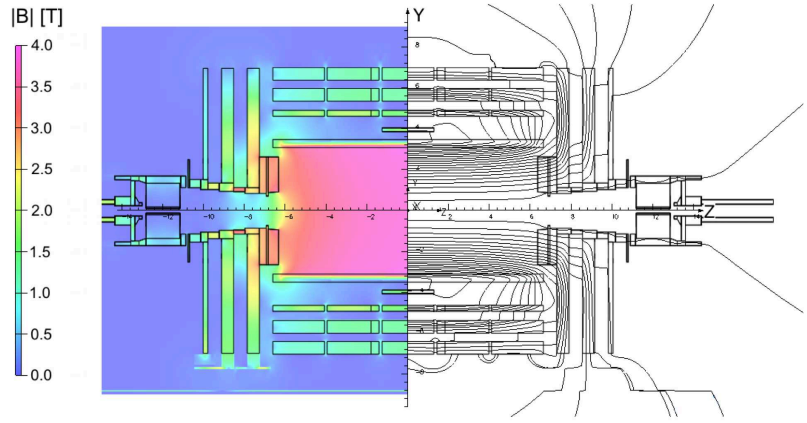

Figure 3.4: Predicted magnitude of the B-field (left) and the field lines (right) in the volume covered by the CMS detector [41].

3.2 Pixel and Strip Trackers

The detector complex closest to the interaction point is the tracker system. It is divided into pixel and strip trackers that measure trajectories of charged particles emerging from proton-proton collisions. Besides, also secondary vertices from the decay of heavy-flavoured hadrons can be measured accurately. Together, the silicon trackers have a length of 5.8 m, a diameter of 2.5 m, and a tracking coverage of $|\eta| < 2.5$. The challenging conditions from LHC collisions require advanced tracking technologies with high granularity and fast response in order to reliably measure the particle trajectories and disentangle tracks from pileup. Furthermore, components in the detector need to withstand the high radiation for an extended period of time which is the reason for the all-silicon design of the CMS tracker system.

The pixel detector consists of 66 million silicon pixels with a dimension of $100\,\mu\text{m} \times 250\,\mu\text{m} \times 250\,\mu\text{m}$. The sensors are composed in three cylindrical layers in the barrel region at a distance of 4.4, 7.3 and 10.2 cm from the beamline, as well as two disks in the forward and backward regions. They disks extend the η coverage to ± 2.5. The pixel tracker provides a spatial resolution of roughly $10 - 15\,\mu\text{m}$ which is sufficient for track reconstruction, primary- and secondary vertex reconstruction. However, due to radiation damage the resolution is degraded over time.

The strip tracker surrounds the pixel tracker. A total of 9.3 million silicon strip sensors are assembled in ten layers in the barrel region and 12 disks on each side of the barrel. As depicted in Fig. 3.5, the Tracker Inner Barrel (TIB) consists of four layers that

cover the region with $|z| < 65\,\text{cm}$. The Tracker Outer Barrel (TOB) has six layers ranging 110 cm to each side of the interaction point and extends to a radius of 110 cm. The three Tracker Inner Disks (TID) cover 45 cm to the left and right of the TIB. Finally, the nine disks constituting the Tracker End Cap (TEC) range over the interval $120 < |z| < 280\,\text{cm}$. A double-layer setup of modules, denoted by double lines in Fig. 3.5, allows measurements of the z and r directions in the barrel and the endcaps. The resolution of 30 µm in the (r, ϕ) plane and 300 µm in z direction is slightly worse than that of the pixel tracker.

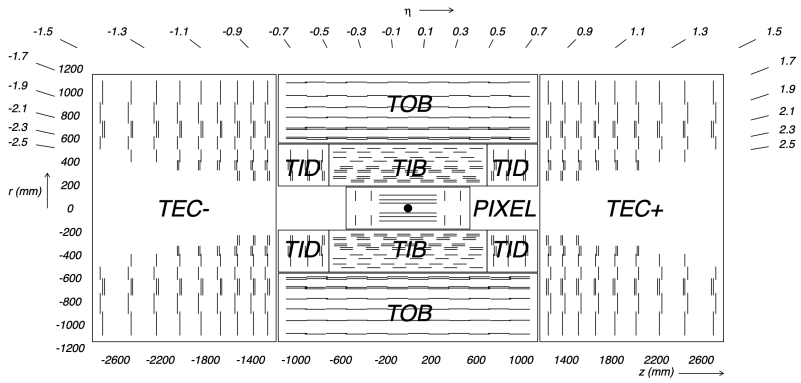

Figure 3.5: Schematic cross section through the CMS tracker. Each line represents a detector module [32].

3.3 Electromagnetic Calorimeter

The electromagnetic calorimeter (ECAL) subdetector is designed for high precision measurements of the energy and position of electrons and photons. The main motivation behind its design is the capability to detect the diphoton final-state of the Higgs boson, which requires a reliable separation of photons from neutral pions. Furthermore, for an accurate measurement of jet energies, a significant portion is carried by photons, thus a high photon energy resolution is needed. In total the CMS ECAL detector consists of almost 76 thousand lead tungstate ($PbWO_4$) crystals which are particularly radiation hard, while providing high granularity. When electromagnetically interacting particles enter the ECAL crystals, they initiate showers. The interplay of pair-production of electrons by energetic photons and bremsstrahlung of energetic electrons results in a cascade of electrons and photons of decreasing energy. As particle energies drop below a critical energy, the cascade beaks down and ionisation becomes the dominant source of energy loss for the electrons. When the ionised crystal atoms recombine with electrons, they emit a blue-green scintillation light which is captured by the photodetectors located at the end of the crystal that is facing away from the beamline. The ECAL crystals are able to provide a short scintillation decay time in order to be compatible with the 25 ns bunch spacing at the LHC.

The ECAL consists of a cylindrical section, the so-called ECAL barrel (EB) section,

surrounding the tracker in the pseudorapidity range $|\eta| < 1.48$. The front faces of the EB crystals are at a radius 1.29 m from the beamline. The ECAL endcaps (EE) at both ends extend the coverage to $|\eta| < 3.0$ at a longitudinal distance of 3.15 m from the interaction point. In addition to the EB and EE, the preshower detector (ES) is utilised to distinguish single photons from photon pairs produced in the decay of neutral pions. Photons produced from a pion decay typically enclose a smaller angle in the forward region. Because of the high granularity of the ES, which is installed in front of the EE in the forward and backward regions, a better position measurement of the electrons and photons is possible. To achieve the optimal precision of the detector a thorough calibration of the ECAL is necessary. The calibration of the ECAL is performed using cosmic-rays and collisions from high energy electrons beams. Thereby, a precise measure of the absolute value of measured energies can be achieved and channel-to-channel relative effects mitigated.

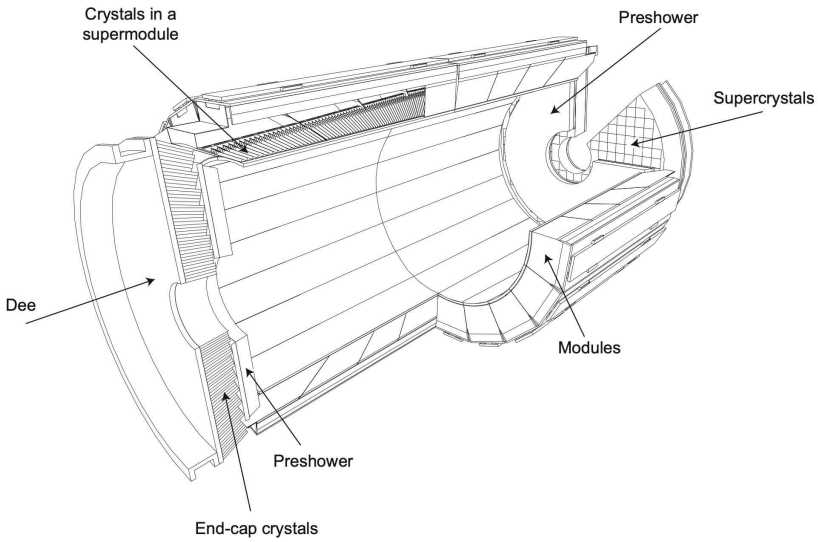

Figure 3.6: Layout of the ECAL showing the arrangement of crystal modules [32].

The ECAL barrel energy resolution for each group of 3×3 crystals was measured using electrons in beam tests. It can be parametrised [42] in terms of the energy E as

$$\left(\frac{\sigma_E}{E}\right)^2 = \left(\frac{2.8\%}{\sqrt{E\,(\text{ GeV})}}\right)^2 + \left(\frac{12\%}{E\,(\text{ GeV})}\right)^2 + (0.3\%)^2 \,, \tag{3.1}$$

where the three contributions are added in quadrature. They correspond to stochastic contributions, noise from electronics, digitisation and pileup, and a constant term coming from channel-to-channel calibration errors and also the leakage of electromagnetic showers from the back of the crystals. A 120 GeV electron, for instance, has a resolution of 0.41%.

3.4 Hadronic Calorimeter

The outermost detector layer that is located largely within the magnet coil is the hadronic calorimeter (HCAL). It is designed to measure the energy and position of hadrons. The CMS HCAL consists of about 70 thousand scintillating tiles. Alternating layers of brass absorber material and plastic scintillator materials are used. Brass is chosen as the absorber material, because it is non-magnetic and has a short nuclear interaction length (about 16 cm). As hadrons enter the HCAL, they interact with nuclei in the brass material and produce a hadronic shower cascade. When particles in the shower enter one of the plastic layers, scintillator light is emitted which is used to measure the energies of the particles in the shower. The HCAL covers an η range up to $|\eta| < 5$, which allows for an accurate measurement of the energy imbalance in the transverse plane.

As can be seen in Fig. 3.7, the HCAL is divided into four subsystems. In the central region ($|\eta| < 1.3$) the HCAL barrel (HB) is located. The HCAL endcap (HE) is positioned in the endcap region ($1.3 < |\eta| < 3$). To maximise the hermeticity of the subdetector, the HCAL forward (HF) extends the coverage in the forward region ($3 < |\eta| < 5$), located 11.2 m away from the interaction point. Thick steel segments (1.65 m) serve as absorbers. Since the energy deposits per collision are about seven times as high as for the rest of the detector, radiation-hard quartz fibres are utilised as the active medium. Photomultiplier tubes capture the Cherenkov light produced by charged particles travelling faster than the speed of light in the quartz fibres of the HF. To catch late showering hadrons, the HCAL outer (HO), also called tail catcher, is positioned outside the magnet. The energy that escapes the HB is collected by the HO which increases the effective thickness and consequently the energy resolution of the HCAL. The solenoid also acts as an additional absorber for the HO and allows to identify late showering hadrons.

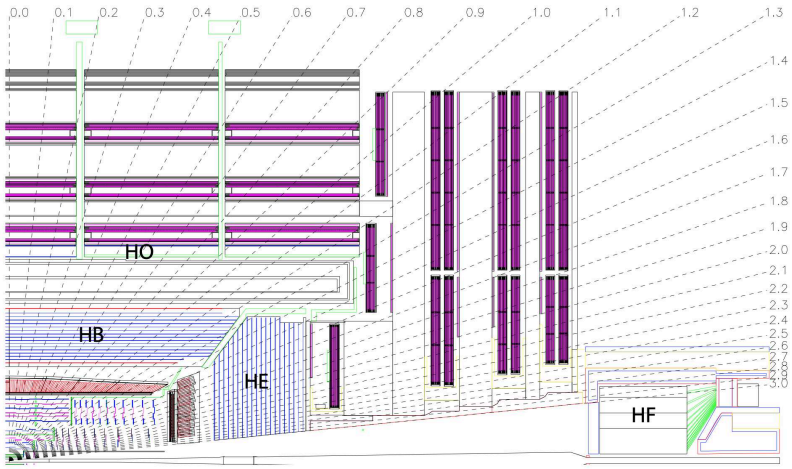

Figure 3.7: Longitudinal view of the CMS detector showing the locations of the hadron barrel (HB), endcap (HE), outer (HO) and forward (HF) calorimeters [32].

The energy resolution, which is optimised using pion beams, is given by

$$\left(\frac{\sigma_E}{E}\right)^2 = \left(\frac{94.3\%}{\sqrt{E\,(\text{ GeV})}}\right)^2 + (8.4\%)^2\,,$$

where the first term is of stochastic nature and the second one is constant [43, 44]. For example, a pion energy of 120 GeV has a resolution of 12%.

3.5 Muon system

The muon system is responsible for the effective identification and momentum measurement of muons. A good momentum resolution is guaranteed by the high magnetic field and the flux-return yoke of the CMS detector. Due to the muon's larg mass, it suffers smaller radiative losses in the tracker material and can even penetrate through the calorimeters and the solenoid. This is the reason why muon chambers are located in the outermost region of a detector. When a muon passes through the gas in a muon chamber, it leaves an ionised track. Free electrons are produced and an electric field forces them to move toward the anode, causing an electric signal being induced in the wire. The signal hit has a resolution of $100\,\mu$m in the r direction and 10^{-3} rad in ϕ direction.

The cylindrical layout of the muon system is composed of a detector section in the barrel region and two endcap sections. Three types of gaseous detectors are used: drift tubes (DTs), cathode strip chambers (CSCs) and resistive plate chambers (RPCs). DTs are aluminum tubes filled with an 85 to 15% mixture of argon and CO_2, respectively, at atmospheric pressure. As is shown in Fig. 3.8, the DTs are employed in the barrel region with $|\eta| < 1.2$. The two endcap regions ($0.9 < |\eta| < 2.4$) are equipped with CSCs, which have a fast response time and good resistance to radiation. Their chambers are filled with 40% argon, 50% CO_2 and 10% CF_4. In order to provide extra coverage in the $|\eta| < 1.6$ region, RPCs are used. The detectors have a low spatial resolution due to their large strip width. Their temporal resolution of about 1 ns, on the other hand, is excellent and allows for unambiguous bunch crossing identification.

3.6 Trigger and data acquisition system

The CMS trigger system processes real-time event data from all the sub-detectors and only information about events that are likely to include interesting physics is staged for storage. At the LHC's design luminosity of $\mathcal{L} = 10^{34}\text{cm}^{-2}\,\text{s}^{-1}$ and the nominal bunch crossing rate of 40 MHz, which corresponds to a 25 ns bunch spacing, about 10^9 interactions take place per second. It is by no means feasible to store the collected data for each interaction, as this would require a gigantic storage space in the order of 50 TB per second. Besides, a large majority of events, do not include a hard

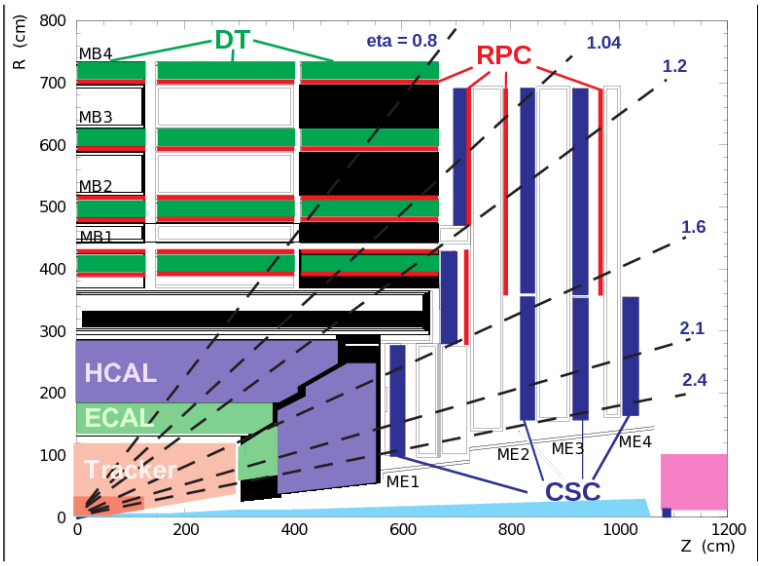

Figure 3.8: Longitudinal layout of one quadrant of the CMS detector, showcasing the muon system. The four DT stations in the barrel (green), the four CSC stations in the endcap (blue), and the RPC stations (red) are shown [45].

scattering interaction and can, therefore, be discarded right away. The CMS trigger is constructed in a two-tier manner, constituted by the Level-1 Trigger (L1T) and the High Level Trigger (HLT). This way, the number of events selected for storage is reduced to between 800 and 1000 interactions per second.

The first trigger stage, the L1T, is responsible for processing the raw information from the tracker, the calorimeters and the muon system. An overview of the L1 trigger architecture is shown in Fig. 3.9. The trigger is allowed a very limited amount of

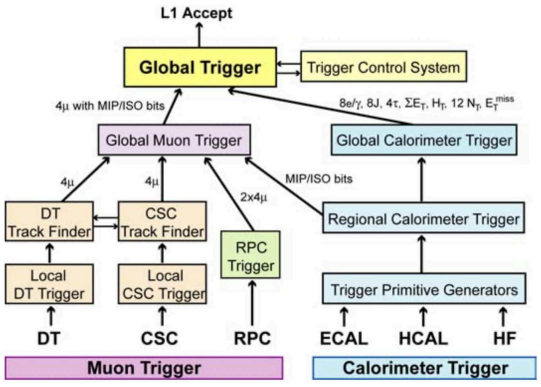

Figure 3.9: Architecture of the Level-1 Trigger [32].

time to process the detector data. The decision on whether to accept or reject an event for storage happens within 4 µs of collision. This can be achieved only due to custom-designed electronics, reduced resolution for the construction of trigger primitives (TPs), as well as simple algorithms to process all the incoming information. The

TPs are generated using energy deposits in the calorimeters or hit patterns in the muon chambers. Regional triggers combine this information to produce the trigger objects, which are candidates for physics objects. Besides, the local triggers also handle the sorting the trigger objects based on their energy or momentum and the quality of the reconstructed TPs. Trigger objects include the calculated missing transverse energy, jets, the four highest ranked candidate objects of muons, isolated and non-isolated electrons and photons, respectively, as well as τ-like objects. The best-ranked trigger objects get passed on by the global calorimeter trigger and the global muon trigger. The final decision at the level of the L1T is made by the global trigger (GT) on a basis of over one hundred algorithms being applied to the trigger objects. If any of the trigger algorithms accepts an event, it is read out by the data acquisition system and passed on to the HLT for further processing. Due to the HLT's computing power, the output rate of the L1T must be kept below 100 kHz.

The HLT is implemented as a software system on a large computing farm. Therefore, it can use more sophisticated algorithms on all the available detector data akin to those used in offline analyses to reconstruct the physics objects. Overall the HLT can reduce the rate of selected events for storage to less than 1 kHz, while the processing delay time is about one tenth of a second.

4 | Reconstructing physics objects

Physics objects such as leptons, photons, and jets participating in an event are reconstructed from the CMS detector data using the so-called particle flow (PF) algorithm [46]. Any physics analysis is based on these reconstructed physics objects. Input elements to the PF algorithm are the *tracks* of charged particles from the tracker, energy deposits from the calorimeters, and muon candidates.

Tracks are reconstructed iteratively using hits in the pixel and strip detectors. The tracks with the tightest criteria are identified first and their hits removed from subsequent iterations. Reconstructed tracks allow a precise measurement of the transverse momentum p_{T}. Furthermore, they provide the direction of charged particles at the primary vertex (PV).

Energy clusters are reconstructed by first identifying cells that surpass a certain energy threshold and then a clustering algorithm combines information of neighbouring cells to determine clusters. This is done separately in each of the calorimeter subsystems, except for the HF where no clustering is needed. Clusters are then exploited for several purposes. Firstly, they are used to detect and measure the energy and direction of stable neutral particles such as neutral hadrons and photons. Secondly, neutral particles are separated from charged hadrons. Furthermore, electrons are combined with corresponding radiated bremsstrahlung photons.

The basis of the PF algorithm is the linking algorithm. By combining tracks and energy clusters from all sub-detectors that are compatible with a particle hypothesis, the link algorithm produces PF blocks. In a subsequent identification and reconstruction process, the PF algorithm splits these blocks into the particles. Tracks and clusters pertaining to an identified particle are gradually removed from the blocks to avoid double counting. Since muons only leave tracks in the tracker and muon systems, they are the first particles to be identified. Next, electron and isolated photons are identified using tracks and ECAL clusters. Afterwards, the remaining tracks and calorimeter clusters in a block are successively checked for compatibility with charged hadrons, neutral hadrons, non-isolated photons, as well as hadrons from nuclear interactions. In order to identify charged hadrons a good agreement between the calorimetric energy and track momentum is necessary. The excess ECAL and HCAL clusters which were not successfully linked to any of the tracks are associated with photons or neutral hadrons.

Due to the high design luminosity of the LHC, signatures from a hard scatter event

overlap with other proton-proton interactions in the same or in different bunch crossings. Such secondary collisions, referred to as pileup, create a challenging environment for the measurement and identification of the particles originating from the primary interaction. The average number of interaction vertices has increased a lot during the last operation period of the LHC. During 2016 data taking, the average number of interactions was 23, which has further increased in 2017. During 2018, an average of 32 interactions per crossing was recorded. Particles arising from pileup vertices can cause mismeasurements of the properties of hard scatter particles. It is therefore essential to remove the pileup contributions which is done by the charged-hadron subtraction (CHS) method.

4.1 Muons

Information from the CMS muon system as well as from the tracker is used to construct three types of muon candidates. A standalone muon is reconstructed using only detector hits in the DT and CSC detectors of the muon system. If a standalone muon track can be matched to a track that has been reconstructed separately using only tracker hits, it is flagged a global muon. The matching procedure involves comparing the parameters of the tracker and standalone muon tracks, after suitably extrapolating the latter to the tracker system. The high precision momentum measurements of the inner tracker improve the reconstruction of global muons as opposed to standalone muons. A tracker muon, on the other hand, originates when tracks in the inner tracker are propagated to the muon system and matched with tracks there. Only tracks with a total momentum greater than 2.5 GeV and $p_{\mathrm{T}} > 0.5$ GeV are considered. Tracker muon reconstruction shows superior resolution for muons with low transverse momentum. For muons produced within the geometrical acceptance of the muon system, the reconstruction as either tracker muons or global muons performs at a high efficiency of 99%. If a muon is reconstructed by both approaches, the two candidates are merged into a single global muon [47].

Charged hadrons may be misreconstructed as muons e.g. if some of the hadron shower remnants reach the muon system (punch-through). In order to obtain the desired balance between identification efficiency and purity, different identification (ID) criteria can be applied to the muon tracks. The medium muon ID, for instance, is designed to have a high efficiency for prompt muons and muons from heavy flavour decays.

4.2 Electrons and photons

Electrons are reconstructed using ECAL energy clusters that are associated with tracks in the pixel and strip detectors [48]. As the electrons interact with the tracker material, most emit a fraction of their energy in the form of bremsstrahlung photons before reaching the ECAL. Furthermore, the electrons' large probability to radiate is used

to differentiate them from charged hadrons. Electron reconstruction allows for identifying electrons with a transverse momentum down to 2 GeV. Isolated photons are reconstructed alongside the electrons. However, for photon reconstruction only ECAL information is used.

To obtain an accurate estimate of the electron energy it is necessary to efficiently gather the energy of all radiated photons pertaining to the electron. This is achieved by grouping the ECAL clusters reconstructed in a small window in η and an extended window in ϕ around the electron direction into a so-called supercluster which serves as a seed for the track reconstruction. The energy of a single electron can spread out over several crystals in the ECAL. If the loss of energy of the electron due to bremsstrahlung is small and a central hit in a crystal is produced, the spread will be narrow. For a 120 GeV electron that means about 97% of the energy will be contained in a 5×5 crystal cluster. For such electrons with low energy loss in the tracker, a standard Kalman filter suffices to reconstruct the electron tracks in the tracker volume with roughly the same efficiency as for muons.

Electrons with small transverse momentum have tracks that are significantly bent by the magnetic field. However, the curvature of the electron trajectories changes due to emitted bremsstrahlung photons. Therefore, the matching of electron tracks in the silicon detector to superclusters in the ECAL is challenging. The radiated energy for low p_{T} electrons is spread over an extended region. Hence, their superclusters may not include all the energy deposits and fail to be successfully matched to tracker hits. For this reason, also a tracker-based electron seeding method was developed in the context of PF reconstruction. A gaussian sum filter is used to refit the track information from both tracker- and ECAL-based approaches which allows to better model radiative losses due to bremsstrahlung.

4.3 Jets

In particle physics experiments, the particles resulting from a hadronisation cascade of an initial quark or gluon are collected as jets. A jet is a cone of particles such as charged or neutral hadrons (mostly $\pi^{\pm}$, $\mathrm{K}^{\pm}$, protons, or K^0, neutrons, respectively), non-isolated photons (from π^0 decays) or electrons and muons (from heavy-flavoured hadron decays). Jets are reconstructed from PF objects using the anti-k_t jet clustering algorithm [49] with a cone radius parameter of $R = 0.4$. Charged hadrons are reconstructed using energy clusters in the HCAL and tracker information. Photons and neutral hadrons are identified by selecting calorimeter clusters which are not linked to a track in the tracker system. ECAL clusters without a linked HCAL cluster are assumed to arise from photons, while linked clusters between the calorimeters are considered as hadrons. Outside of the tracker acceptance, where $|\eta| > 2.5$, neutral and charged hadrons cannot be distinguished [46]. On average, most of the energy is carried by charged hadrons ($\approx 60\%$), photons ($\approx 25\%$) and neutral hadrons ($\approx 10\%$).

There are various factors that can lead to differences between the energies of the

clustered jets and the actual parton energies. However, physics analyses rely heavily on a high jet energy resolution (JER) and the correct jet energy scale (JES). For that reason, jets are scrupulously calibrated using both data and simulation [50]. The resulting jet energy corrections (JEC) are formulated as multiplicative corrections to the four momentum. Using simulated event samples, the energy offset induced by pileup and noise is corrected. Inhomogeneities in the detector response are corrected by comparing reconstructed jets with simulated jets. The corrections are derived as functions of jet p_{T} and η. In a final step, residual corrections for differences between data and simulation are applied. Eventually, the total uncertainty of the JECs for a jet with 100 GeV transverse momentum is around 1% and a few percent for low-p_{T} jets [51].

4.3.1 *b*-tagged jets

Due to long-lived B mesons, jets that are arising from bottom quarks[1] can be identified, which is known as the process of *b*-tagging jets. This is particularly useful for physics analyses. The presence of jets originating from a bottom quark can give important insights into the nature of the preceding hard scatter, since the decay of top quark into bottom quarks is the dominant source for these jets in the SM.

The *b*-tagging algorithm takes advantage of the presence of secondary vertices (SV) and displaced tracks from B meson decay. They are a result of the relatively long lifetime of hadrons containing bottom quarks which leads to a decay within the tracker system. Typical values for the distance between the primary and secondary vertex are 450 μm (for comparison, the spatial resolution of reconstructed PVs is 12 μm [47]). The latest *b*-tagging algorithm used in CMS analyses is based on machine learning techniques using deep neural networks and is called DeepCSV, where CSV stands for combined SV algorithm [52]. To compensate for differences in *b*-tagging efficiency between data and simulation, scale factors are applied to simulated events. These scale factors are measured using data control samples and lead to a good agreement of the *b*-tagged jet multiplicity distribution between data and simulation.

4.4 Missing transverse energy

Not all particles can be directly detected. For instance, as neutrinos only interact weakly, they can escape all layers of the detector without leaving any trace. Furthermore, hypothetical weakly interacting BSM particles such as neutralinos are also invisible. Such particles, however, may have a significant momentum and can be detected indirectly by observing the resulting momentum imbalance of the observed particles. This quantity is known as missing momentum. It must be stressed that momentum conservation can only be exploited in the transverse plane due to the unaccessability

[1] To a limited extent also jets arising from charm quarks will be *b*-tagged.

of the colliding hadrons' initial momenta. Therefore, the relevant quantity that can be reconstructed is the missing transverse momentum $\boldsymbol{p}_{\mathrm{T}}^{\mathrm{miss}}$. In most CMS analyses it is determined to be the negative vectorial sum of transverse momenta $\boldsymbol{p}_{\mathrm{T},i}$ of all final state particles reconstructed via the PF algorithm, i.e.

$$\boldsymbol{p}_{\mathrm{T}}^{\mathrm{miss}} = -\sum_{i}^{\text{PF candidates}} \boldsymbol{p}_{\mathrm{T},i}\,.$$

An accurate calculation of magnitude and direction of the $p_{\mathrm{T}}^{\mathrm{miss}}$ relies on a precise reconstruction of all detectable particles. There are various sources that lead to an imprecise reconstruction of $\boldsymbol{p}_{\mathrm{T}}^{\mathrm{miss}}$, such as energy and p_{T} thresholds for calorimeter and tracker systems and nonlinearities in the detector response. The scale and resolution of $p_{\mathrm{T}}^{\mathrm{miss}}$ are measured in events with no genuine $p_{\mathrm{T}}^{\mathrm{miss}}$ such as events where a Z boson decays into two leptons. To further improve $\boldsymbol{p}_{\mathrm{T}}^{\mathrm{miss}}$ measurements, jet corrections, for instance due to pileup interactions, can be propagated into the calculation of $\boldsymbol{p}_{\mathrm{T}}^{\mathrm{miss}}$. The $p_{\mathrm{T}}^{\mathrm{miss}}$ observable is of paramount importance for BSM searches that predict the production of highly energetic weakly interacting particles.

5 | Search for supersymmetry in dilepton final state

This thesis describes the search for supersymmetry (SUSY), in particular top squark pair production in events with exactly two charged leptons (electrons or muons) in the final state. Furthermore, only events with at least two jets, at least one of which is required to be a b-tagged jet, are considered. The analysis is based on pp collision data at a center of mass energy of 13 TeV, taken at the CMS experiment between the years 2016 and 2018 and amounting to an integrated luminosity of 137.37 fb^{-1}. An earlier analysis using only 2016 data has already been conducted in [53]. The search is designed to be sensitive to the models `T2tt`, `T2bW` and `T8bbllnunu`, which are described in detail in Sec. 1.3.6. The analysis methods, that will be discussed in the following, make use of the distinct kinematical features of those signal models. In Section 5.1 samples for data, simulated backgrounds and signals, correction factors (weights) for simulations, as well as event filters will be described. Section 5.2 introduces the event selection of the analysis. The definition of signal and control regions is presented in Section 5.3. In Section 5.4, the systematic uncertainties affecting the analysis will be described in detail. Furthermore, background estimation methods are discussed in Section 5.5. Eventually, the results and the statistical methods for interpretations will be presented in Section 5.6. The observed data showed no significant excess over the predicted SM background, and the results are interpreted in several SUSY models in order to set limits on the top squark–neutralino mass plane.

5.1 Data and simulated samples

For the success of an analysis it is essential to have an accurate understanding of the SM *backgrounds*, which contribute to final states and resemble the signal. In order to develop and validate the background estimation method, as well as testing the background+signal hypothesis, simulated samples are used. Samples for background and signal processes are generated using Monte Carlo (MC) techniques on a per-event basis. Not only the hard scatter from the proton-proton collision is simulated but also the detector response and the reconstruction algorithms. The essential input for the simulation of proton collisions are parton distribution functions (PDFs) that describe the momenta of the incoming partons. In particular, they represent the probability

for a parton to carry a certain fraction of proton momentum at a certain energy scale. PDFs are determined empirically using QCD perturbation theory. This is possible since the hard scatter process involves high momentum transfer induced by the LHC's high energies. In that regime partons can be considered to be asymptotically free. Events are simulated up to leading (LO) or next-to-leading order (NLO) in perturbation theory using the POWHEG [54, 55] or MADGRAPH [56] programs. The parton showering and hadronisation is handled by PYTHIA8 [57]. Finally, GEANT4 [58] is used to simulate the response of the CMS detector to the generated particles.

Correction factors for simulation

In order to suitably compare the simulated samples with data, event weights w are introduced. They are calculated as the ratio of the expected number of events N_{exp} (cf. Eq. (2.1)) and the total number of simulated events N_{sim},

$$w = \frac{N_{\text{exp}}}{N_{\text{sim}}} = \frac{\sigma}{N_{\text{sim}}} \int \mathcal{L}\,\mathrm{d}t\,, \tag{5.1}$$

where σ denotes the cross section of the event and $\int \mathcal{L}\,\mathrm{d}t$ the integrated luminosity of the detector data. The present analysis uses collision data corresponding to an integrated luminosity of 137.37 fb^{-1}.

Remaining differences between data and simulation are handled by extra factors multiplied to the event weight. For example, the mismodelling of the number of inelastic scatterings per bunch crossing (pileup) is corrected for by mimicking the observed values in data via a pileup reweighting factor. Inefficiencies of lepton tracking, lepton identification and the dilepton trigger are all corrected for via dedicated weights in the simulated sample. Besides, differences in the b-tagging efficiency between data and simulation are handled on a per-event basis. Also events with pre-firing in the L1 trigger signal, caused by remnant interactions from the previous bunch crossing in the hadron calorimeter, are taken care of via a weight. During the 2018 data taking period part of the HEM calorimeter was not powered and failed to record data. This affects about 64.8% of the 2018 data set. A dedicated weight therefore vetoes events with a jet in the HEM region (i.e. the affected detector region plus some extra margin: $-3.2 < \eta < -1.0$ and $-2.0 < \phi < -0.5$) in data and simulation. Signal samples, describing SUSY events, also use all the just mentioned weights and an additional one for an initial state radiation (ISR) modelling correction.

Event cleaning filters

During data taking, some events may be contaminated with detector or reconstruction effects [59] that result in anomalous events with large values of $p_{\text{T}}^{\text{miss}}$. Such events can be caused by dead cells in the ECAL, fake energy deposits due to noise or beam halo particles. A set of algorithms, called $p_{\text{T}}^{\text{miss}}$ filters, has been developed to suppress these kind of events in the data. The ones used in this analysis are:

- HBHE noise and isolation noise filter to veto noise in the HCAL,
- ECAL trigger primitive filter to filter events with saturation in the reconstructed energy for certain crystals where only a low granularity readout is available,
- primary vertex filter that requires at least one reconstructed primary vertex of high quality, and
- beam halo filter to remove events with deposits from beam halo particles.

Triggers

In order to achieve an optimal event selection efficiency for this analysis, various sets of high level triggers (HLTs) are used to trigger dileptonic events. For each of the three dilepton channels (ee, $\mu\mu$ and $e\mu$) the logical OR of the dilepton triggers is taken. Isolated and non-isolated triggers are combined. Moreover, the partially inefficient dilepton triggers are complemented by single lepton triggers. Of course, this introduces an overlap between two primary data sets or potentially even three in the case of the $e\mu$ channel. This overlap in the ee and $\mu\mu$ channels is removed by vetoing events that fired a dilepton trigger in the single lepton primary data sets. The potential overlap of the dilepton and the two complementing single lepton primary data sets for the $e\mu$ channel is gotten rid of in two steps. First, events from the single electron primary data set are added that fired single electron triggers but failed the double lepton triggers. Second, events from the single muon primary data set are added that fired single muon triggers but fired none of the triggers used to select events in the other two primary data sets. The gain of adding single lepton triggers has been studied in the preceding analysis [53] using only 2016 data.

The trigger efficiencies are measured and used to scale the simulation. There is an inefficiency for muons with high transverse momentum in the muon system's endcaps in 2016 data, hence the trigger inefficiency is parametrised as a function of both lepton momenta. This is done in two bins of the η distribution of the leading lepton defined as $|\eta| \gtrless 1.5$. In the $e\mu$ channel, the measurement is binned similarly but the η value is always taken from the muon, whether it is leading or not. Figure 5.1 shows the trigger efficiencies inclusively in the leading lepton's $|\eta|$.

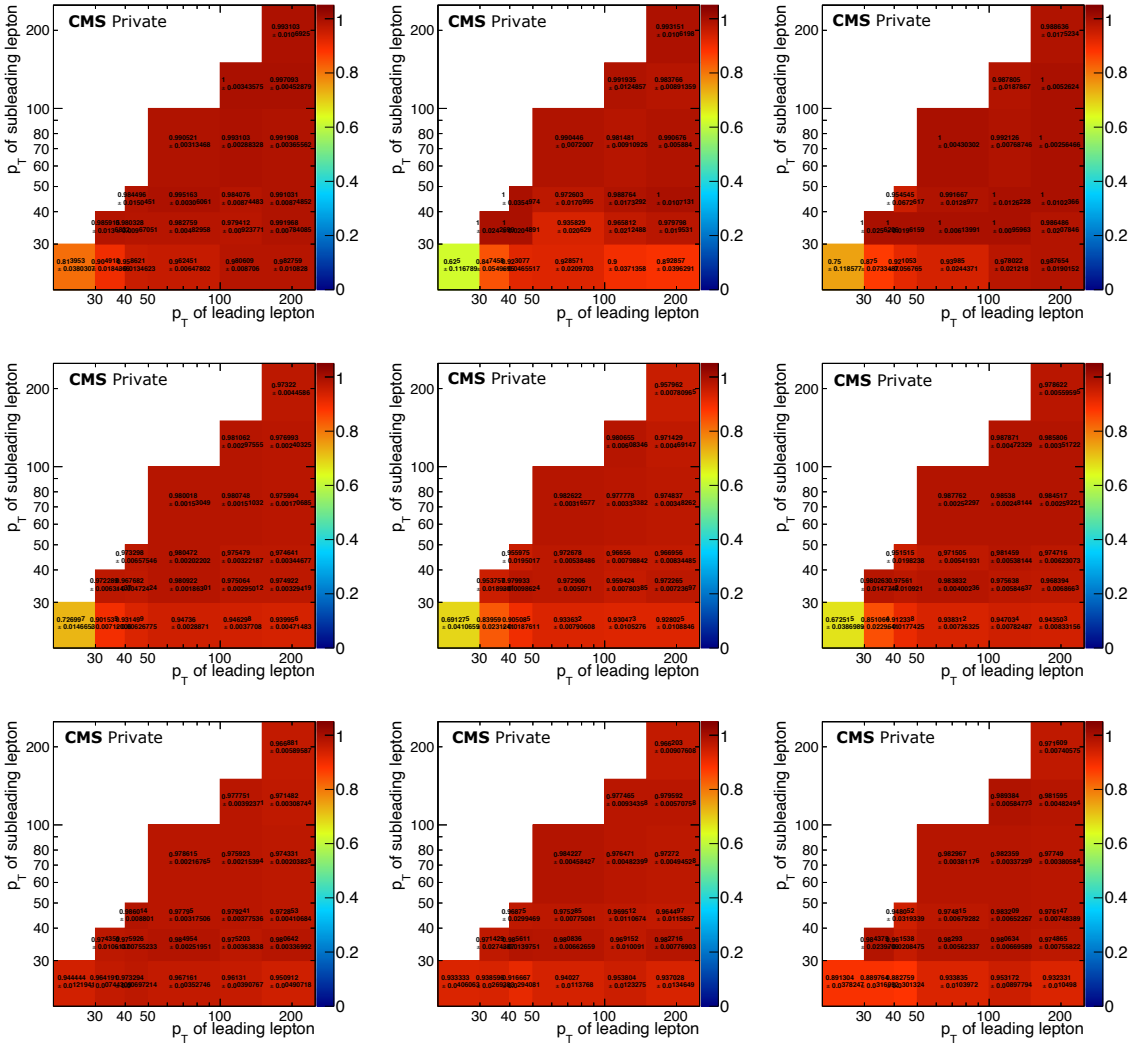

Figure 5.1: Trigger efficiencies for the ee (top), $e\mu$ (center) and $\mu\mu$ (bottom) channel, for 2016, 2017 and 2018 (from left to right).

5.2 Event selection

The present analysis targets top squark pair production. As introduced in Section 1.3.6, the signal models that are considered here all contain a neutralino as the LSP in the final state. Further decay products include top quarks for `T2tt`, bottom quarks and W bosons for `T2bW`, and bottom quarks, neutrinos and dileptons for `T8bbllnunu`. All of those models have a significant branching ratio into a dilepton (i.e. two leptons) final state emerging from the decay products of the W bosons. For `T8bbllnunu`, the branching fraction is 100%, as the leptons (including τ leptons) are part of its cascade decay chain. Therefore, this model exclusively focusses on events with two isolated (and oppositly charged) leptons in the final state. Furthermore, since all signal models predict bottom quarks (the top quark in `T2tt` decays into a bottom quark and a W boson) at least two jets per event are required in this search. At least one of the jets is required to be b-tagged.

5.2.1 Search strategy

The general strategy pursued by searches for new physics at the LHC is to select events according to the specific kinematic properties of the signal model(s). In particular, a search is designed to be sensitive to a range of model parameter values, i.e. particle masses in the case of SMS. Using the kinematic features of the signal models, *signal regions* (SRs) and *control regions* (CRs) are defined. The signal regions are chosen such that the kinematical features of the signal model are utilised to their full advantage. The control regions are regions where the signal contribution is small. Hence, they are largely dominated by SM background. Signal and control regions are defined without overlap using the $M_{\mathrm{T2}}(\ell\ell)$, $M_{\mathrm{T2}}(b\ell b\ell)$ and $p_{\mathrm{T}}^{\mathrm{miss}}$ significance variables. Those variables will be described in detail in the following. The observed data in the control regions is utilised to estimate the contribution of the SM processes in the signal regions. Subsequently, the compatibility of the observed data in the signal regions with the background-only and the background+signal hypotheses is tested using a maximum likelihood-based approach. To this end, it is essential to take all relevant (systematic) uncertainties for signal and background processes into account. In the following, the variables that are used to define signal and background regions are discussed.

Stransverse mass variables

The stransverse mass variable $M_{\mathrm{T2}}(\ell\ell)$ [60] is used to separate the top squark signal from the SM background, which consists primarily of a top-antitop quark pair decaying into dileptons (referred to as a $t\bar{t}$ event; its Feynman diagram is depicted in Fig. 5.13a). The stransverse mass is a generalisation of the transverse mass m_{T} to a system of pair produced particles that decay semi-invisibly[1]. In the case of W boson decay, m_{T} is

[1]Note that particles that are invisible to the detector, such as neutrinos or the hypothetical neutralinos, produce $p_{\mathrm{T}}^{\mathrm{miss}}$.

formed from the transverse momentum of a high p_{T} lepton (from the W decay) and the missing transverse momentum ($p_{\mathrm{T}}^{\mathrm{miss}}$) in the event, which is assumed to come from the corresponding neutrino. In the limit where the masses of the daughter particles can be neglected the transverse mass m_{T} is given by

$$m_{\mathrm{T}} = \sqrt{2\, p_\ell\, p_{\mathrm{T}}^{\mathrm{miss}}\, (1 - \cos(\Delta\phi))}\,.$$

Furthermore, a useful property of the transverse mass is that if the lepton and the $p_{\mathrm{T}}^{\mathrm{miss}}$ both come from the decay of a single mother particle with mass m then this mass serves as an upper bound for the transverse mass, i.e. $m_{\mathrm{T}} \leq m$. This notion is generalised to a system with two particles of the same mass, each decaying semi-invisibly. First of all, the measured $p_{\mathrm{T}}^{\mathrm{miss}}$ is decomposed into a sum of two missing transverse momentum vectors according to

$$\mathbf{p}_{\mathrm{T}}^{\mathrm{miss}} = \mathbf{p}_{\mathrm{T1}}^{\mathrm{miss}} + \mathbf{p}_{\mathrm{T2}}^{\mathrm{miss}}. \tag{5.2}$$

Subsequently, each missing transverse momentum vector is again paired with the visible products of the decay in order to compose m_{T} for each branch of the pair production. Of course, the correct separation of the $p_{\mathrm{T}}^{\mathrm{miss}}$ into two parts is unknown. Therefore, a good approach is to first maximise the two transverse masses for every possible combination satisfying Eq. (5.2) and then obtain the minimum of all those maximum values. That means that, effectively, the parameter space of all possible hypothetical neutrino momenta that satisfy Eq. (5.2) is explored and for each point in this parameter space m_{T} is calculated for each branch. What then enters the minimisation procedure is the higher m_{T} value of the two branches. The resulting variable is denoted by $M_{\mathrm{T2}}\,(\ell\ell)$ and expressed as

$$M_{\mathrm{T2}}^2(\ell\ell) = \min_{\mathbf{p}_{\mathrm{T1}}^{\mathrm{miss}} + \mathbf{p}_{\mathrm{T2}}^{\mathrm{miss}} = \mathbf{p}_{\mathrm{T}}^{\mathrm{miss}}} \left(\max \left[m_{\mathrm{T}}^2(\mathbf{p}_{\mathrm{T}}^{\ell_1}, \mathbf{p}_{\mathrm{T1}}^{\mathrm{miss}}),\ m_{\mathrm{T}}^2(\mathbf{p}_{\mathrm{T}}^{\ell_2}, \mathbf{p}_{\mathrm{T2}}^{\mathrm{miss}}) \right] \right)\,. \tag{5.3}$$

It can be shown [60] that the definition of $M_{\mathrm{T2}}\,(\ell\ell)$ has the same convenient property as the transverse mass. Namely, that $M_{\mathrm{T2}}\,(\ell\ell)$ is at most equal to the mass of one of the pair-produced semi-invisibly decaying particles.

In the case of the top squark search in the dilepton channel discussed here, the main challenge comes from separating the SM's $t\bar{t}$ production from the signal, since the composition of the final states is identical except for invisible particles. The final state for dileptonic $t\bar{t}$ events results from the decay chain

$$pp \to t + \bar{t} + X \to b\, W^+ + \bar{b}\, W^- + X \to b\, \bar{\ell}\nu_\ell + \bar{b}\, \ell\bar{\nu}_\ell + X\,.$$

The contribution of the other products X to the $p_{\mathrm{T}}^{\mathrm{miss}}$ is assumed to be moderately small. Then, the assumptions made in the definition of $M_{\mathrm{T2}}\,(\ell\ell)$ hold for the lepton-$p_{\mathrm{T}}^{\mathrm{miss}}$ system and its value has an upper bound at the W mass. Top squark pair production events with a dileptonic final state, on the other hand, will have at least four invisible particles, so long as both lepton number and R-parity are conserved. Depending on the exact model considered, top squark decays can proceed differently. A typical example for the models used here is called `T2tt`, which presents the decay

$$pp \to \tilde{t} + \bar{\tilde{t}} + X \to \bar{\tilde{\chi}}_1^0\, t + \tilde{\chi}_1^0\, \bar{t} + X \to \bar{\tilde{\chi}}_1^0\, b\, W^+ + \tilde{\chi}_1^0\, \bar{b}\, W^- + X \to \bar{\tilde{\chi}}_1^0\, b\, \bar{\ell}\nu_\ell + \tilde{\chi}_1^0\, \bar{b}\, \ell\bar{\nu}_\ell + X\,.$$

In this case, there are now two invisible particles on each branch of the decay. Hence the division of the $p_{\mathrm{T}}^{\mathrm{miss}}$ into two components no longer has an upper bound at the W mass, which illustrates the discriminative power of $M_{\mathrm{T2}}(\ell\ell)$ for this analysis. For visualisation, the $M_{\mathrm{T2}}(\ell\ell)$ distribution is shown in Fig. 5.2.

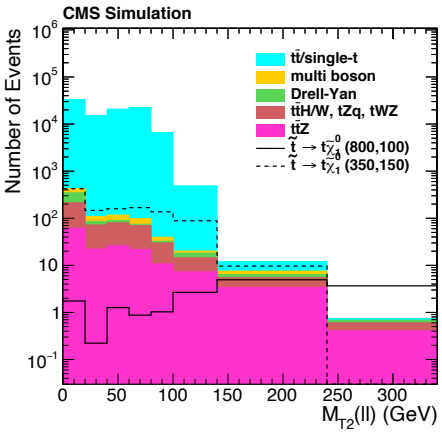

Figure 5.2: $M_{\mathrm{T2}}(\ell\ell)$ distribution showcasing its disriminative power. $t\bar{t}$ (light blue) has an upper bound at the W boson mass around 100 GeV, while the signals (black lines) show no upper bound.

In a similar fashion, another variant of the $M_{\mathrm{T2}}(\ell\ell)$ variable can be constructed, also taking b-jets into account, namely

$$M_{\mathrm{T2}}^2(b\ell b\ell) = \min_{\mathbf{p}_{\mathrm{T1}}^{\mathrm{miss}}+\mathbf{p}_{\mathrm{T2}}^{\mathrm{miss}}=\mathbf{p}_{\mathrm{T}}^{\mathrm{miss}}} \left(\max_{b\in b_1,b_2;\,\ell\in\ell_1,\ell_2} \left[m_{\mathrm{T}}^2(\mathbf{p}_{\mathrm{T}}^{b}+\mathbf{p}_{\mathrm{T}}^{\ell}, \mathbf{p}_{\mathrm{T1}}^{\mathrm{miss}}) \right] \right) .$$

With reasoning analogous as above, $M_{\mathrm{T2}}(b\ell b\ell)$ is expected to have an upper bound at the top quark mass. Of course, some events contain one or even zero b-tagged jets. In such cases, the highest p_{T} jets failing the b-tagging requirement are taken instead. Furthermore, there are two possible ways to pair the two leptons and the two b-jets in $M_{\mathrm{T2}}(b\ell b\ell)$. However, by minimising the maximum invariant mass of the two lepton-jet pairs, this ambiguity is resolved.

MET significance

Besides $M_{\mathrm{T2}}(\ell\ell)$ and $M_{\mathrm{T2}}(b\ell b\ell)$, $p_{\mathrm{T}}^{\mathrm{miss}}$ significance, denoted by $\mathcal{S}$, serves as another discriminating variable in this analysis. As the signals involve large amounts of $p_{\mathrm{T}}^{\mathrm{miss}}$, it is critical to obtain the ability to distinguish between events with intrinsic $p_{\mathrm{T}}^{\mathrm{miss}}$ and ones with spurious $p_{\mathrm{T}}^{\mathrm{miss}}$. The $p_{\mathrm{T}}^{\mathrm{miss}}$ significance variable aids in making this distinction on a per event basis, unaffected by any hadronic activity in the event. The computation of $\mathcal{S}$ utilises the reconstructed $p_{\mathrm{T}}^{\mathrm{miss}}$, jets, leptons, as well as low-p_{T} hadronic activity (i.e. PF candidates not clustered in jets) in each event. The $p_{\mathrm{T}}^{\mathrm{miss}}$ significance variable turns out to be applicable to a variety of event topologies at CMS. More details on the $\mathcal{S}$ variable can be found in [61, 62].

Another reason why $\mathcal{S}$ is used here instead of the $p_{\mathrm{T}}^{\mathrm{miss}}$ variable itself is that the acceptance of Drell-Yan (DY) events after a $p_{\mathrm{T}}^{\mathrm{miss}}$ requirement strongly depends on pileup (PU), as will be discussed later in some more detail. In the 2016 data set, where the mean PU was sufficiently low, a $p_{\mathrm{T}}^{\mathrm{miss}} > 80$ GeV requirement efficiently removes DY events. This is not the case for 2017 and 2018, however. There, the PU dependence would subsequently lead to systematic uncertainties in the DY/Multiboson control region yields from the uncertainty in the minimum bias cross section, for example. These CRs are used to measure scale factors and accuracy thus indirectly suffering from varying PU conditions. To overcome this issue, $p_{\mathrm{T}}^{\mathrm{miss}}$ significance, which has been first described in [61], is used instead of $p_{\mathrm{T}}^{\mathrm{miss}}$. It turns out that $\mathcal{S}$ thresholds and $p_{\mathrm{T}}^{\mathrm{miss}}$ thresholds are somewhat comparable in terms of sensitivity but that the former is much more stable against PU, especially for the 2017 and 2018 data sets.

$p_{\mathrm{T}}^{\mathrm{miss}}$ significance is defined as the log-likelihood ratio

$$\mathcal{S} \equiv 2 \ln \left(\frac{\mathcal{L}(\boldsymbol{\varepsilon} = \sum \boldsymbol{\varepsilon}_i)}{\mathcal{L}(\boldsymbol{\varepsilon} = 0)} \right), \tag{5.4}$$

where the $\boldsymbol{\varepsilon}$ is the *true* $p_{\mathrm{T}}^{\mathrm{miss}}$ and $\sum \boldsymbol{\varepsilon}_i$ is the *observed* $p_{\mathrm{T}}^{\mathrm{miss}}$. The numerator contains the likelihood evaluated for the case that the true value of $p_{\mathrm{T}}^{\mathrm{miss}}$ equals the observed value, while the denominator corresponds to the *null hypothesis*, which assumes the true $p_{\mathrm{T}}^{\mathrm{miss}}$ to be zero. Furthermore, the likelihood $\mathcal{L}(\boldsymbol{\varepsilon})$ takes on the shape of a Gaussian distribution to a good approximation. Therefore, the significance can be written as

$$\mathcal{S} = \big(\sum \boldsymbol{\varepsilon}_i \big)^{\dagger} \, \mathbf{V}^{-1} \, \big(\sum \boldsymbol{\varepsilon}_i \big). \tag{5.5}$$

Here, $\mathbf{V}$ is the 2×2 $p_{\mathrm{T}}^{\mathrm{miss}}$ covariance matrix. Moreover, it turns out that for events with zero true $p_{\mathrm{T}}^{\mathrm{miss}}$, $\mathcal{S}$ follows a χ^2 distribution with two degrees of freedom (one degree of freedom for each component of $p_{\mathrm{T}}^{\mathrm{miss}}$), as can be seen in Fig. 5.4.

The covariance matrix $\mathbf{V}$ in Eq. (5.5) models the $p_{\mathrm{T}}^{\mathrm{miss}}$ resolution smearing in each event. In order to construct the covariance $\mathbf{V}$, the respective resolutions of the objects entering the $p_{\mathrm{T}}^{\mathrm{miss}}$ sum are propagated to it. The $p_{\mathrm{T}}^{\mathrm{miss}}$ resolution entering into $\mathbf{V}$ is primarily determined by the hadronic components of the event. In particular, this includes jets above a threshold $p_{\mathrm{T,\,min}}^{\mathrm{jet}}$, and "unclustered energy", which refers to objects that are not contained in any jet. The transverse momentum of jets below the threshold $p_{\mathrm{T,\,min}}^{\mathrm{jet}}$ is added to the unclustered energy. Jets enter into the total covariance $\mathbf{V}$ with an individual covariance of the form

$$\mathbf{U} = \begin{pmatrix} \sigma_{p_{\mathrm{T}}}^2 & 0 \\ 0 & p_{\mathrm{T}}^2 \, \sigma_{\phi}^2 \end{pmatrix}, \tag{5.6}$$

where the quantities $\sigma_{p_{\mathrm{T}}}$ and σ_{ϕ} are measured and subsequently re-tuned with a combination of simulation and data driven techniques. The momenta from all objects not included in the jets are summed vectorially. The resulting momentum is then assigned into a single object with $\boldsymbol{p}_{\mathrm{T}} = \sum_i \boldsymbol{p}_{\mathrm{T},i}$. The resolution of this object is parametrised by the scalar sum over the p_{T} of its constituents

$$\sigma_{uc}^2 = \sigma_0^2 + \sigma_s^2 \sum_{i=1}^{n} |\boldsymbol{p}_{\mathrm{T},i}|. \tag{5.7}$$

The values of σ_0^2 and σ_s^2 are determined using a data driven technique, see also [62]. The resolution of this object is assumed to be isotropic in the transverse plane of the detector. The reconstructed leptons are assumed to have perfect resolutions compared to the hadronic components in the same event. Therefore, they make no contribution to the covariance $\mathbf{V}$.

Unclustered energy, i.e. PF candidates that are not clustered into jets, is treated as a pseudo-jet. Its isotropic resolution in the transverse plane is only proportional to its magnitude, while the spatial configuration is assumed not to play a role. This method of encapsulating unclustered energy is robust to different pileup scenarios, as shown in Fig. 5.3.

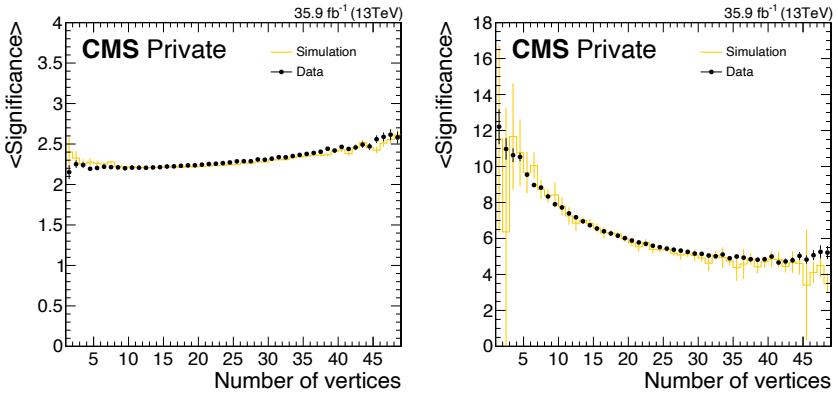

(a) dimuon events **(b)** single-electron events

Figure 5.3: Dependence of the average significance $\mathcal{S}$ on pileup, for dimuon events and single-electron events. For processes with no genuine $p_{\mathrm{T}}^{\mathrm{miss}}$ a small dependence is observed, whereas in events with intrinsic $p_{\mathrm{T}}^{\mathrm{miss}}$ the behavior of $\mathcal{S}$ depends strongly on pileup.

The parameters for jets and unclustered energy are determined by maximising the likelihood $\mathcal{L}(\boldsymbol{\epsilon} = 0)$ which is equivalent to minimising

$$-2\mathcal{L}(\boldsymbol{\epsilon} = 0) = \mathcal{S} + \log(\det \mathbf{V})\,. \tag{5.8}$$

The likelihood fit is performed in a $Z \to \mu\mu$ selection, separately for data and simulation. For jets with a transverse momentum $p_{\mathrm{T}} > p_{\mathrm{T,\,min}}^{\mathrm{jet}}$ the jet resolution scale parameters are binned in terms of jet η and p_{T}.

The parameters that have been obtained as a result of the tuning for the 2016-2018 data taking periods are shown in Table 5.1. In order to obtain a good agreement between data and simulation in $t\bar{t}$ enriched samples, a binning in jet p_{T} was found to be necessary in the 2017 data taking period. The same strategy was used in 2018, while for 2016 an inclusive jet p_{T} bin was used. The $p_{\mathrm{T,\,min}}^{\mathrm{jet}}$ threshold is 15 GeV for 2016 and 2017 data, and 25 GeV for 2018 data. The fully tuned $\mathcal{S}$ observable in a dilepton selection with a requirement of at least two jets and an invariant mass of the leptons within a 15 GeV window of the Z boson mass is shown in Fig. 5.4.

Table 5.1: Parameters modifying σ_{p_T} in the covariance matrix for jets in bins of $|\eta|$, as well as parameters used for the covariance matrix of the unclustered energy. Values are given separately for simulation and data.

Parameter	$\lvert\eta\rvert$	p_T	MC simulation			data		
			2016	2017	2018	2016	2017	2018
	0 – 0.8	<40 GeV	1.62	1.96	1.90	1.84	2.23	1.75
		≥ 40 GeV		1.53	1.74		1.24	1.34
	0.8 – 1.3	<40 GeV	1.45	1.92	1.70	1.64	2.23	1.91
		≥ 40 GeV		1.51	1.73		1.26	1.37
	1.3 – 1.9	<40 GeV	1.41	1.81	1.59	1.57	2.02	1.59
		≥ 40 GeV		1.32	1.53		1.16	1.44
	1.9 – 2.5	<40 GeV	1.41	1.55	1.37	1.51	1.74	1.52
		≥ 40 GeV		1.27	1.45		1.16	1.45
	>2.5	<40 GeV	1.36	1.51	1.48	1.61	1.94	1.89
		≥ 40 GeV		1.65	1.45		1.87	1.71
σ_0			0	0	0	0	0	0
σ_s			0.65	0.66	0.69	0.61	0.65	0.74

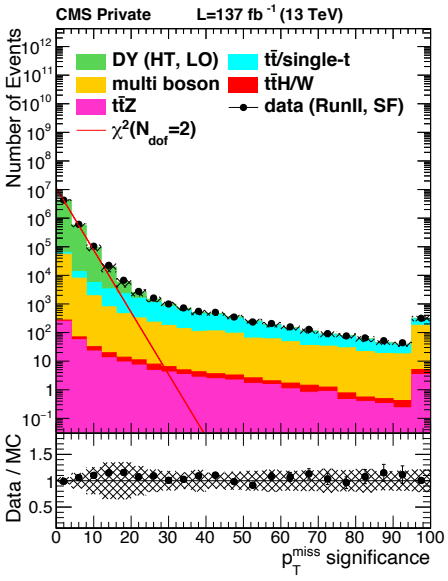

Figure 5.4: Distribution of $\boldsymbol{p}_{\mathrm{T}}^{\mathrm{miss}}$ significance in a $Z \to \ell\ell$ selection, requiring at least two jets, none of which is b-tagged. Events with no genuine $\boldsymbol{p}_{\mathrm{T}}^{\mathrm{miss}}$ like Drell-Yan follow a χ^2 distribution with two degrees of freedom (red line).

MET significance and pileup

Figure 5.5 illustrates the fact that for CMS's 2017 and 2018 data sets the average pileup increased significantly compared to the 2016 data set. It was found that Drell-

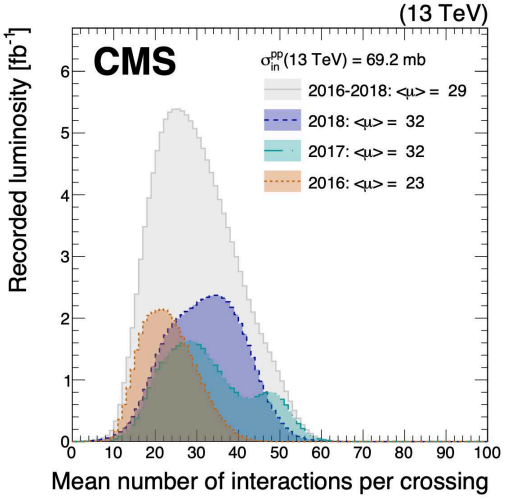

Figure 5.5: Pileup distributions for 2016, 2017, and 2018 [63].

Yan acceptance is particularly sensitive to the modelling of $p_{\mathrm{T}}^{\mathrm{miss}}$ mismeasurements and hence also to the amount and details of deposits from PU in the event. A sizeable systematic uncertainty will arise in the DY control regions from the uncertainty on the minimum bias cross section.

The missing transverse energy $p_{\mathrm{T}}^{\mathrm{miss}}$ and the "kinematical" $p_{\mathrm{T}}^{\mathrm{miss}}$ significance ($p_{\mathrm{T}}^{\mathrm{miss}}/\sqrt{H_{\mathrm{T}}}$) variable are shown in Fig. 5.6ab for varying pileup conditions and clearly reveal a large dependence on the amount of PU. The H_{T} variable used here is defined as the scalar sum of all transverse jet momenta, i.e. $H_{\mathrm{T}} = \sum_i^{\mathrm{jets}} p_{\mathrm{T},i}$. The $\mathcal{S}$ variable, on the other hand, is shown in Fig. 5.6c and has a much better behaved PU dependence. This makes the case for the use of the $\mathcal{S}$ variable as opposed to plain $p_{\mathrm{T}}^{\mathrm{miss}}$ which was used in the preceding analysis [53] with the 2016 data set.

For this analysis, a lower threshold of $\mathcal{S} > 12$ is set as part of the preselection. This lower threshold mostly serves to reduce the DY background by several orders of magnitude, as can be seen in Fig. 5.7. The upper threshold is defined as $\mathcal{S} > 50$ and helps to improve sensitivity to signals with a large mass gap and high expected values for $p_{\mathrm{T}}^{\mathrm{miss}}$ (and hence $M_{\mathrm{T2}}(\ell\ell)$).

The sensitivity of the two thresholds was checked for different values respectively, as well as in comparison to the sensitivity of the 2016 analysis [53] using $p_{\mathrm{T}}^{\mathrm{miss}}$ thresholds. Variation of the lower threshold induces little variation since the $M_{\mathrm{T2}}(\ell\ell) > 100$ GeV threshold used to define the SRs almost entirely removes DY events. For the upper threshold, the sensitivity varies very slightly. Overall, the main benefit of using $\mathcal{S}$ is its big impact on stability, not so much on sensitivity. Furthermore, Fig. 5.8 shows a comparison of the expected limits on the cross section in the top squark–neutralino

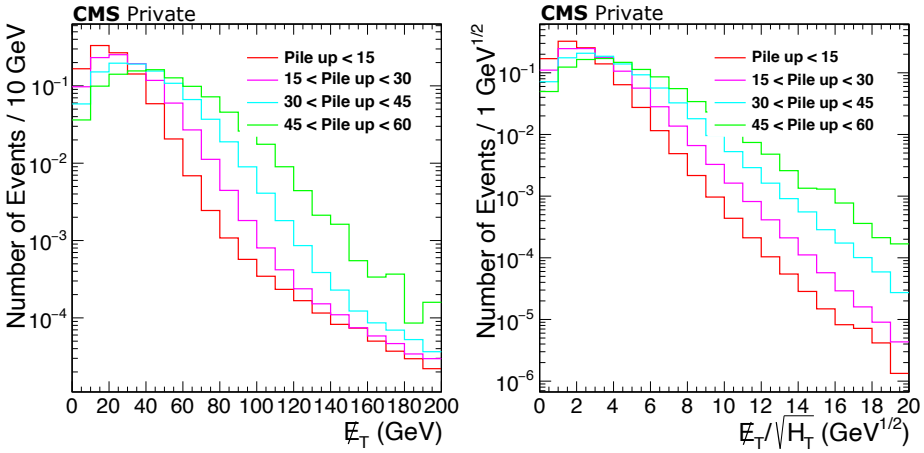

(a) $p_{\mathrm{T}}^{\mathrm{miss}}$ **(b)** "kinematical" $p_{\mathrm{T}}^{\mathrm{miss}}$ significance

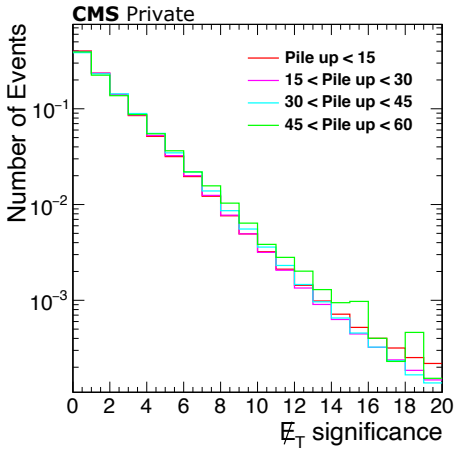

(c) $\mathcal{S}$

Figure 5.6: Distribution of $p_{\mathrm{T}}^{\mathrm{miss}}$, the "kinematical" $p_{\mathrm{T}}^{\mathrm{miss}}$ significance and $\mathcal{S}$ for varying pileup in 2016 simulation for a least two jets and two leptons consistent with a Z boson.

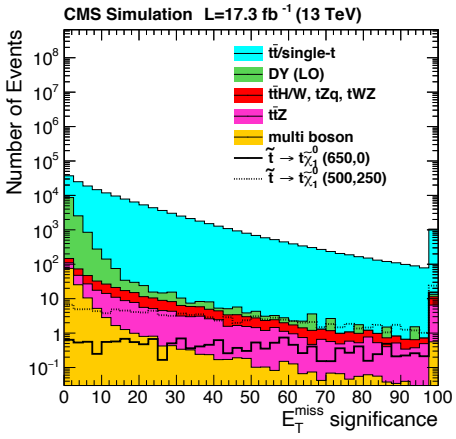

Figure 5.7: Simulated $\mathcal{S}$ distribution after a $N_{\mathrm{jets}} > 2$, $N_{\text{b-jets}} > 1$ preselection.

mass plane between the $p_{\mathrm{T}}^{\mathrm{miss}}$ based analysis [53] and the threshold values or $\mathcal{S} > 12$ and $\mathcal{S} > 100$ used here. There is indeed also an indication of a small improvement in sensitivity.

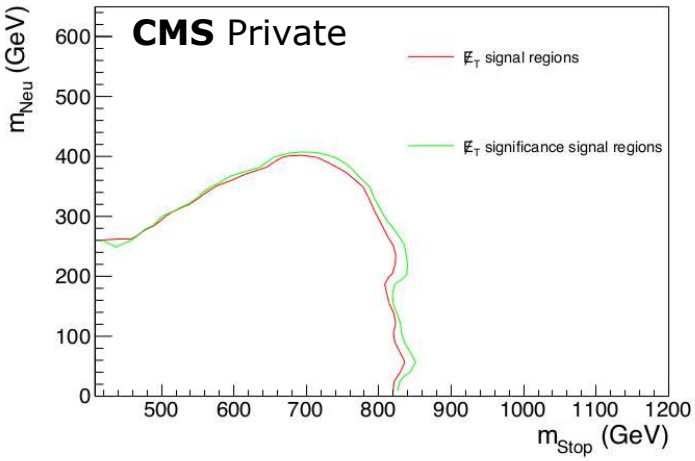

Figure 5.8: Comparison of the expected limits in the $m_{\tilde{t}}$-$m_{\tilde{\chi}_1^0}$ mass plane for the signal regions defined in [53] and the ones in Table 5.5, respectively.

Pileup reweighting

In the 2016 analysis [53] the uncertainty in the efficiency of vetoing Drell-Yan via the $p_{\mathrm{T}}^{\mathrm{miss}}$ requirement turned out to be an important effect. This uncertainty originates from the one in the minimum bias cross section that is used for pileup reweighting. As briefly discussed in Section 5.1, PU reweighting is applied to simulated events in order to match the PU profile in data. This is necessary, since Monte Carlo events are generated before data taking according to an estimated PU profile. The target pileup distribution for data is generated using the instantaneous luminosity per bunch crossing for each luminosity section and a total pp inelastic cross section of 69.2 mb is assumed. The effectiveness of rejecting DY events is very important for the stability of the control regions where DY is a major background, while being almost negligible in the signal regions.

In order to avoid large scale factors for DY events in the $M_{\mathrm{T2}}\,(\ell\ell)$ tail, a good description of high vertex multiplicities presents itself very valuable. Figure 5.9a displays the vertex multiplicity distribution from the 2016 data set after PU reweighting split in bins of $\mathcal{S}$. High vertex multiplicities seem to contribute slightly more in events with low $\mathcal{S}$ which will be removed by the preselection. Conversely, Figs. 5.9bc show $p_{\mathrm{T}}^{\mathrm{miss}}$ and $\mathcal{S}$ in bins of vertex multiplicity. The binned DY component indicates that there seems to be less correlation between $\mathcal{S}$ and vertex multiplicity than between $p_{\mathrm{T}}^{\mathrm{miss}}$ and vertex multiplicity. Since $p_{\mathrm{T}}^{\mathrm{miss}}$ directly enters the main search variable in this analysis,

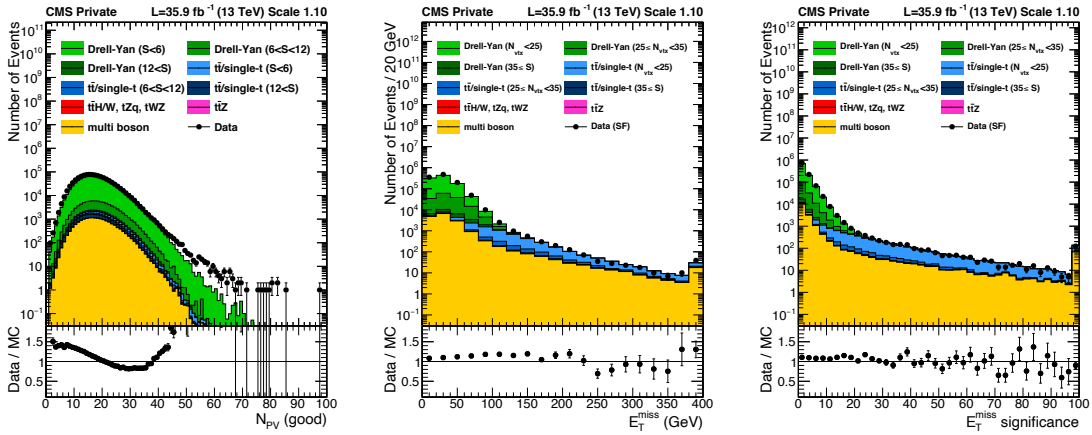

(a) N_{PV} distribution (DY split in bins of $\mathcal{S}$).

(b) $p_{\mathrm{T}}^{\mathrm{miss}}$ distribution (DY split in bins of vertex multiplicity).

(c) $\mathcal{S}$ distribution (DY split in bins of vertex multiplicity).

Figure 5.9: Distribution of vertex multiplicity, missing transverse energy and $p_{\mathrm{T}}^{\mathrm{miss}}$ significance where the DY contribution is split in bins of $\mathcal{S}$ (a) and N_{PV} (b and c).

$M_{\mathrm{T2}}(\ell\ell)$, a good description of the high vertex multiplicity tail should be achieved, however.

For the 2018 data set the nominal value 69.2mb of the minimum bias cross section is found to be suboptimal which can be seen in Fig. 5.10a. An increase of the cross section

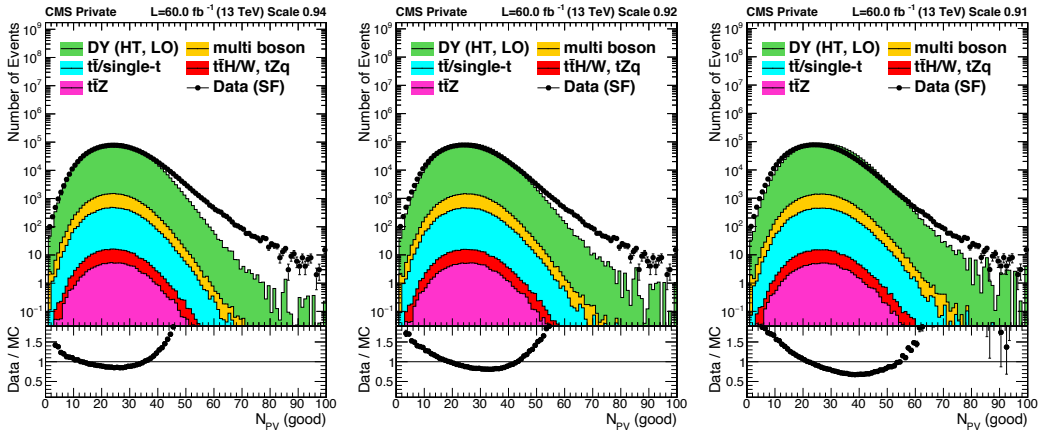

(a) 69.2mb (nominal)

(b) 72.6mb (+5%)

(c) 76.1mb (+10%)

Figure 5.10: Distribution of vertex multiplicity in 2018 data in a SF selection with a Z candidate and $N_{\mathrm{jets}} \geq 2$ and $N_{\text{b-jets}} = 0$ for three different values for the minimum bias cross section used in the PU reweighting.

by 10% to 76.1mb provides a much better description of the vertex multiplicity tail. Furthermore, Fig. 5.11 shows a comparison of the $p_{\mathrm{T}}^{\mathrm{miss}}$ distributions for the nominal and

the 10% increased minimum bias cross section. Comparing Fig. 5.10a and Fig. 5.10c,

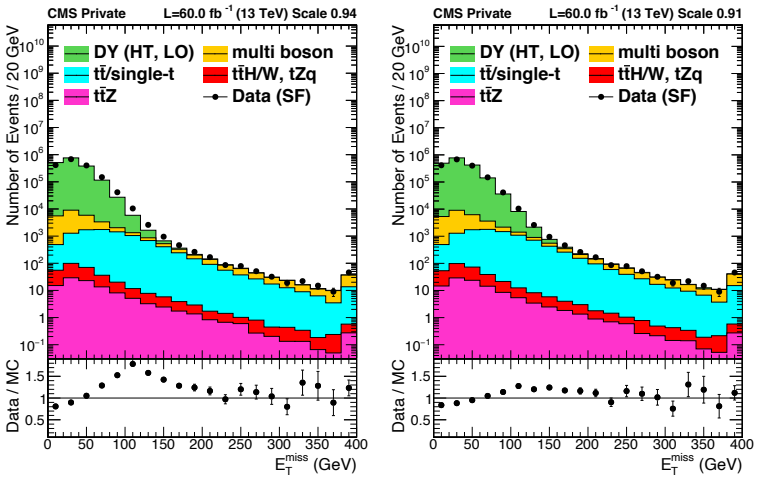

(a) 69.2mb (nominal) **(b)** 72.6mb (+10%)

Figure 5.11: Distribution of $p_{\mathrm{T}}^{\mathrm{miss}}$ in 2018 SF data in a selection with a Z candidate and $N_{\mathrm{jets}} \geq 2$ and $N_{\text{b-jets}} = 0$, and with nominal PU reweighting and with a minimum bias cross section of 76.1mb.

it becomes apparent that events with low vertex multiplicity are now more strongly mismodelling. However, these events are removed by the $\mathcal{S} > 12$ requirement that will be part of the preselection discussed in the next section.

It must be noted that one could also perform a PU reweighting such that simulated are scaled to agree with data in bins of vertex multiplicity. This choice would have introduced a dependence on the selection where the reweighting profile is measured.

5.2.2 Preselection

Object Selection

Leptons are selected according to a set of identification and isolation criteria which are summarised in Table 5.2 and will be discussed in the following. The leading (highest p_{T}) lepton in an event is required to have a transverse momentum of at least 30 GeV, while the trailing lepton must exceed 20 GeV. Both leptons must satisfy $-2.4 < \eta < 2.4$. If an event contains additional leptons with $p_{\mathrm{T}} > 15$ GeV and relative isolation below 0.4 it is vetoed, i.e. it is not considered in the analysis.

Table 5.2: Selection criteria for electrons and muons.

	dilepton selection		3rd lepton veto	
	electrons	muons	electrons	muons
p_{T}	$> 30(20)$ GeV	$> 30(20)$ GeV	> 15 GeV	> 15 GeV
$\lvert\eta\rvert$	< 2.4	< 2.4	< 2.4	< 2.4
isolation	miniIso < 0.2	miniIso < 0.2	relIso03 < 0.4	relIso03 < 0.4
$\lvert d_{xy}\rvert$	< 0.05	< 0.05	-	-
$\lvert d_z\rvert$	< 0.1	< 0.1	-	-
$\mathrm{SIP}_{3\mathrm{D}}$	< 4	< 4	-	-
lost hits	$= 0$	-	-	-
identification	cut-based criteria (e.g. expected missing inner hits ≤ 1)	global muon with additional muon-quality requirements	cut-based criteria (e.g. expected missing inner hits ≤ 2 or 3)	veto global muon with additional muon-quality requirements

For the electron identification cut-based criteria are used. For example, for a vetoed electron, the number of expected missing inner hits must be less than 2 for a supercluster in the barrel region ($|\eta| \leq 1.479$) and less than 3 in the endcap region ($|\eta| > 1.479$). Additionally, the longitudinal impact parameter $|d_z|$ with respect to the primary vertex is required to be less than 1 mm in the endcap region ($1.479 < |\eta| < 2.4$). Furthermore, the significance of the 3D impact parameter (IP) should satisfy $\mathrm{SIP}_{3\mathrm{D}} \equiv \left|\frac{\mathrm{IP}}{\sigma_{\mathrm{IP}}}\right| < 4$, where the IP is defined as the smallest distance of the lepton track to the primary vertex of the event and σ_{IP} is its associated uncertainty.

Muons are identified if the are reconstructed as a global muon and pass additional muon-quality requirements. Furthermore, the transverse impact parameter $|d_{xy}|$ and the longitudinal impact parameter $|d_z|$ with respect to the primary vertex are required to be less than 0.5 mm and 1 mm respectively. Just as for electrons, the $\mathrm{SIP}_{3\mathrm{D}}$ is required to be less than 4.

In terms of isolation of the leptons, the mini isolation variable is required to be smaller than 0.2 for both electrons and muons. Lepton identification and isolation efficiencies are measured per lepton leg in $Z/\gamma^* \to \ell\ell$ events using the tag-and-probe technique. The resulting data/MC scale factors, derived in bins of lepton p_{T} and $|\eta|$, have been applied on the simulated sample.

Due to tracking inefficiencies (loss of hits) there is a loss of lepton reconstruction

efficiency. This is taken into account by applying additional scale factors to each of the lepton legs in 2016 data. Uncertainties in the lepton reconstruction efficiencies are provided too, and are propagated to the final results.

Jets are constructed by clustering PF candidates using the Anti-k_t algorithm [49] with distance parameter $R = 0.4$. The effect of pileup is mitigated by the Charged Hadron Subtraction (CHS) technique which ignores charged particle candidates with a track closer along the z-axis to any vertex other than the primary vertex. Jets are calibrated in simulation and in data separately in order to account for imperfect detector response and deposits from pileup. Corrected jets with $p_{\mathrm{T}} > 30$ GeV and $|\eta| < 2.4$ are selected for the analysis if they also pass the jet identification criteria as recommended by the CMS POG. These include the requirement for neutral electromagnetic and hadron fractions of at most 99% in 2016 and 90% in 2017 and 2018. Non-zero charged hadron fraction and multiplicity are required, as well as a charged electromagnetic fraction less than 99% for 2016 and 2017 and less than 80% in 2018. Besides, a jet must consist of at least two PF candidates. Note that jet corrections are also propagated to $p_{\mathrm{T}}^{\mathrm{miss}}$.

A jet selected according to the just described criteria may still overlap with the selected leptons. This is due to the fact that a lepton may also be clustered into a jet. In order to prevent such cases, however, jets are removed from the set of selected jets in an event if they are found within a cone of $R = 0.4$ around any of the selected signal leptons.

Jets originating from the hadronisation of b-quarks are identified using the DeepCSV algorithm which is described in some detail in Section 4.3.1. For this analysis a jet is b-tagged if its discrimator value exceed the DeepCSV discriminator values according to the POG's medium working point, which are 0.6321 for 2016, 0.4941 for 2017 and 0.4184 for 2018 [64].

Event Selection

Events are required to have two leptons (ee, $\mu\mu$ or $e\mu$) with opposite charge in order to be considered for the analysis. The dilepton invariant mass m_{ll} must be 20 GeV at minimum. This invariant mass requirement successfully rejects events from QCD multijet processes. In order to avoid DY background contamination in same-flavour dilepton events (ee or $\mu\mu$), events with a $m_{\ell\ell}$ falling within a 15 GeV range from the Z-boson mass are rejected. The leading lepton is required to pass a transverse momentum threshold of $p_T > 30$ GeV to avoid a bias from the online selection.

At least two jets are required with at least one of them being b-tagged. Both jets are required to be separated from the $p_{\mathrm{T}}^{\mathrm{miss}}$ in the azimuthal plane. For the leading jet a separation of $\cos(\Delta\phi(p_{\mathrm{T}}^{\mathrm{miss}}, \mathrm{j}_1)) < 0.8$ is required and $\cos(\Delta\phi(p_{\mathrm{T}}^{\mathrm{miss}}, \mathrm{j}_2)) < \cos(0.25)$ for the second leading jet, where $0.8 \approx \cos(0.64)$ and $\cos(0.25) \approx 0.97$. The relatively small angular separation between $p_{\mathrm{T}}^{\mathrm{miss}}$ and the sub-leading jet is aimed to protect against drastic jet mismeasurements. The reasoning is that in some cases, when the true leading jet is reconstructed having sufficiently less energy such that it ends up as the subleading jet, $p_{\mathrm{T}}^{\mathrm{miss}}$ is typically aligned with the sub-leading jet to within half the

jet clustering distance. These selections have a relatively small impact, though.

In the 2017 data set, events with a jet with transverse momentum of at least 30 GeV and $2.6 < |\eta| < 3$ are vetoed because of some miscalibrated ECAL endcap (EE) channels. This reduces the acceptance in the 2017 data taking period by about 10%, i.e. the expected yield after all preselection cuts for `T2tt` with $m_{\tilde{t}} = 600$ GeV, $m_{\tilde{\chi}_1^0} = 0$ GeV drops from 47.5 to 43.4. For comparison the HEM region veto in the 2018 data set has a 20% effect, i.e. the `T2tt` yield after all preselection cuts for $m_{\tilde{t}} = 600$ GeV, $m_{\tilde{\chi}_1^0} = 0$ GeV drops from 69.9 to 57.4.

Backgrounds without genuine $p_{\mathrm{T}}^{\mathrm{miss}}$ are removed with a suitable threshold on $p_{\mathrm{T}}^{\mathrm{miss}}$ significance, denoted by $\mathcal{S}$. The distribution of $\mathcal{S}$ is shown in Fig. 5.12 in a control region with $N_{\mathrm{jets}} \geq 2$ and $N_{\text{b-jets}} = 0$. The hashed uncertainty band is from experimental (ob-

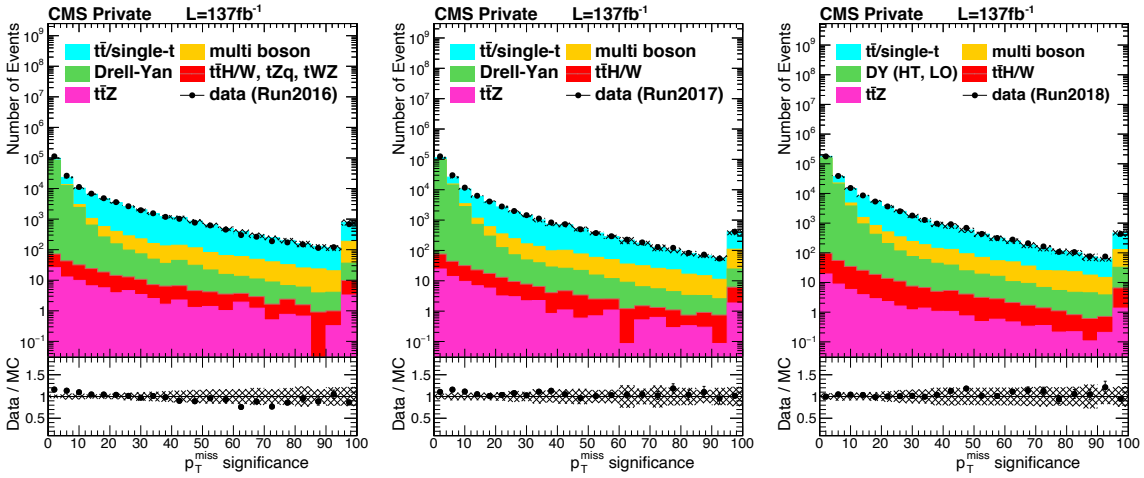

(a) 2016 **(b)** 2017 **(c)** 2018

Figure 5.12: Distribution of $\mathcal{S}$ in the $N_{\mathrm{jets}} \geq 2$ and $N_{\text{b-jets}} = 0$ control region.

ject level) systematic uncertainties. In the tail region (i.e. high $\mathcal{S}$) of the distribution where $t\bar{t}$ is dominant, the agreement is within one standard deviation. For events from a DY process, which have no genuine $p_{\mathrm{T}}^{\mathrm{miss}}$, the modelling of $p_{\mathrm{T}}^{\mathrm{miss}}$ resolution is difficult. The plots in Fig. 5.12 already indicate that specific sidebands, where DY is important, will have scale factors for DY that may deviate from unity. Based on sensitivity studies in simulation that are described in Sec. 5.3 a cut of $\mathcal{S} > 12$ is chosen. A complete summary of the event selection is displayed in Table 5.3.

A so-called cut flow table is shown in Table 5.4. It displays the background yields for the subsequent application of the selection cuts defining the search region, as well as the corresponding yields for a signal sample with the parameters $m_{\tilde{t}} = 600$ GeV and $m_{\tilde{\chi}_1^0} = 0$ GeV.

Table 5.3: Summary of the event selection.

N_{leptons}	=	2, opposite charge
p_T(leading lepton)	>	30 GeV
p_T(sub-leading lepton)	>	20 GeV
N_{jets}	$\geq$	2
$N_{\text{b-jets}}$	$\geq$	1
$m_{\ell\ell}$	>	20 GeV
$\lvert m_{\ell\ell} - m_Z \rvert$	>	15 GeV
$\mathcal{S}$	>	12
$\lvert\Delta\phi(p_{\text{T}}^{\text{miss}}, \text{leading jet})\rvert$	>	0.64
$\lvert\Delta\phi(p_{\text{T}}^{\text{miss}}, \text{sub-leading jet})\rvert$	>	0.25

Table 5.4: Cut flow table for background yields combining all three years.

	$t\bar{t}+Z$	$t\bar{t}+X$	Multiboson	DY	$t/t\bar{t}$	T2tt(600, 0)
no cuts	7151.9	13673.4	544761.6	168591225.9	2757678.6	758.3
$n_{\text{lepton}} = 2$	4248.5	7644.7	367426.5	157311344.0	1356448.1	374.1
opposite charge	3920.2	6303.1	358668.6	156927208.4	1341876.2	368.2
loose lepton veto	3169.3	5336.1	340069.9	155167234.8	1258279.3	324.9
$m_{\ell\ell} > 20$ GeV	3021.5	5270.4	334832.3	154587865.2	1231437.0	321.0
$\lvert m_{\ell\ell} - m_Z \rvert > 15$ GeV (SF)	941.1	2304.7	105211.1	10215930.5	960502.3	272.2
$n_{\text{jet}} \geq 2$	862.1	2106.7	16916.5	639331.7	650828.5	225.3
$n_{b-\text{tag}} \geq 1$	697.2	1691.6	1707.4	62166.5	544314.9	191.5
$p_{\text{T}}^{\text{miss}}$ significance	240.6	621.1	253.6	753.0	170847.3	168.2
$\phi(p_{\text{T}}^{\text{miss}}$, jets) veto	211.8	555.0	228.6	509.7	154867.6	155.0
bad EE jet veto	203.4	536.7	222.5	476.1	150678.8	150.8
$M_{T2}(ll) > 140$ GeV	9.3	5.7	3.9	4.4	16.3	54.2

5.3 Signal and control regions

Signal regions are constructed using the $M_{\text{T2}}(\ell\ell)$, $M_{\text{T2}}(b\ell b\ell)$ and $\mathcal{S}$ variables on top of the preselection discussed in Section 5.2.2. In order to optimise the sensitivity of the analysis while ensuring reasonable statistical uncertainties in simulated samples, $M_{\text{T2}}(\ell\ell) \geq 100$ GeV is applied as the first requirement. This particular threshold is motivated by the shoulder in the $M_{\text{T2}}(\ell\ell)$ distribution below m_W, as shown in Fig. 5.2, with a suitable margin that approximately corresponds to the $p_{\text{T}}^{\text{miss}}$ resolution. Thereby, it is ensured that the SRs have a relatively small contamination from dileptonic top quark decays. Events with $M_{\text{T2}}(\ell\ell) < 100$ GeV will serve as a control region for the $t\bar{t}$ background with an extra $\lvert m_{\ell\ell} - m_Z \rvert \geq 15$ GeV veto in the same-flavour channel.

Next, the $M_{\text{T2}}(\ell\ell) > 100$ GeV region is sliced into bins with respect to the other two variables using a fine binning of 50 GeV which results in a large number of signal regions. In order to determine a suitably chosen SR binning the following procedure was

used. It aims to find an attractive compromise between the feasibility of the background estimation on the one hand, and the sensitivity of the analysis on the other. First, the signal and background yields have been estimated purely from simulation for those regions. Then a 95% confidence level exclusion limit as a function of the SUSY mass parameter is obtained. It includes all uncertainties except the ones related to the data driven background estimation procedures that will be discussed in Section 5.5. In order to avoid a bias towards finer binning, SRs with a vanishing background estimation are excluded. Subsequently, to get rid of empty regions, the empty SR bins were combined with others starting at the highest bins in each of the variables. While collapsing the SRs, small losses of the sensitivity where monitored by re-evaluating the simulation-based contour in the limit. The outcome of this process shows that a 100 GeV binning in $M_{\mathrm{T2}}\,(b\ell b\ell)$ is sufficient. In terms of $\mathcal{S}$, two bins with a threshold of 50 GeV are used. Furthermore it was found that $M_{\mathrm{T2}}\,(\ell\ell)$ should be split into three different bins, with the first threshold at around 140 GeV and the second one at 240 GeV. The 13 resulting signal regions with respect to $M_{\mathrm{T2}}\,(\ell\ell)$, $M_{\mathrm{T2}}\,(b\ell b\ell)$ and $\mathcal{S}$ are listed in Table 5.5. The same flavour and opposite flavour search regions have different

Table 5.5: Definition of the signal regions on top of the preselection in Table 5.3.

$M_{\mathrm{T2}}\,(b\ell b\ell)$ (GeV)	$\mathcal{S}$	$100 \leq M_{\mathrm{T2}}\,(\ell\ell) < 140$ GeV	$140 \leq M_{\mathrm{T2}}\,(\ell\ell) < 240$ GeV	$M_{\mathrm{T2}}\,(\ell\ell) \geq 240$ GeV
$0-100$	$12-50$	SR0	SR6	SR12
	≥ 50	SR1	SR7	
$100-200$	$12-50$	SR2	SR8	
	≥ 50	SR3	SR9	
≥ 200	$12-50$	SR4	SR10	
	≥ 50	SR5	SR11	

background compositions due to the fact that backgrounds where the two leptons stem from a Z boson will not contribute to the opposite flavour channel. Therefore a split of the SRs into same-flavour (SF) and opposite-flavour (OF) regions is implemented, which yields 26 SRs in total. A further splitting of the SF channels into individual $\mu\mu$ and ee channels has turned out not to be beneficial, however.

As previously mentioned, the $M_{\mathrm{T2}}\,(\ell\ell) < 100$ GeV region will serve as a control region for the $t\bar{t}$ background, with an extra $|m_{\ell\ell} - m_Z| \geq 15$ GeV veto in the SF channel. In addition, two sets of control regions are added in order to constrain the DY/diboson and $t\bar{t} + Z$ backgrounds respectively. Five $t\bar{t} + Z$ control regions are added by moving to a 3ℓ sideband and requiring different combinations of jet and b-tagged jet multiplicities. Furthermore, DY/diboson contributions are measured in 13 control regions orthogonal to the SRs. Those CRs are obtained by inverting the b-jet and the Z-window ($|m_{\ell\ell} - m_Z| \geq 15$ GeV) requirement in each signal region. Note that for the DY/diboson control regions only same-flavour channels are used. The use of these control regions, which are summarised in Table 5.3, is discussed in some detail in Section 5.5.

The combination of signal and control regions are collectively called mainband regions.

Table 5.6: Definition of the control regions with respect to the preselection in Table 5.3.

name	extra requirement	process
TTCRSF	$M_{\mathrm{T2}}(\ell\ell) < 100$ GeV, SF leptons, $\lvert m(\ell\ell) - m_Z \rvert > 15$	$t\bar{t}$
TTCROF	$M_{\mathrm{T2}}(\ell\ell) < 100$ GeV, OF leptons	$t\bar{t}$
TTZ2j2b	3$^{\mathrm{rd}}$ lepton $p_{\mathrm{T}} > 20$, Z candidate, $\mathcal{S} \geq 0$, $N_{\mathrm{jets}} = 2$, $N_{\text{b-jets}} \geq 2$	$t\bar{t} + Z$
TTZ3j1b	3$^{\mathrm{rd}}$ lepton $p_{\mathrm{T}} > 20$, Z candidate, $\mathcal{S} \geq 0$, $N_{\mathrm{jets}} = 3$, $N_{\text{b-jets}} = 1$	$t\bar{t} + Z$
TTZ3j2b	3$^{\mathrm{rd}}$ lepton $p_{\mathrm{T}} > 20$, Z candidate, $\mathcal{S} \geq 0$, $N_{\mathrm{jets}} = 3$, $N_{\text{b-jets}} \geq 2$	$t\bar{t} + Z$
TTZ4j1b	3$^{\mathrm{rd}}$ lepton $p_{\mathrm{T}} > 20$, Z candidate, $\mathcal{S} \geq 0$, $N_{\mathrm{jets}} \geq 4$, $N_{\text{b-jets}} = 1$	$t\bar{t} + Z$
TTZ4j2b	3$^{\mathrm{rd}}$ lepton $p_{\mathrm{T}} > 20$, Z candidate, $\mathcal{S} \geq 0$, $N_{\mathrm{jets}} \geq 4$, $N_{\text{b-jets}} \geq 2$	$t\bar{t} + Z$
CR0-CR12	same as SR0-SR12 in Table 5.5, but $\lvert m(\ell\ell) - m_Z \rvert \leq 15$ and $N_{\text{b-jets}} = 0$	DY, MB

Sideband regions, on the other hand, distinguish themselves in terms of inverted jet and b-tagged jet multiplicity requirements. They are used to cross-check the background modelling in Appendix A.

5.4 Systematic uncertainties

The data-driven manner of quantifying experimental characteristics based on reconstructed objects introduces systematic uncertainties which are considered in simulation. Recalling Eq. (5.1), the number of predicted events is obtained from the number of simulated ones by a reweighting factor w

$$N_{\mathrm{pred}} = w \cdot N_{\mathrm{sim}} \ .$$

Systematic uncertainties of the predicted backgrounds in the SRs are measured in simulation by independently varying existing event weights up and down by one standard deviation, i.e. $1\,\sigma$, or by introducing new ones. A specific uncertainty for one SR can then be expressed as

$$\delta_{\mathrm{syst}} = \frac{N'_{\mathrm{pred}}}{N_{\mathrm{pred}}} - 1 \ ,$$

where N' reflects the predicted background yield using the varied weight, and N using the central value of the weight (assuming the simulated yield remains unchanged). As will be described in detail in Section 5.5, the normalisations of the main backgrounds in the signal regions are obtained and studied in the control regions. It turns out that the predicted values of the main backgrounds in the SRs are only sensitive to the differences of uncertainties between SR and CR, not their absolute values. As a result, any effect that changes the background yields in corresponding signal and control regions by the same factor will not have any affect on the final results. A summary of the experimental systematic uncertainties that are relevant for the backgrounds in this analysis is given in Table 5.8. Those background uncertainties as well as ones for

Table 5.7: Overview of systematic uncertainties.

systematic	size
Pileup	$\leq 6.5\%$
Jet energy resolution	$\leq 40.8\%$
Jet energy corrections	$\leq 14.1\%$
Top quark p_{T} reweighting	$\leq 3.0\%$
Unclustered energy	$\leq 32.1\%$
b-tagging SF (b quark)	$\leq 1.1\%$
b-tagging SF (light quark)	$\leq 1.8\%$
Lepton SF	$\leq 1.8\%$
Trigger	$\leq 2.5\%$

signals will be presented in the following.

For $t\bar{t}$+jets and $t\bar{t}+Z$ backgrounds the renormalisation and factorisation scale is varied while keeping the overall normalisation constant. The assigned uncertainty is based on the envelope of the variations and is uncorrelated between the different background processes. The assumption of certain parton distribution functions (PDFs) can have an effect on the simulated $M_{\mathrm{T2}}(\ell\ell)$ shape. Therefore, the change of acceptance in the signal regions is measured and the envelope of the acceptances assigned as a correlated uncertainty.

Pileup

A variation of $\pm 5\%$ on the minimum bias cross section is used to estimate the uncertainties due to the pileup modelling. As explained in Section 5.2.1, the pileup distribution differs between simulation and data. This has motivated the introduction of a pileup reweighting procedure based on a total inelastic collision cross section of 69.2 mb in order to match the simulated PU activity to data. For the 2018 data set the value is increased by 10% and a total inelastic cross section of 76.1 mb is used. The resulting uncertainty on the background prediction in the SRs is well below 10%.

Jet energy scale and resolution

The jet energy scale (JES) [65] is varied within 1σ uncertainty as a function of jet p_{T} and η. The arising changes are propagated to all observables, including $p_{\mathrm{T}}^{\mathrm{miss}}$ and $\mathcal{S}$.

The jet energy resolution (JER) scale factors are much larger in the 2017 and, especially, the 2018 data set than in the 2016 one. Meanwhile, the indirect effect on the JER SF complicates the estimation of the DY background in the CR in 2017 and 2018, as will be described later. Because of the feeble control of this experimental effect, the full JER SF is taken as an uncertainty, not just its uncertainty. Therefore, the JER uncertainty can take on values up to 40.8% in the SRs. These large JER SFs for the

2018 data set will be subject to future refinements.

Unclustered energy

Moreover, the $p_{\mathrm{T}}^{\mathrm{miss}}$ and $\mathcal{S}$ observables are subject to uncertainties from the unclustered energy which is varied within uncertainties.

Jet energy corrections

Variations of jet energy corrections within 1σ are applied and propagated to the dependent variables. They impact the jet energy spectrum as well as $p_{\mathrm{T}}^{\mathrm{miss}}$. The resulting uncertainty reaches values of up to 14.1% in certain SRs.

b-tag scale factor

The simulated efficiencies for the identification of b-quark jets and for the misidentification of c-quark, light-quark or gluon jets need to be corrected for with scale factors and their respective uncertainties to match the ones in data. The SFs are evaluated in a data-driven manner using the simulated b-tagging efficiency. The used method does not consider a migration of events from one b-tag multiplicity bin to the other, in other words simulated events with n b-tagged jets will continue to have n b-tagged jets after the reweighting. The b-tagging uncertainty accounts for less than 1% in most regions.

Lepton scale factors

Systematic uncertainties for the efficiency of lepton reconstruction and identification are handled in the same way as for b-tagging. The lepton identification efficiencies are considered for electrons and muons separately. The uncertainties are derived from factorised two-dimensional measurements in p_{T} and η.

Trigger efficiency

The applied trigger efficiencies are described in Section 5.1 and the corresponding bin-by-bin uncertainties are applied as systematics in a correlated way across the three data sets. When a background or signal yield is taken from a simulated sample, the statistical uncertainties are taken into account. These uncertainties apply to both the background prediction and the signal yield. For the backgrounds the systematic uncertainties are below 2.5%.

Reweighting of the top quark p_{T}

The p_{T} spectrum of top quarks is found to be softer in data than predicted by various simulations using LO and NLO event generators [66, 67]. It turns out that perturbative calculations at NNLO precision provide a good description of the top quark p_{T} spectrum [68]. In order to account for the difference between the LO $t\bar{t}$+jets event samples used in the analysis, a weight is applied. The uncertainty is then assessed from the background prediction between applying and not applying the weight. This results in uncertainties below 3%. Note that top quark p_{T} reweighting uncertainties are not used in the limit setting.

Signal uncertainties

For the signal samples an additional uncertainty on the initial-state radiation (ISR) is applied. ISR is determined based on the number of jets which are not matched to simulated particles descending from top quarks, W, Z, Higgs bosons or SUSY particles. An event is reweighted based on the distribution of this observables, while the total change in the cross section of the respective mass point is accounted for.

Furthermore, the factorisation and renormalisation scale are each changed by a factor of 0.5 and 2 respectively. The envelope of the variations of the predicted signal yield is assigned as a systematic uncertainty. Note that anti-correlated variations are not considered.

Finally, uncertainties in the signal cross section are also taken into account.

5.5 Background estimation

The aim in this section is to study the shape and normalisation of the main backgrounds of the analysis in dedicated control regions. The dominating backgrounds in the signal and control regions, namely $t\bar{t}$, DY, diboson and $t\bar{t} + Z$ backgrounds are shown in Fig. 5.13. The CRs for the different background components are defined in Table 5.6. They are based on a sideband selections with respect to the the SR preselection, summarised in Table 5.3. Table 5.4 shows the effect of the different cuts on the backgrounds and the signal in the signal region. The signal contamination in the CRs is negligible except in the $t\bar{t}$ region when the top squark mass is close to the top mass. In this case the contamination can reach values up to 15%. In order to properly take this into account the signal is included in the maximum likelihood fits discussed later on. Additional checks on the modelling of the main backgrounds is displayed in Appendix A in background enriched sideband regions.

The stategy pursued here will be to perform a maximum likelihood fit for the control and signal regions simultaneously in order to then be able to set limits on the production cross section of top squarks for three different models. However, before that, a fit is performed on just the control regions. Each background component is assigned an

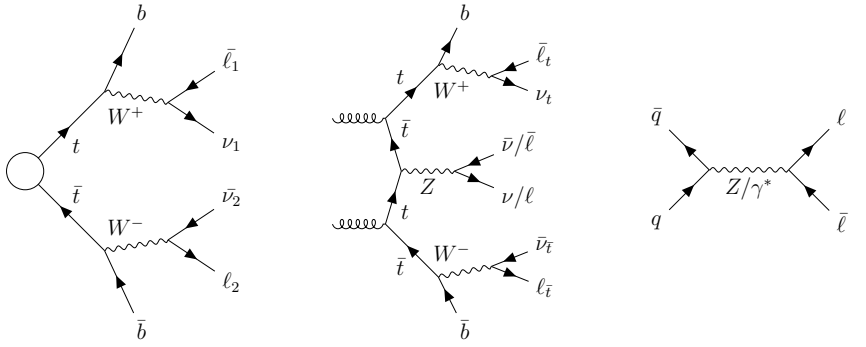

(a) $t\bar{t}$ background

(b) $t\bar{t} + Z$ background

(c) DY background

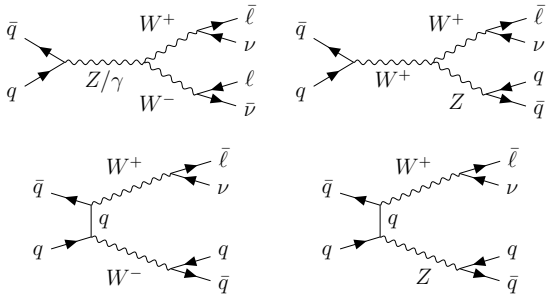

(d) Diboson background

Figure 5.13: Main backgrounds in this analysis.

unconstrained rate parameter. Performing a maximum likelihood fit on the CRs then results in (post-fit) normalisation factors (SFs) of the backgrounds and their covariance matrix which can be extracted for further use. Overall, the background estimation strategy is very similar to the one in the preceding analysis [53]. In the following, the control regions and the input uncertainties that are assigned to the various background components are discussed.

5.5.1 $t\bar{t}$ background

The $t\bar{t}$ contribution is normalised using the $M_{\mathrm{T2}}(\ell\ell) < 100$ GeV CR, split into same flavour (SF) and opposite flavour (OF) channels as defined in Tab. 5.6. In order to be able to estimate the relevant uncertainties, some checks on $t\bar{t}$ events in the tails of the $M_{\mathrm{T2}}(\ell\ell)$ distribution are performed. The $t\bar{t}$ background contributions are categorised into four classes, for which separate uncertainties will be assessed. A non-gaussian jet mismeasurement[2] is defined by the presence of a single jet in the event with a transverse momentum mismeasurement of more than 40 GeV. Gaussian jet mismeasurement, on the other hand, is characterised by a total jet mismeasurement of a least 40 GeV, meaning the mismeasurements of all individual jets are summed over. The remaining

[2]In simulation the mismeasurement can simply be determined by taking the difference of the generated and the corresponding reconstructed objects.

two categories are cases with non-prompt or fake leptons which are identified by the absence of a match in simulation for one or both of the leptons respectively. Figure 5.14 displays the $M_{\mathrm{T2}}(\ell\ell)$ distributions in term of these categories. The uncertainty in the gaussian component of the $t\bar{t}$ shape is assumed to be covered by the JER uncertainty.

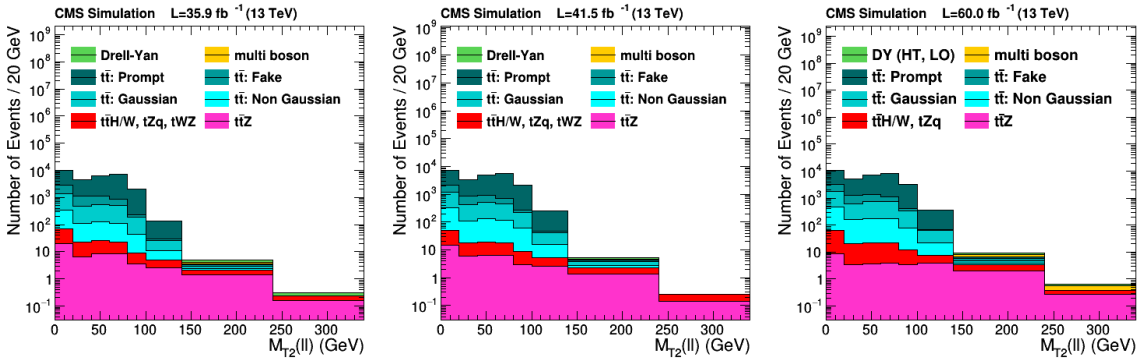

(a) 2016 **(b)** 2017 **(c)** 2018

Figure 5.14: $M_{\mathrm{T2}}(\ell\ell)$ distributions of $t\bar{t}$ background in $\mu\mu$ channel with $N_{\text{jets}} \geq 2$, $N_{\text{b-jets}} \geq 1$ for the respective years.

$p_{\mathrm{T}}^{\mathrm{miss}}$ mismeasurements

The rate of large $p_{\mathrm{T}}^{\mathrm{miss}}$ mismeasurements is checked using the $N_{\text{jets}} \geq 2$, $N_{\text{b-jets}} = 0$ control region in an attempt to limit a potential mismodelling of such mismeasurement effects. Drell-Yan events are useful for this task, since they have no genuine $p_{\mathrm{T}}^{\mathrm{miss}}$. Any missing transverse energy originates from mismeasurements. Therefore, DY events are selected by requiring a lepton pair consistent with the Z boson mass within 15 GeV, i.e. $|m_{\ell\ell} - m_Z| < 15$ GeV. First, the tail of the $p_{\mathrm{T}}^{\mathrm{miss}}$ distribution is checked. However, it is obstructed by the presence of the $t\bar{t}$ background, which dominates for sufficiently high $p_{\mathrm{T}}^{\mathrm{miss}}$ thresholds because of genuine $p_{\mathrm{T}}^{\mathrm{miss}}$ from neutrinos. To circumvent this limitation, the $M_{\mathrm{T2}}(\ell\ell)$ distribution is studied instead.

The $M_{\mathrm{T2}}(\ell\ell)$ plots are shown in Fig. 5.15 for the three data taking periods and are scaled by luminosity. The $t\bar{t}$ is background is beneficially suppressed in the $M_{\mathrm{T2}}(\ell\ell)$ tail. Furthermore, the DY contribution is split in coarse bins of $p_{\mathrm{T}}^{\mathrm{miss}}$ in steps of 40 GeV. DY events with large values of (mismeasured) $p_{\mathrm{T}}^{\mathrm{miss}}$ happen to populate the $M_{\mathrm{T2}}(\ell\ell)$ tail. In fact, $p_{\mathrm{T}}^{\mathrm{miss}}$ and $M_{\mathrm{T2}}(\ell\ell)$ are strongly correlated for the DY background. There is also a tiny $Z \to \tau\tau$ contribution with genuine $p_{\mathrm{T}}^{\mathrm{miss}}$ which can be ignored because it populates low values of $M_{\mathrm{T2}}(\ell\ell)$. There is no sign of unaccounted sources of non-gaussian jet mismeasurements that are originating from $p_{\mathrm{T}}^{\mathrm{miss}}$ mismeasurements. They would otherwise appear in the tail of the $M_{\mathrm{T2}}(\ell\ell)$ distribution. Based on the agreement of data and simulation in Fig. 5.15, an uncertainty of 30% on the non-gaussian component for $t\bar{t}$ is applied. In Section 5.5.2, a residual era dependent trend that is covered by the uncertainty in the JER scale factor will be explained.

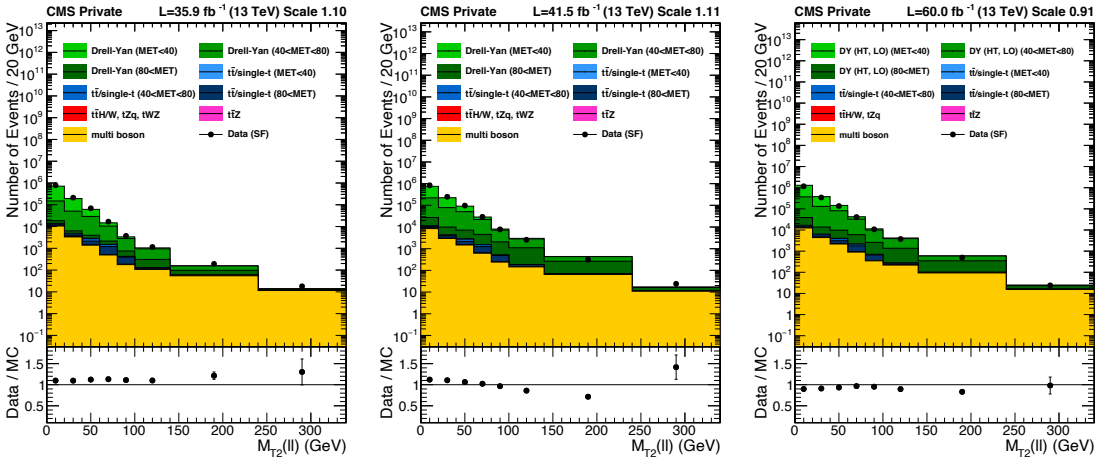

(a) 2016 **(b)** 2017 **(c)** 2018

Figure 5.15: Distribution of $M_{\mathrm{T2}}(\ell\ell)$ in the same flavour channel of the $N_{\text{jets}} \geq 2$, $N_{\text{b-jets}} = 0$ selection without the $\mathcal{S} > 12$ requirement for the three data taking periods.

Fake lepton shape in 2ℓ events

The simulated $M_{\mathrm{T2}}(\ell\ell)$ shape for fake and non-prompt leptons is checked in the following way. Two independent studies based on two and three lepton control regions are considered in the next two sections. First, lepton misidentification is mimicked by selecting three lepton events where the third lepton is non-isolated (i.e. no isolation criterion applied) and either fulfills $p_{\mathrm{T}} > 7$ GeV or $p_{\mathrm{T}} > 5$ GeV for electrons and muons, respectively. All other selections summarised in Table 5.3 are applied. In order to imitate the loss of a lepton, $M_{\mathrm{T2}}(\ell\ell)$ is recomputed by combining either the leading or the sub-leading lepton with the extra trailing lepton selected in this way. Figure 5.16a diagrammatically depicts this case. Changes in flavour channel associated with the

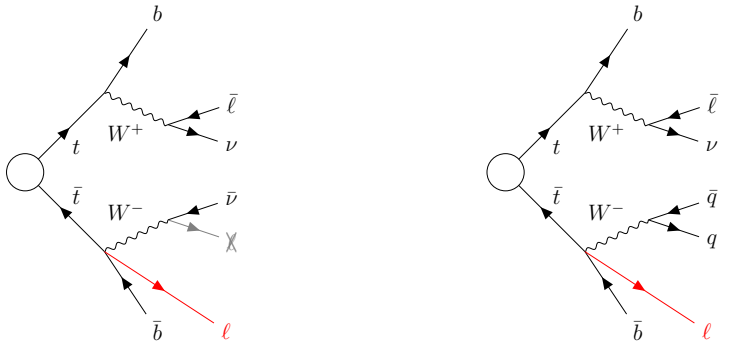

(a) $t\bar{t}$ background with lost lepton **(b)** semi-leptonic $t\bar{t}$ background

Figure 5.16: Fake and non-prompt $t\bar{t}$ backgrounds.

lepton replacement are monitored. This swapping procedure is applied to lepton mo-

menta only. The $p_{\mathrm{T}}^{\mathrm{miss}}$ is not changed because of the very high detection efficiency and compensating nature of the nearly hermetic CMS detector. The procedure can be applied to both data and simulation and the resulting $M_{\mathrm{T2}}(\ell\ell)$ distributions are shown in Fig. 5.17 and exhibit excellent agreement between data and simulation.

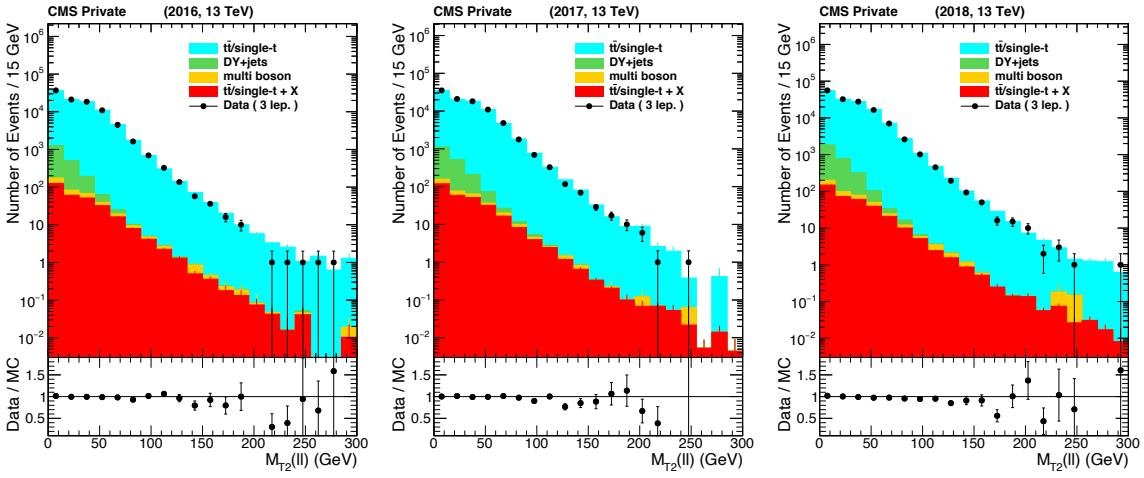

(a) 2016 **(b)** 2017 **(c)** 2018

Figure 5.17: $M_{\mathrm{T2}}(\ell\ell)$ distributions in the three lepton control region with all lepton channels combined for the years 2016, 2017 and 2018. Changes of flavour and p_{T} due to the lepton swapping are taken into account. MC yields are normalised to data using the yields at $M_{\mathrm{T2}}(\ell\ell) < 100$ GeV.

It remains to be shown that the swapping procedure really mimics the lost lepton contribution. This is done analogous to the 2016 analysis [53] in Figure 5.18 where the two-lepton simulation is overlayed with an inverted isolation requirement $I_{\mathrm{mini}} > 0.2$ on the trailing lepton (red line) with the three-lepton prediction from the swapping procedure (blue area). The distributions are normalised for $M_{\mathrm{T2}}(\ell\ell) > 100$ GeV and the almost perfect agreement confirms that the swapping procedure mimics the loss of a lepton very well for $M_{\mathrm{T2}}(\ell\ell) > 80$ GeV. It should be noted that the swapping procedure is not strongly dependent on the p_{T} threshold in the selection of the extra leptons. As long as the loose selection guarantees that the third (extra) leptons are dominated by fake leptons from jets or from non-prompt decays in b-jets, the reconstructed value of $M_{\mathrm{T2}}(\ell\ell)$ after swapping is governed by the modelling of the distribution of the relative angles between leptons and jets. The transverse momentum of fake and non-prompt leptons is typically too small to have a dominant effect on the $M_{\mathrm{T2}}(\ell\ell)$ reconstruction. This procedure is only expected to describe the tail of the distribution. The discrepancy at low values comes from a large contribution of 2ℓ events where the lepton with inverted isolation is nevertheless prompt. In conclusion, there are no signs of a discrepancy in the $M_{\mathrm{T2}}(\ell\ell)$ shape for events with a lost lepton from this study.

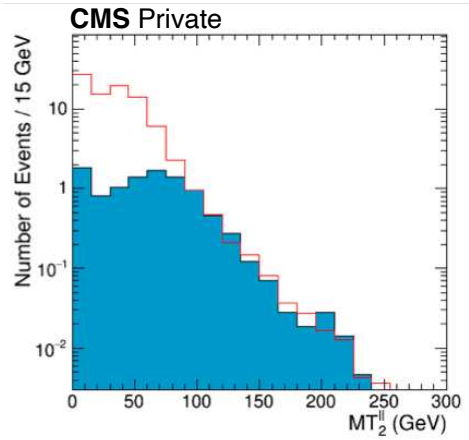

Figure 5.18: Comparison of the three lepton simulation (blue area) and the two-lepton simulation with inverted isolation requirements on one of the leptons (red line), normalised at $M_{\mathrm{T2}}(\ell\ell) > 100$ GeV. The plot is reproduced from the 2016 analysis [53].

Fake lepton shape in 1ℓ events

In this study, 1ℓ events with an extra non-isolated lepton are selected to further constrain the $M_{\mathrm{T2}}(\ell\ell)$ shape. For a semi-leptonic $t\bar{t}$ selection as indicated in Fig. 5.16b, one lepton satisfying the analysis requirements and also $N_{\text{jets}} \geq 4$ and $N_{\text{b-jets}} \geq 1$ is required. For the non-isolated lepton, the isolation criterion is inverted to mini isolation > 0.2. Figure 5.19 shows the distribution of m_T computed with the non-isolated lepton and the distribution of $M_{\mathrm{T2}}(\ell\ell)$ computed with the lepton and the non-isolated lepton. Since there is no $p_{\mathrm{T}}^{\mathrm{miss}}$ from an neutrino directly corresponding to the non-isolated lepton, there is no chance for that event to end up in the $M_{\mathrm{T2}}(\ell\ell)$ tail. Hence, $M_{\mathrm{T2}}(\ell\ell)$ efficiently rejects semi-leptonic $t\bar{t}$ in the signal regions. A very good agreement between data and simulation is observed.

There are no visible signs that the $M_{\mathrm{T2}}(\ell\ell)$ shape of the fake component of $t\bar{t}$ is significantly mismodelled. It is, however, a small contribution that is constrained only indirectly by the CR studies presented here. An uncertainty of 30% is assessed on this contribution.

Finally, the rate of loose leptons can be checked when the loose lepton veto is lifted by checking the distribution of the lepton mini isolation for electrons, muons for all three years. These distributions are shown in Fig. 5.20 and exhibit very good agreement between data and simulation, both in in the shape and the total rate.

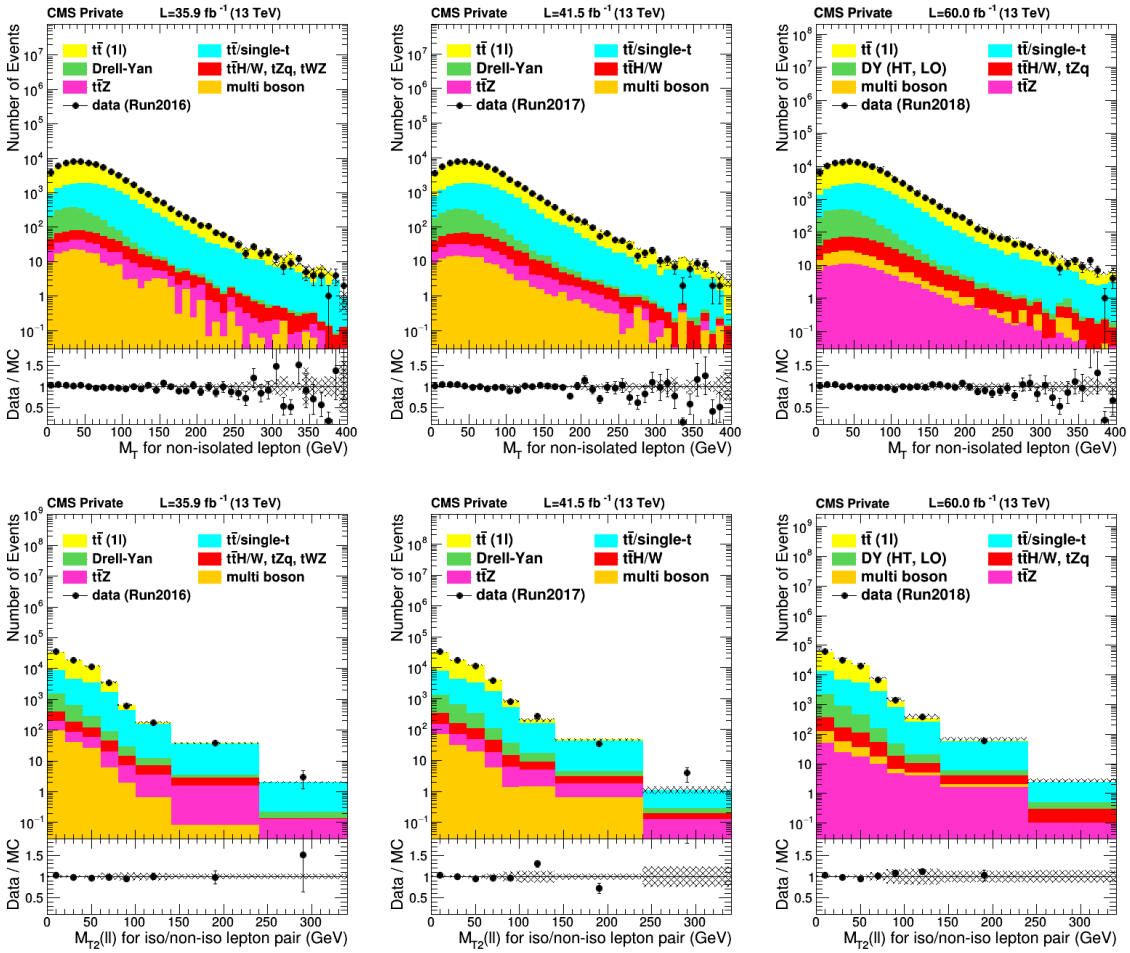

Figure 5.19: Transverse mass for non-isolated leptons (top); $M_{T2}(\ell\ell)$ for lepton pair consisting of one isolated and one non-isolated lepton (bottom) for 2016, 2017 and 2018 (from left to right).

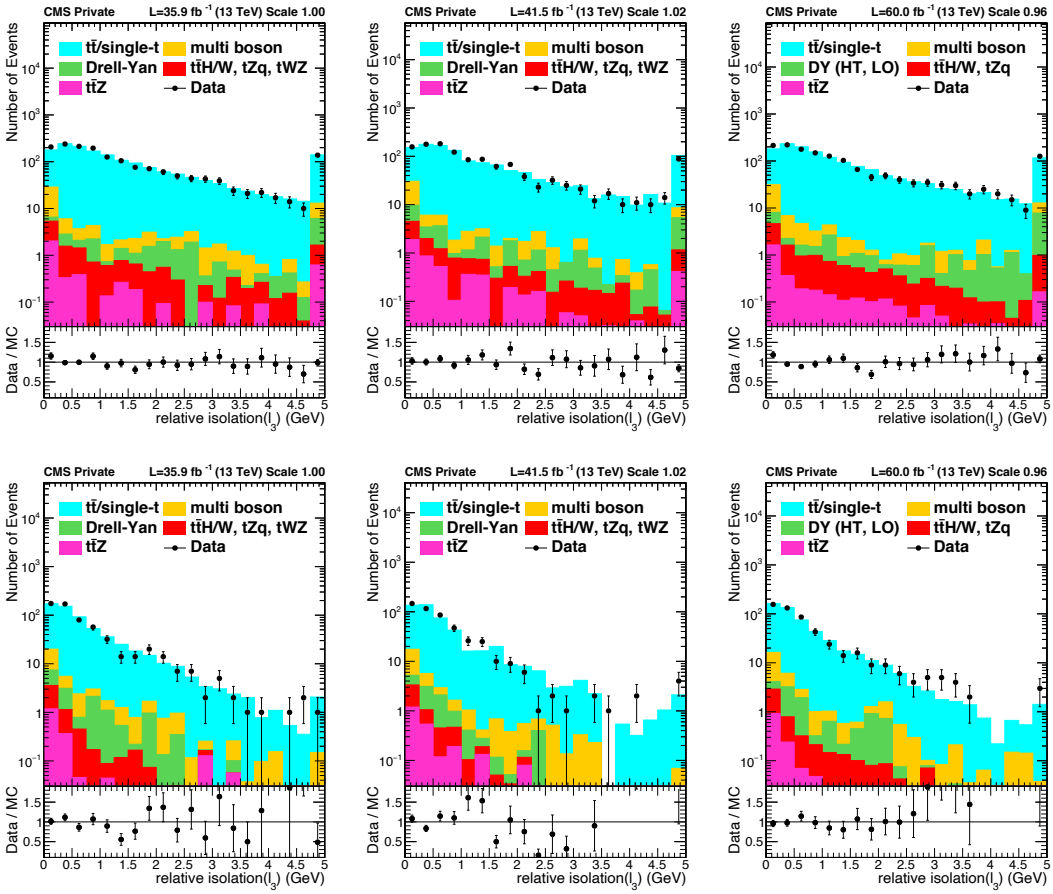

Figure 5.20: Isolation of the loose lepton when the veto on loose leptons is lifted for muons (top) and electrons (bottom) for 2016 (left), 2017 (middle), and 2018 (right).

5.5.2 Drell-Yan and Multiboson background

The background contribution from Drell-Yan events is greatly reduced by the event selection, as discussed in Section 5.2.2, where several cuts on $p_{\mathrm{T}}^{\mathrm{miss}}$-related variables are applied. In this section, these cuts and the properties of the DY background are discussed in more detail using control regions defined by a 0 b-jet and on Z mass requirement, the latter being defined by $|m_{\ell\ell} - m_Z| < 15$ GeV.

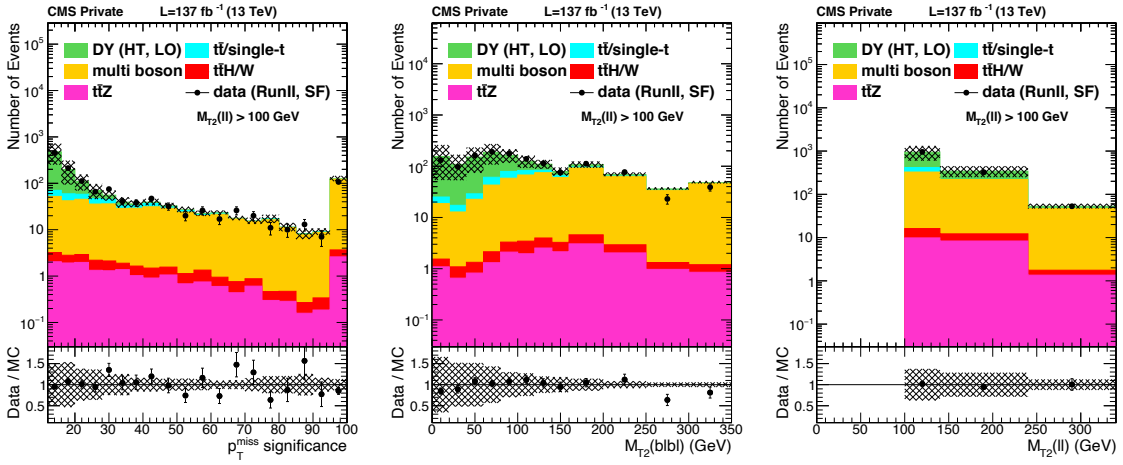

(a) $\mathcal{S}$ **(b)** $M_{\mathrm{T2}}\,(b\ell b\ell)$ **(c)** $M_{\mathrm{T2}}\,(\ell\ell)$

Figure 5.21: Distribution of $\mathcal{S}$, $M_{\mathrm{T2}}\,(b\ell b\ell)$, and $M_{\mathrm{T2}}\,(\ell\ell)$ in the same flavour $N_{\text{jets}} \geq 2$, $N_{\text{b-jets}} = 0$ selection with the $\mathcal{S} > 12$ requirement and with $|m_{\ell\ell} - m_Z| \leq 15$. The hashed band represents the experimental systematic uncertainties. The plots are normalised by luminosity.

Figure 5.21 shows the abundance of DY and diboson events in such a control region, after requiring $M_{\mathrm{T2}}\,(\ell\ell) > 100$ GeV to suppress $t\bar{t}$ events. There are no scale factors applied in Fig. 5.21. It is also be seen that $\mathcal{S}$ and $M_{\mathrm{T2}}\,(b\ell b\ell)$ are able to seperate DY and diboson contributions. Therefore, 13 control regions orthogonal to the signal regions are added to the fit by inverting the b-jet and off Z mass requirement in each signal region, i.e. a Z candidate within 15 GeV of m_Z and $N_{\text{b-jets}} = 0$ is required. Statistical uncertainties from limited statistics in the simulated samples are treated as nuisances in each bin. These fits, as discussed in Section 5.6.2, provide scale factors for DY and diboson events. It is evident that the acceptance of DY events is greatly influenced by the detailed properties of the JER modelling. Fortunately, due to the use of the $\mathcal{S}$ variable, the DY yield in the SRs are tiny and an acceptable post-fit description of the DY dominated CR is achieved by including a JER nuisance per era.

5.5.3 $t\bar{t} + Z$ background

One of the main backgrounds in the $M_{\mathrm{T2}}(\ell\ell)$ tail region is $t\bar{t}+Z$, in which the Z boson decays into neutrinos which is depicted in Fig. 5.13(b). These neutrinos add additional missing transverse energy to the event which promotes $t\bar{t}+Z$ events from the bulk into the tail of the $M_{\mathrm{T2}}(\ell\ell)$ distribution. The strategy to select an event sample dominated by $t\bar{t}+Z$ follows the one outlined in [69].

The normalisation of the $t\bar{t}+Z$ background can be estimated in a data-driven way using the 3ℓ sideband. As shown in Fig. 5.22(a), a Z boson decays into two leptons, while one top quark decays leptonically and the other hadronically. The three leptons are

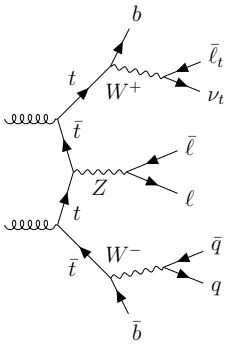

(a) top quark pair decays semi-leptonically and the Z boson into leptons (3ℓ final state).

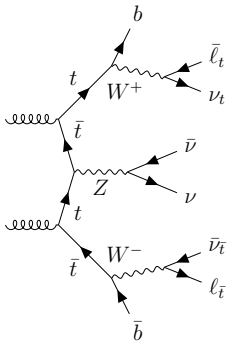

(b) Z boson decays to neutrinos (4ℓ final state).

Figure 5.22: $t\bar{t} + Z$ background processes with three or four lepton final state.

required to exceed p_{T} thresholds of 40, 20 and 20 GeV, respectively. Jets and b-tagged jets are required to have a p_{T} of at least 30 GeV, just as the jets used in the analysis. Two leptons with same flavour are required to have opposite charge and fall within a Z mass window of 10 GeV in order to construct a Z boson candidate. Figure 5.23 shows distributions associated to the leading lepton in the 3ℓ CR. The presence of genuine $p_{\mathrm{T}}^{\mathrm{miss}}$ in the 2ℓ SR and the absence of a $p_{\mathrm{T}}^{\mathrm{miss}}$ related requirement in the CR implies that the estimation procedure is only affected by issues of $p_{\mathrm{T}}^{\mathrm{miss}}$ or jet resolution to a small extent. The 4 different combinations of the 3ℓ selection, that is $\mu\mu\mu$, eee, $\mu\mu e$, and μee, are combined in different control regions, requiring different jet and b-tagged jet multiplicities: 2j/2b, 3j/1b, 3j/2b, 4j/1b and 4j/2b. These control regions are shown in Fig. 5.24 and will be included in the fit.

In addition to the on in 3ℓ channel, also a crude check of the modelling of the $t\bar{t} + Z$ in the 4ℓ channel is performed. As depicted in Fig. 5.22(b), the Z boson decays into two neutrinos there. Such $t\bar{t} + Z$ events in the 4ℓ channel are selected by requring 4 leptons with transverse momentum thresholds 40, 20, 10 and 10 GeV as well as $N_{\text{b-jets}} \geq 1$ and $N_{\text{jets}} \geq 1$. Next, the reconstructed Z candidate is treated as invisible in simulation. Accordingly, it is added to the $p_{\mathrm{T}}^{\mathrm{miss}}$ and all important observables are recalculated. The result is shown in Fig. 5.25 for the $M_{\mathrm{T2}}(\ell\ell)$ and the $p_{\mathrm{T}}^{\mathrm{miss}}$ observable.

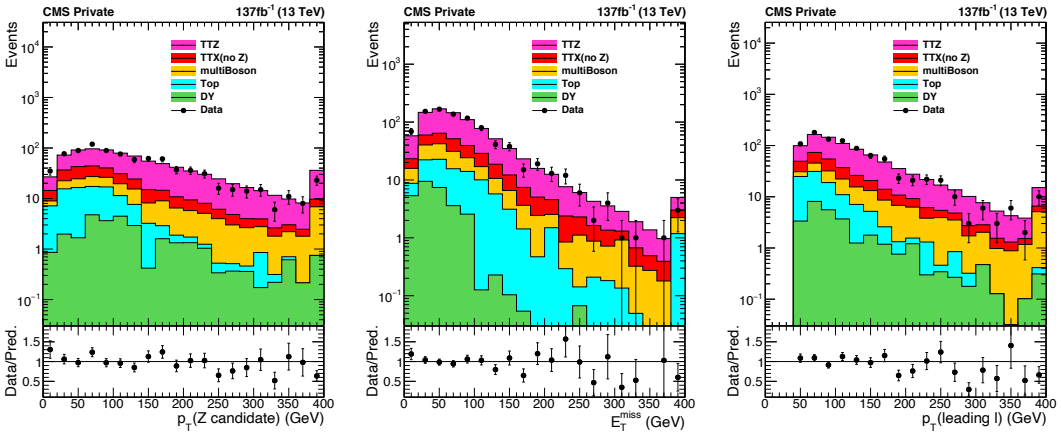

Figure 5.23: Distributions of the Z boson p_{T}, $p_{\mathrm{T}}^{\mathrm{miss}}$ and p_{T} of the leading lepton in the 3ℓ control region.

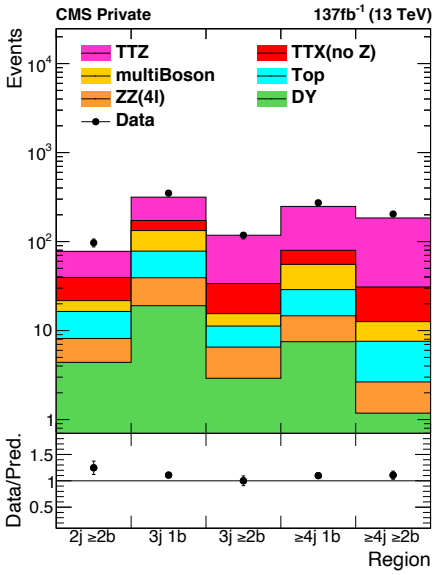

Figure 5.24: $t\bar{t} + Z$ control regions used to extract the normalisation factor, with scale factors applied.

All other observables show similarly good agreement. The reconstructed Z peak in the

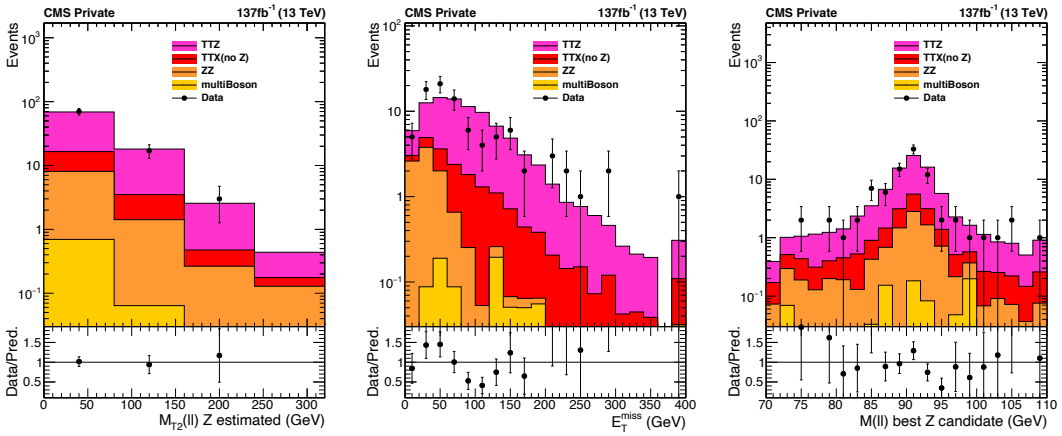

Figure 5.25: Distributions of $M_{\mathrm{T2}}(\ell\ell)$ with the p_{T} of the Z boson candidate added to $p_{\mathrm{T}}^{\mathrm{miss}}$(left), the modified $p_{\mathrm{T}}^{\mathrm{miss}}$ (center), and the mass of the best Z boson candidate (right).

4ℓ channel is also shown. Within the statistical precision of this test, no mismodelling of the $t\bar{t}+Z$ event shape is recognised. The simulated $p_{\mathrm{T}}(Z)$ spectrum shows an admirable agreement with the one from the differential cross section measurement presented in [69].

5.5.4 Rare backgrounds

The backgrounds that differ from the already mentioned ones are collected in a rare backgrounds category in the analysis. Those are made up of $t\bar{t}$ production in association with one or more weak bosons (excluding $t\bar{t}+Z$ and tWZ) or Higgs bosons, or four top quark production. However, their contribution is found to be negligible in all search regions. These rare backgrounds are collectively assigned an uncertainty of 25%.

5.6 Results

The objective of this whole analysis is to set constraints on the top squark–neutralino mass plane in the parameter space of SMS. Computing those limits is only possible, of course, if of the observed and predicted values are compatible with one another. In Section 5.6.1, a brief overview of the statistical methods used for this analysis will be given. The agreement between observed and predicted values will be studied in Sections 5.6.2 and 5.6.3. Finally, the calculated exclusion limits at a 95% confidence level will be presented in Section 5.6.4. The limits are determined with respect to the `T2tt`, `T2bW` and `T8bbllnunu` models introduced in Section 1.3.6. No significant excess over the SM prediction is observed. In other words, the expectations provided by the SM describe the observed data very well.

5.6.1 Statistical methods

In the previous sections the observed number of events, the expected number of background and signal events as well as the corresponding uncertainties have been studied. Based on this information, exclusion limits on the signal strength modifier will be calculated in the $m_{\tilde{t}} - m_{\tilde{\chi}_1^0}$ mass plane in the following. Those limits will be specified using confidence levels (CLs) [70] which is quite common in physics analyses by the ATLAS and CMS collaborations.

Statistical interpretations in this analysis are based on frequentist probabilities. In this realm, the theoretical signal models are considered to be fixed and the probability (likelihood) of the observed data is considered. Bayes' theorem connects the likelihood of the observed data $P(\text{data}|\text{theory})$ with the posterior probability $P(\text{theory}|\text{data})$ via

$$P(\text{theory}|\text{data}) = \frac{P(\text{data}|\text{theory}) \cdot P(\text{theory})}{P(\text{data})} \,.$$

Here, $P(\text{theory})$ is the prior probability which without any prior knowledge is taken to be a flat probability distribution, whereas $P(\text{data})$ essentially serves as a normalisation factor.

At the heart of the CL method lies the the signal strength modifier r. This parameter is a multiplicative factor for the SUSY signal cross section. Expected signal and background yields can be written in terms of r and the so-called nuisance parameters θ_i as $r \cdot s(\theta_i)$ and $b(\theta_i)$, respectively. The background-only hypothesis can the be characterised by $r = 0$, while $r > 0$ corresponds to the background+signal hypothesis.

Given the observed data yields, where data is a set of individual observations $\{n_i\}$, across all signal and control regions, the likelihood function can be written in terms of r and θ as

$$\mathcal{L}(\text{data}|r,\theta) = \prod_{i}^{\text{regions}} \text{Po}(n_i|b_i(\theta) + r \cdot s_i(\theta)) \cdot \prod_{j}^{\text{nuisances}} \rho(\tilde{\theta}_j|\theta_j) \,, \tag{5.9}$$

including all nuisance parameters θ_i.

A nuisance parameters is associated to each source of systematic uncertainties that affects background and signal processes, as described in Section 5.4. It can be modelled by a log-normal probability distribution function (pdf) which is of the form

$$\rho(\tilde{\theta}|\theta) = \frac{1}{\sqrt{2\pi}\,\theta \ln \kappa} \exp\Big(- \frac{\big(\ln \frac{\theta}{\tilde{\theta}}\big)^2}{2(\ln \kappa)^2}\Big) \,.$$

Here, the κ parameter characterises the width of the distribution and $\tilde{\theta}$ is the nominal value for the corresponding nuisance parameter θ. The reason why the log-normal distribution is used here is its distinctive feature that it vanishes at zero making it a suitable pdf for multiplicative factors.

The number of recorded data events per signal or control region bin follows the Poisson distribution

$$\mathrm{Po}(\mathrm{data}|b_i(\theta) + r \cdot s_i(\theta)) = \frac{(b_i + r s_i)^{n_i}}{n_i!} \mathrm{e}^{-(b_i + r s_i)} \,,$$

where n_i corresponds to the number of observed events in region i. Data in this context does not necessarily always refer to actual observations, it may also represent simulated pseudo-data that is utilised for limit setting.

In order to quantify the compatibility of the data and the background-only or background+signal hypothesis, a test statistic is introduced. The test statistic essentially captures all the knowledge about the search such as the expected and observed number of events as well as systematic uncertainties. It is defined [71] using a profile likelihood ratio in the asymptotic limit

$$\tilde{q}_r = -2 \ln \left[\frac{\mathcal{L}(\mathrm{data}|r, \hat{\theta}(r))}{\mathcal{L}(\mathrm{data}|\hat{r}, \hat{\theta})} \right] \,. \tag{5.10}$$

The fraction in the logorithm involves the maximum of the likelihood for a given signal strength modifier r in the numerator, where the nuisance parameter takes the value $\hat{\theta}(r)$, divided by the global maximum of the likelihood given by $\hat{r}$ and $\hat{\theta}$. In the following, one-sided confidence intervals are considered for setting upper limits. Therefore, the constraint $0 \leq \hat{r} \leq r$ is imposed on the signal strength modifier in order to avoid excluding r values smaller than its best fit value.

In order to set limits on the signal strength modifier, the observed test statistic is compared with ones calculated using pseudo-data for the the background-only and the background+signal hypothesis, respectively. Pseudo-data is generated according to Eq. (5.9) using Monte Carlo simulations. A given r is said to be excluded at a confidence level $(1 - \alpha)$ if $\mathrm{CL_s} < \alpha$, where $\mathrm{CL_s}$ is defined as

$$\mathrm{CL_s} = \frac{\mathrm{CL_{b+s}}}{\mathrm{CL_b}} \,.$$

Here, $\mathrm{CL_{b+s}}$ denotes the probability that the test statistic $\tilde{q}_r$ for the background+signal hypothesis is at least as large as the observed one $\tilde{q}_r^{\mathrm{obs}}$

$$\mathrm{CL_{b+s}} = P(\tilde{q}_r^{\mathrm{obs}} \geq \tilde{q}_r|\text{background+signal}) = \int_{\tilde{q}_r^{\mathrm{obs}}}^{\infty} f(\tilde{q}_r|r,\hat{\theta}(r))\ \mathrm{d}\tilde{q}_r\,.$$

The pdf $f(\tilde{q}_r|r,\hat{\theta}(r))$ is constructed using Monte Carlo pseudo-data with fixed values for the nuisance parameters that are obtained by fitting to the observed data. Using the definition of the signal strength modifier, $\mathrm{CL_b}$ is just $\mathrm{CL_{b+s}}\big|_{r=0}$. In this analysis 95% confidence levels (i.e. $\alpha = 0.05$) are considered. The signal strength modifier is varied until $\mathrm{CL_s} = \alpha$ which results in the value for the upper limit on r at a 95% CL. This is, of course, a very computationally intensive process. The cross section of the SUSY signals in this analysis is fixed by theory. Hence, the upper limit on the signal strength modifier can be interpreted as an upper limit on the cross section. A mass point of the signal model can be excluded if the corresponding signal strength modifier r is smaller than unity.

Using the methods discussed here, the exclusion limits for this analysis will be obtained in Section 5.6.4. Before that, however, a control region fit will be performed to obtain a normalisation for the main backgrounds.

5.6.2 Control region fits

In order to determine the normalisation of the main backgrounds ($t\bar{t}$, Drell-Yan, $t\bar{t}+Z$ and Multiboson) a log-likelihood fit is performed in the dedicated control regions, as defined in Table 5.6. More specifically, unconstrained rate parameters are used as input whose values are then extracted after the fit and used as scale factors. Besides the systematic uncertainties discussed in Section 5.4, input uncertainties are provided. The have been assessed based on studies in the preceding analysis [53]. Input uncertainties are assigned to the classes of $t\bar{t}$ events containing non-gaussian mismeasurement and fake leptons. The uncertainty in the total $t\bar{t}$ prediction from non-gaussian mismeasurement ranges from sub-percent in the $t\bar{t}$ CR to 25% in signal regions with $M_{\mathrm{T2}}(\ell\ell) > 140$ GeV, while it reaches values up to 20% from the uncertainty in the rate of fake leptons. The list of custom input uncertainties is summarised in Table 5.8. Note that the scale factor uncertainties for Drell-Yan, $t\bar{t}+Z$ and Multiboson are only applied in the signal regions, which will be utilised only in the next section for the signal extraction.

The CR yields are shown in Fig. 5.26 before and after the fit. The first two bins correspond to the normalisation region of the $t\bar{t}$ background, where $M_{\mathrm{T2}}(\ell\ell) < 100$ GeV. For bins 2–6 different jet and b-tagged jet multiplicities are used, as well as a 3ℓ selection, to constrain the $t\bar{t}+Z$ background. Bins 7–19 are control regions enriched in DY and Multiboson events, by inverting the off-Z and the b-tag requirements of the signal regions. The extracted results of the rate parameters are listed in Table 5.9. Also the

Table 5.8: Correlation pattern of the nuisances and rate parameters related to the background estimation procedures. The experimental uncertainties (JER, JEC, b-tagging, leptonSF etc.) are accounted for but not shown here.

nuisance parameter	input uncertainty
$t\bar{t}$ rate parameter	unconstrained
$t\bar{t} + Z$ rate parameter	unconstrained
DY rate parameter	unconstrained
Multiboson rate parameter	unconstrained
rate of non-gaus mismeas.	0.2 – 25%
rate of fakes in $t\bar{t}$	0.2 – 20%
DY SF unc. (SR only)	25%
$t\bar{t} + Z$ SF unc. (SR only)	20%
MB SF unc. (SR only)	25%
rare processes ($t\bar{t}$+X(X))	25%

normalisation factor of the rare backgrounds is listed which does not get significantly pulled from unity.

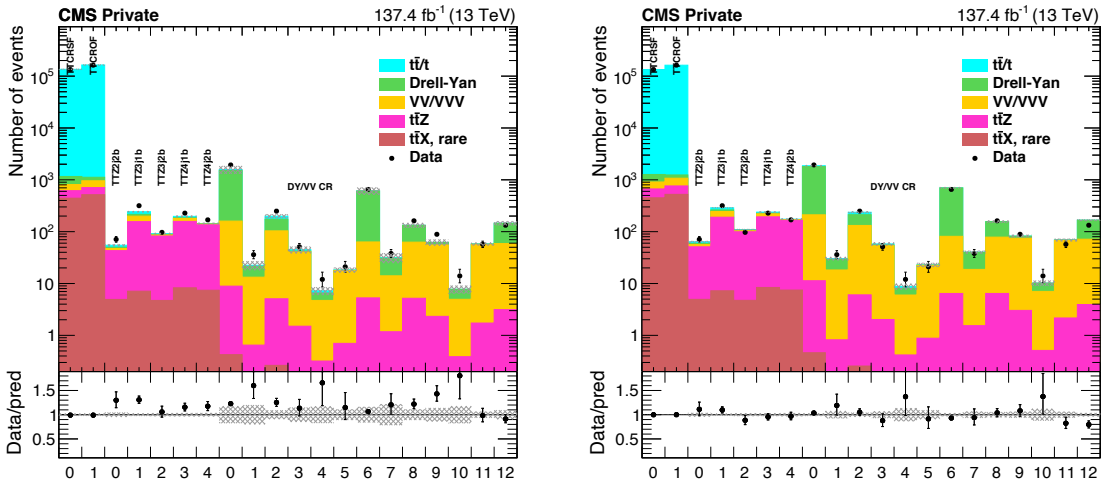

(a) pre-fit **(b)** post-fit

Figure 5.26: Control regions with systematic uncertainties, before and after the maximum likelihood fit.

Further studies of the nuisance parameters are displayed in Appendix B. Figure B.1 shows the pulls and constraints on the various systematic uncertainties induced by the maximum likelihood fit.

Table 5.9: Normalisation factors for the backgrounds extracted by the fit to data in the control regions for all years separately and combined, with the corresponding uncertainty assigned on the normalisation.

Process	2016	2017	2018	combined
$t\bar{t}/t$	0.98 ± 0.04	1.01 ± 0.04	0.98 ± 0.04	0.99 ± 0.04
$t\bar{t} + Z$	1.33 ± 0.27	1.23 ± 0.25	1.19 ± 0.24	1.24 ± 0.25
Drell-Yan	1.29 ± 0.32	1.22 ± 0.31	1.07 ± 0.26	1.14 ± 0.28
MultiBoson	1.39 ± 0.35	1.01 ± 0.25	1.21 ± 0.30	1.27 ± 0.32
Rare	1.03 ± 0.26	1.04 ± 0.26	1.01 ± 0.25	1.03 ± 0.26

5.6.3 Combined fit and limit setting

In preparation for limit setting, a maximum likelihood fit is performed on the signal and control region yields at the same time. The information needed to perform the fit comprises the data, signal and background yields in each of the search regions. Signal yields are available for each mass point in the considered sector of the top squark-neutralino mass plane. Figure 5.27 shows the distributions according to which the 13 SRs are constructed. As already mentioned, the systematic variations are added

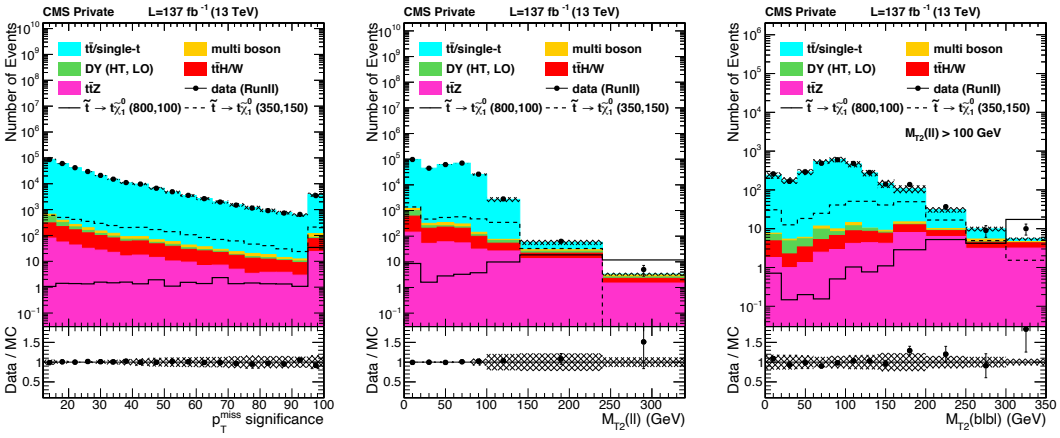

Figure 5.27: Signal regions with a $N_{\text{jets}} \geq 2$, $N_{\text{b-jets}} \geq 1$ selection, for SF and OF combined. The usual preselections are applied. For the first two plots MC yields are normalised to data using the yields at $M_{\text{T2}}(\ell\ell) > 100$ GeV. The $M_{\text{T2}}(b\ell b\ell)$ plot is normalised by luminosity and a cut $M_{\text{T2}}(\ell\ell) > 100$ GeV is applied to select the signal region distribution. The hashed band represents the experimental systematic uncertainties.

as nuisance parameters to the fit. The statistical uncertainties of signal and background samples are treated as separate nuisance parameters since they are considered uncorrelated for each sample and region. The systematic uncertainties on the main backgrounds are somewhat reduced due to the scale factors from the post-fit nuisance parameters after performing the maximum-likelihood fit on the CRs only. Figure 5.28

summarises the background predictions in all search region before and after the fit, respectively.

Besides, the impacts of the nuisance parameters are tested on the signal strength of the `T2tt` signal with $m_{\tilde{t}} = 800$ and $m_{\tilde{\chi}_1^0} = 100$ for the signal extraction fit of all signal regions. The result for the nuisances of the combined fit, sorted by their impact on $\hat{r}$, are shown in Fig. B.2-B.3 in Appendix B.

Following the procedure for setting limits in Section 5.6.1, a likelihood function is formed over all search regions with Poisson distributed data and nuisance parameters modelled by a log-normal distribution. The profile likelihood ratio in the asymptotic approximation as introduced in Eq. (5.10) is used as the test statistic. Finally, exclusion limits on the signal cross section are calculated at a 95% confidence levels using the asymptotic CL_s criterion [72, 70]. The results of the exclusion limits obtained from the combination of all 26 signal region bins will be discussed in the next section.

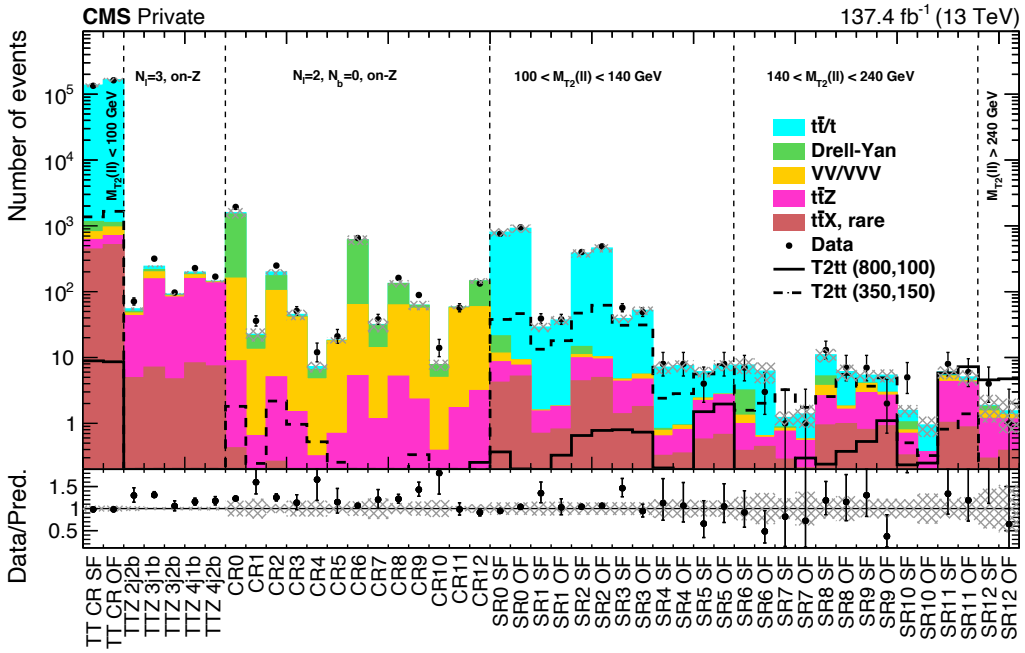

(a) pre-fit search region yields

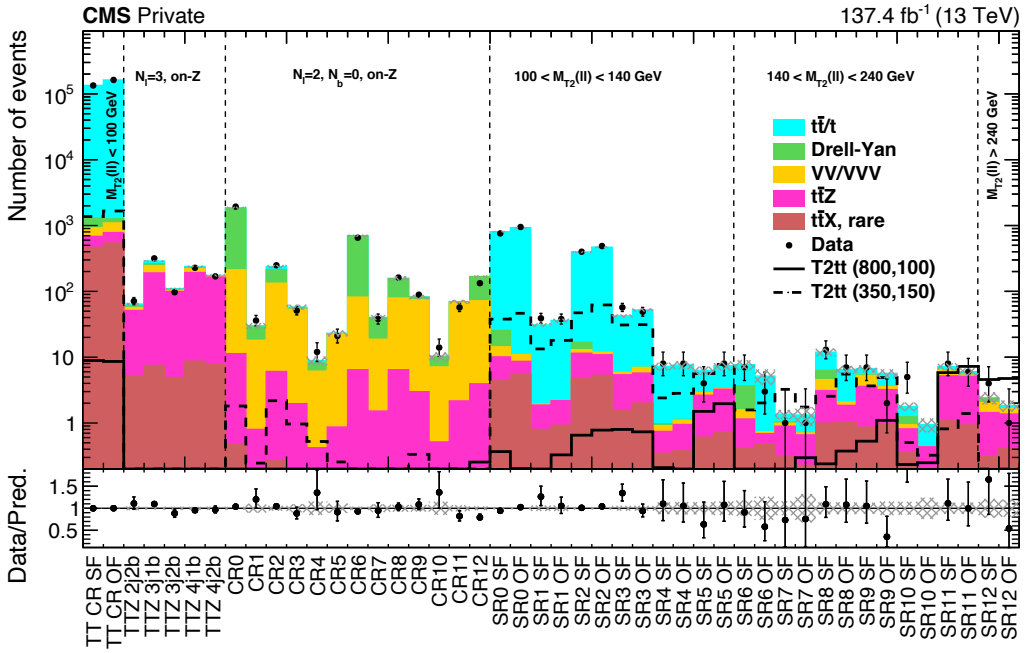

(b) post-fit search region yields

Figure 5.28: Predicted background and signal yields for the control and signal regions, compared to observation before performing the maximum likelihood fit (pre-fit). The M_{T2} ($b\ell b\ell$) region are devided into low and high $p_{\mathrm{T}}^{\mathrm{miss}}$ significance, and further split into same flavour and opposite flavour events. For reference, the signal region definitions are given in Table 5.5.

5.6.4 Exclusion limits

The results of the exclusion limits on the signal strength modifier are presented in the $m_{\tilde{t}} - m_{\tilde{\chi}_1^0}$ plane in Figs. 5.29 and 5.30. The colour map in Fig. 5.29 represents the 95% CL on the upper limit on the product of the cross section and the square of the branching ratio $\sigma \times \mathcal{B}^2$. In the simplified models discussed here, the branching fraction of the top squark pair into the respective products is assumed to be 100%. Since the cross section is fixed by theory parameters, the limit is intimately linked to the one on the signal strength modifier value. The dashed red lines represent the expected exclusion limit at 95% CL and the region containing 68% of the distribution of limits expected under the background-only hypothesis. The area below the thick black curve represents the observed exclusion region at 95% CL. The thin black lines show the effect of the theoretical uncertainties in the signal cross section.

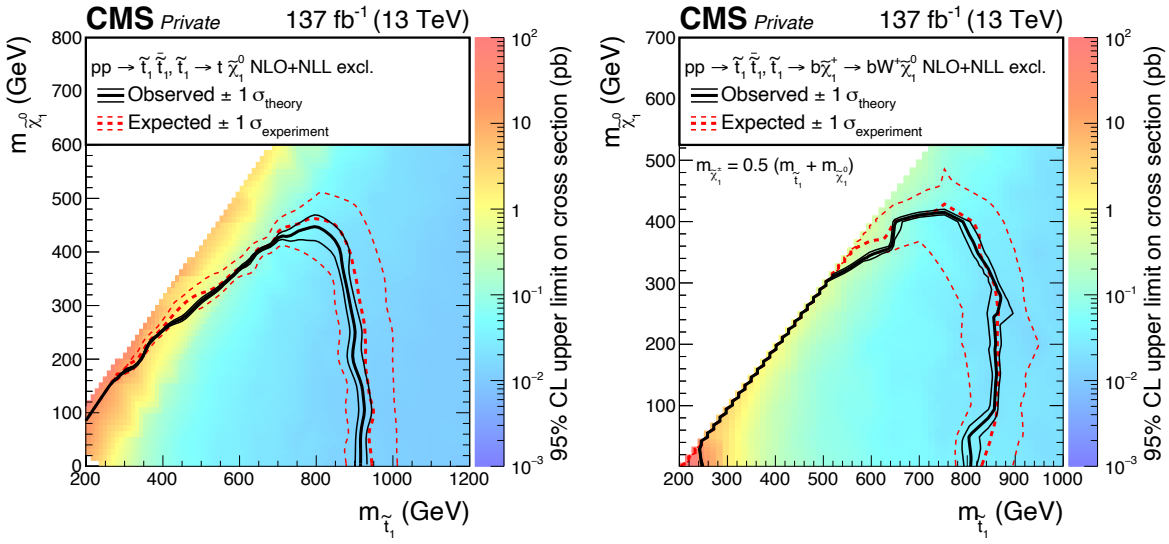

(a) `T2tt` model **(b)** `T2bW` model

Figure 5.29: 95% CL upper limit for the `T2tt` and for the `T2bW` model.

As displayed in Fig. 5.29a, for the `T2tt` model mass configurations with $m_{\tilde{\chi}_1^0}$ up to 440 GeV and $m_{\tilde{t}_1}$ up to 900 GeV are excluded, assuming that the top quarks are unpolarised. The results for the `T2bW` model is shown in Fig. 5.29b. For this model, mass configurations with $m_{\tilde{\chi}_1^0}$ up to 400 GeV and $m_{\tilde{t}_1}$ up to 850 GeV are excluded. Both the `T2tt` and the `T2bW` model's observed contours are well within one standard deviation of the corresponding expected contours.

Another interpretion of the results is done in terms of the `T8bbllnunu` model. In this model the top squarks undergo a cascade decay to neutralinos via an intermediate chargino and a slepton, as introduced in Section 1.3.6. The unknown masses of the two additional new particles are fixed via the following parametrisation. The chargino mass is chosen exactly halfway between $m_{\tilde{t}}$ and $m_{\tilde{\chi}_1^0}$. The slepton mass is parametrised

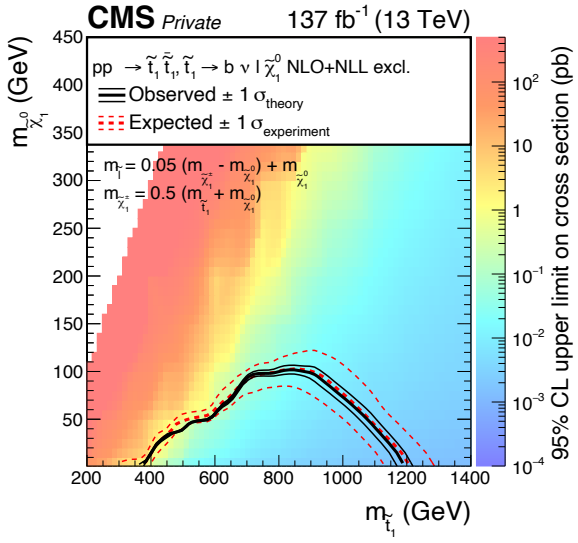

(a) `T8bbllnunu` with $x = 0.05$

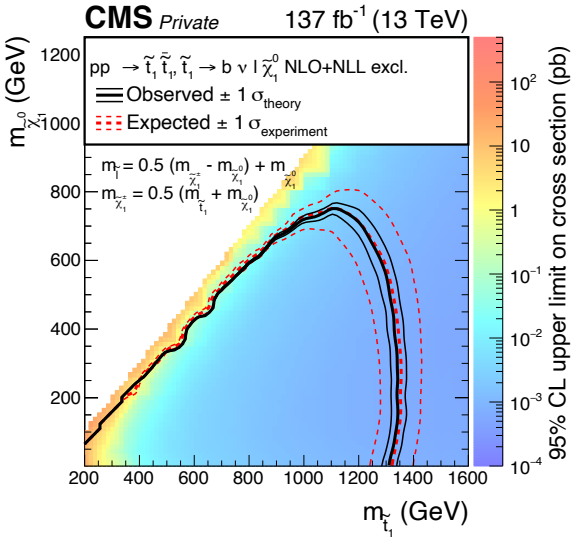

(b) `T8bbllnunu` with $x = 0.5$

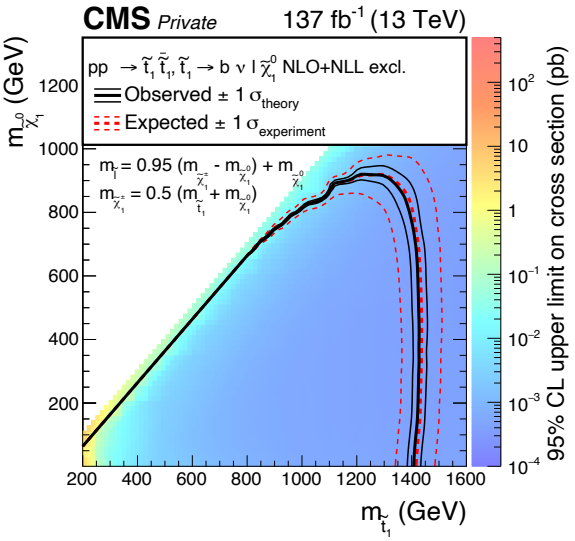

(c) `T8bbllnunu` with $x = 0.95$

Figure 5.30: 95% CL upper limit for `T8bbllnunu` model with three different slepton mass parameterisations, according to Eq. (5.11).

as a function of $m_{\tilde{\chi}_1^0}$ and $m_{\tilde{\chi}_1^\pm}$,

$$m_{\tilde{\ell}} = x \cdot (m_{\tilde{\chi}_1^\pm} - m_{\tilde{\chi}_1^0}) + m_{\tilde{\chi}_1^0} \,. \tag{5.11}$$

In the following the results are interpreted for three different slepton mass parameters according to

$$x = 0.05, 0.5, \text{and } 0.95 \,.$$

The expected and observed limits on the production cross section in the `T8bbllnunu` model with these three different slepton mass parameterisations are shown in Fig. 5.30.

In the interpretation in Fig. 5.30 (a) for $x = 0.05$ the observed exclusion reaches masses of the top squark of $m_{\tilde{t}} = 1.2$ TeV, while masses of for the LSP reach values of 180 GeV. For a mass parameter of the slepton of $x = 0.5$ in Fig. 5.30 (b) the sensitivity is somewhat higher. Top squark masses up to 1300 GeV and $m_{\tilde{\chi}_1^0} < 750$ GeV are excluded. For $x = 0.95$, the limit contour is shown in Fig. 5.30 (c). There the observed exclusion of top squark masses approaches $m_{\tilde{t}} = 1.4$ TeV and the exclusion for $m_{\tilde{\chi}_1^0}$ up to 900 GeV. In summary, the sensitivity in the `T8bbllnunu` model strongly depends on the intermediate slepton mass and is largest when $x = 0.95$. The rather low exclusion region for the case where $x = 0.05$ can be explained by the soft slepton mass which is close to the neutralino mass.

5.6.5 Comparison with other results

The exclusion limits presented in the previous section can be compared with previous analyses by CMS [53] and ATLAS [73]. These two analyses have focussed on the similar SMS signal models in the dilepton final state with data from the 2016 LHC data taking at a center-of-mass energy of 13 GeV. No significant excess was observed in these analyses. Table 5.10 summarises the upper bounds of the exclusion limits in the two analyses and this one, respectively. Overall, the results presented here achieve an expansion of the excluded regions for all of the five signal models discussed here. The limits for the top squark mass are improved by about 100 GeV for all signal models compared to [53]. In terms of neutralino masses this analysis scores better by more than 100 GeV for most SMS models as well. In the case of `T2bW`, however, the excluded neutralino mass range is only increased by about 20 GeV compared to [73]. The neutralino mass limit for `T8bbllnunu` with $x = 0.05$ is increased by about 40 GeV.

Table 5.10: Upper bounds of the exclusion limits for Full Run 2 (this analysis), CMS 2016 data [53] and ATLAS 2016 data [73].

		$m_{\tilde{t}_1}$	$m_{\tilde{\chi}_1^0}$
`T2tt`	Full Run 2 (this analysis)	< 900 GeV	< 440 GeV
	CMS 2016 data [53]	< 800 GeV	< 350 GeV
	ATLAS 2016 data [73]	< 730 GeV	< 300 GeV
`T2bW`	Full Run 2 (this analysis)	< 850 GeV	< 400 GeV
	CMS 2016 data [53]	< 750 GeV	< 320 GeV
	ATLAS 2016 data [73]	< 700 GeV	< 380 GeV
`T8bbllnunu` x=0.05	Full Run 2 (this analysis)	< 1200 GeV	< 100 GeV
	CMS 2016 data [53]	< 1050 GeV	< 60 GeV
`T8bbllnunu` x=0.5	Full Run 2 (this analysis)	< 1300 GeV	< 750 GeV
	CMS 2016 data [53]	< 1200 GeV	< 600 GeV
`T8bbllnunu` x=0.95	Full Run 2 (this analysis)	< 1400 GeV	< 900 GeV
	CMS 2016 data [53]	< 1300 GeV	< 800 GeV

6 | Conclusion

A search for top squark pair production has been presented for final states with two leptons, at least one b-tagged jet, and large missing transverse momentum in data. The data considered in this analysis corresponds to an integrated luminosity of 137 fb^{-1} in pp collisions collected at a center-of-mass energy of 13 TeV in the CMS detector at the LHC.

An efficient standard model background reduction has been achieved using dedicated kinematic variables. Thereby, the large background of dileptonic $t\bar{t}$ events has been suppressing by several orders of magnitude. Furthermore, the shape and normalisations of the main backgrounds have been studied in dedicated control regions. On top of that, several sources of systematic uncertainties of the background prediction have been closely examined. The largest uncertainties arise from jet energy resolution and unclustered energy. Other uncertainties are way below 15%. Systematic uncertainties of simulated signal events have been studied as well.

No evidence for a deviation from the expected background from the standard model has been observed. Therefore, the results were interpreted in several simplified models for supersymmetric top squark pair production. Limits on the production cross section in the top squark–neutralino mass plane at a 95% confidence level have been set. For the `T2tt` model which describes the decay $\tilde{t}_1 \to t\tilde{\chi}_1^0$, top squark masses up to 900 GeV and neutralino masses less than 440 GeV are excluded. In the `T2bW` model with $\tilde{t}_1 \to b\tilde{\chi}_1^\pm \to bW^\pm\tilde{\chi}_1^0$ decays, $\tilde{t}_1$ masses below 850 GeV and $\tilde{\chi}_1^0$ masses below 400 GeV are excluded. In this case a chargino mass equal to the mean of the $\tilde{t}_1$ and the $\tilde{\chi}_1^0$ masses is assumed. The decay $\tilde{t}_1 \to b\tilde{\chi}_1^\pm \to b\nu\tilde{\ell} \to b\nu\ell\tilde{\chi}_1^0$ in the `T8bbllnunu` model has a 100% branching into dilepton final states. It turns out that the sensitivity depends on the intermediate particle masses. The chargino mass is taken as the mean of the $\tilde{t}_1$ and the $\tilde{\chi}_1^0$ masses again and for the slepton mass three different scenarios have been considered. The strongest exclusion is obtained if the slepton mass is close to the chargino mass. In this case, excluded masses reach up to 1400 GeV for the top squark mass and neutralino masses below 900 GeV are excluded.

The analysis was pre-approved by the CMS collaboration on January 29th, 2020.

A | Background modelling check in sideband selections

The modelling of the main backgrounds is checked in sideband selections which feature high yields for specific backgrounds. Figure A.1 shows distributions in the same selection that is used to measure the DY and Multiboson normalisation (same flavour dileptons, inside Z mass window, $N_{\text{b-jets}} = 0$). On the other hand, figure A.2 shows a more $t\bar{t}$ and Multiboson enriched selection (especially in the $M_{\text{T2}}(\ell\ell)$ tails) by only selecting opposite flavour events, while events with b-tagged jets are vetoed. This region is only used to cross check the modelling. Figure A.3 shows the combined same and opposite flavour channels, after vetoing the Z mass window for same flavour events.

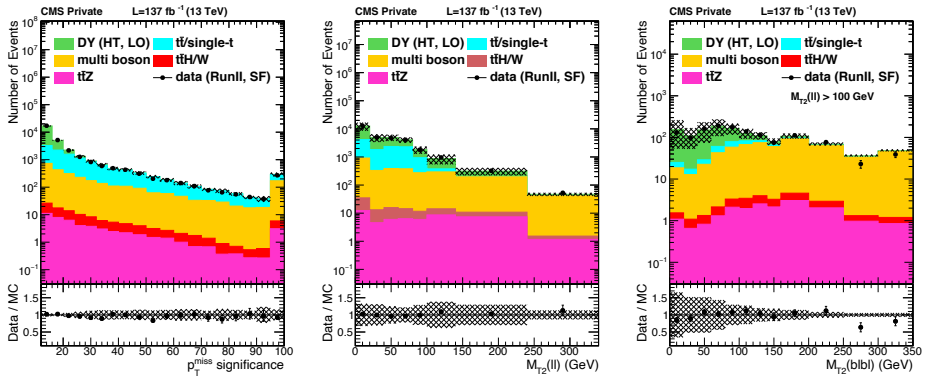

Figure A.1: Same flavour control region (all three years combined) with a $N_{\text{jets}} \geq 2$, $N_{\text{b-jets}} = 0$ selection reversing the Z mass window $|m_{\ell\ell} - m_Z| \leq 15$. The normal preselection is applied. For the $\mathcal{S}$ plot, MC yields are normalised to data using the yields for $M_{\text{T2}}(\ell\ell) < 100$ GeV to reflect the background estimation for $t\bar{t}$. The second and third plot is luminosity normalised. The hashed band represents the experimental systematic uncertainties.

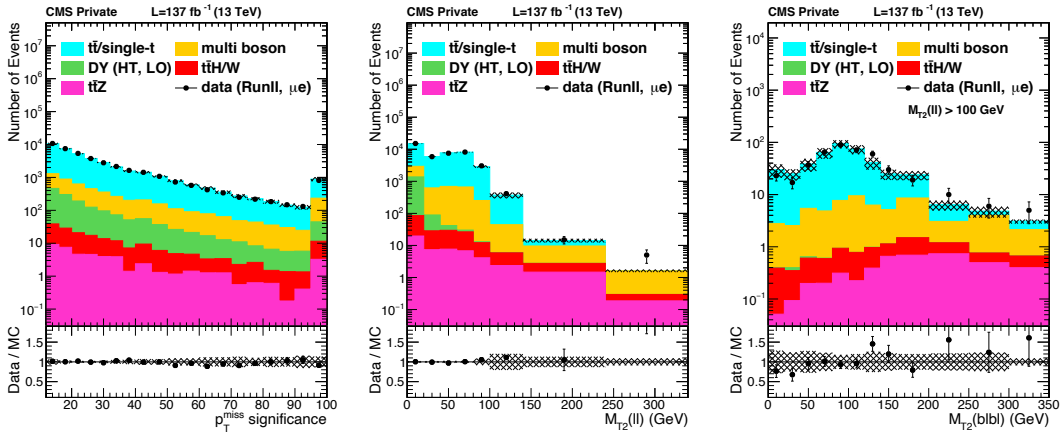

Figure A.2: Opposite flavour (μe, all three years combined) control region with a $N_{\text{jets}} \geq 2$, $N_{\text{b-jets}} = 0$ selection. All other preselection cuts are applied. For the first two plots MC yields are normalised to data using the yields at $M_{\text{T2}}(\ell\ell) < 100$ GeV. The $M_{\text{T2}}(b\ell b\ell)$ plot is normalised by luminosity. The hashed band represents the experimental systematic uncertainties.

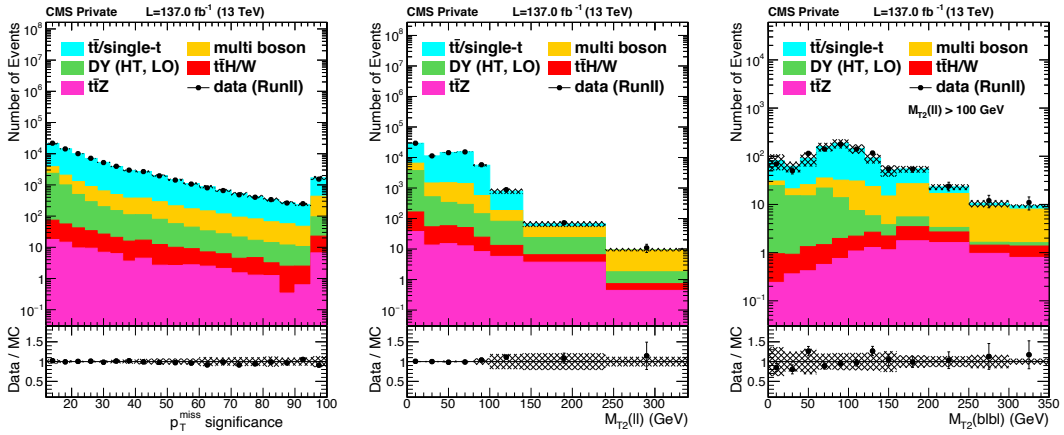

Figure A.3: Control regions (all three years combined) with a $N_{\text{jets}} \geq 2$, $N_{\text{b-jets}} = 0$ selection, combined for SF and OF. All other preselection cuts are applied. For $\mathcal{S}$ and $M_{\text{T2}}(\ell\ell)$ plots MC yields are normalised to data using the yields at $M_{\text{T2}}(\ell\ell) < 100$ GeV. The $M_{\text{T2}}(b\ell b\ell)$ plot is normalised by luminosity. The hashed band represents the experimental systematic uncertainties.

B | Pulls, nuisances and correlations

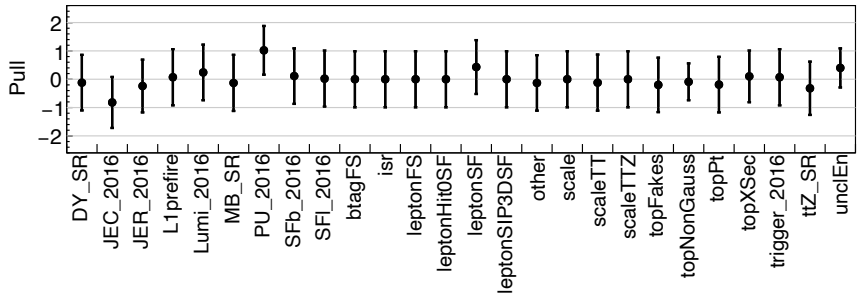

(a) 2016

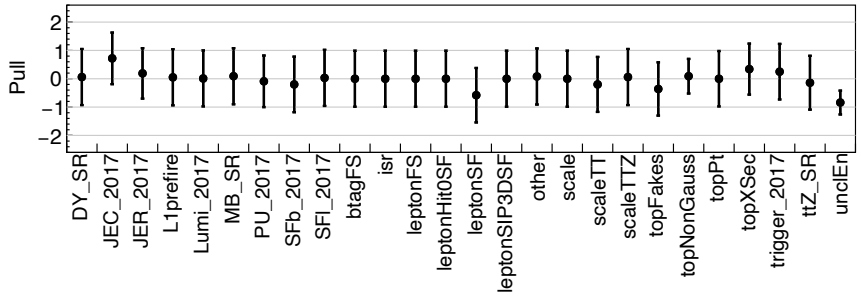

(b) 2017

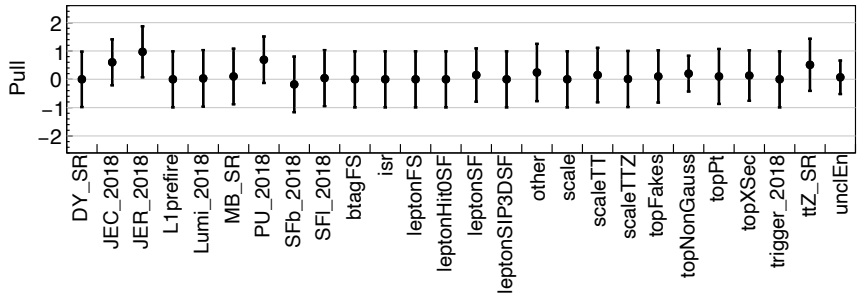

(c) 2018

Figure B.1: Pulls and constraints on the systematic uncertainties for the 2016, 2017 and 2018 data taking periods.

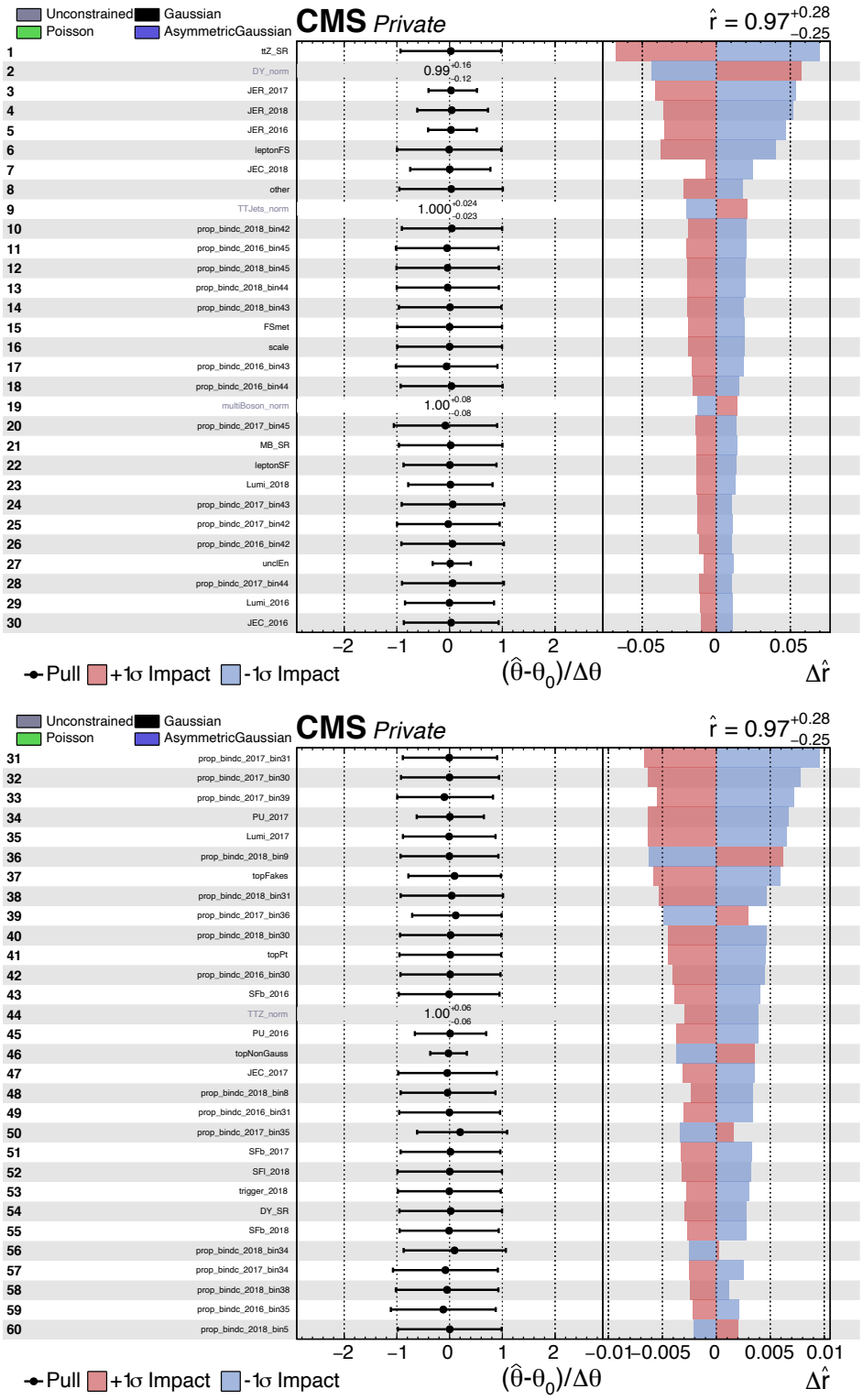

Figure B.2: Impact of the leading nuisances of the combined fit ranked by $\hat{r}$ for T2tt_800_100.

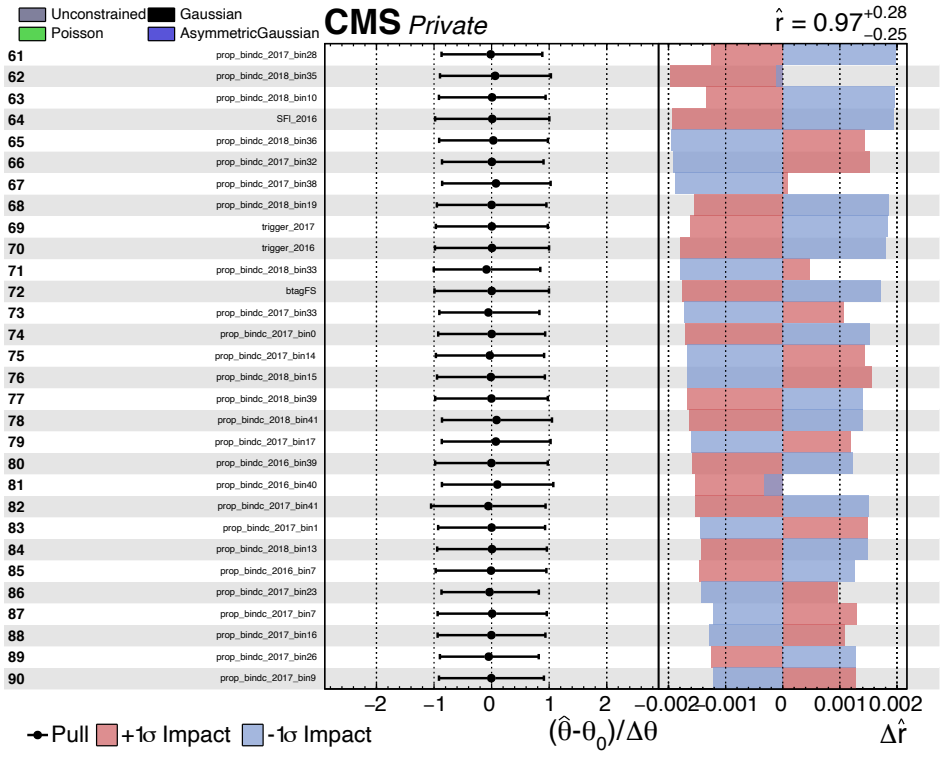

Figure B.3: Impact of the leading nuisances of the combined fit ranked by $\hat{r}$ for T2tt_800_100.

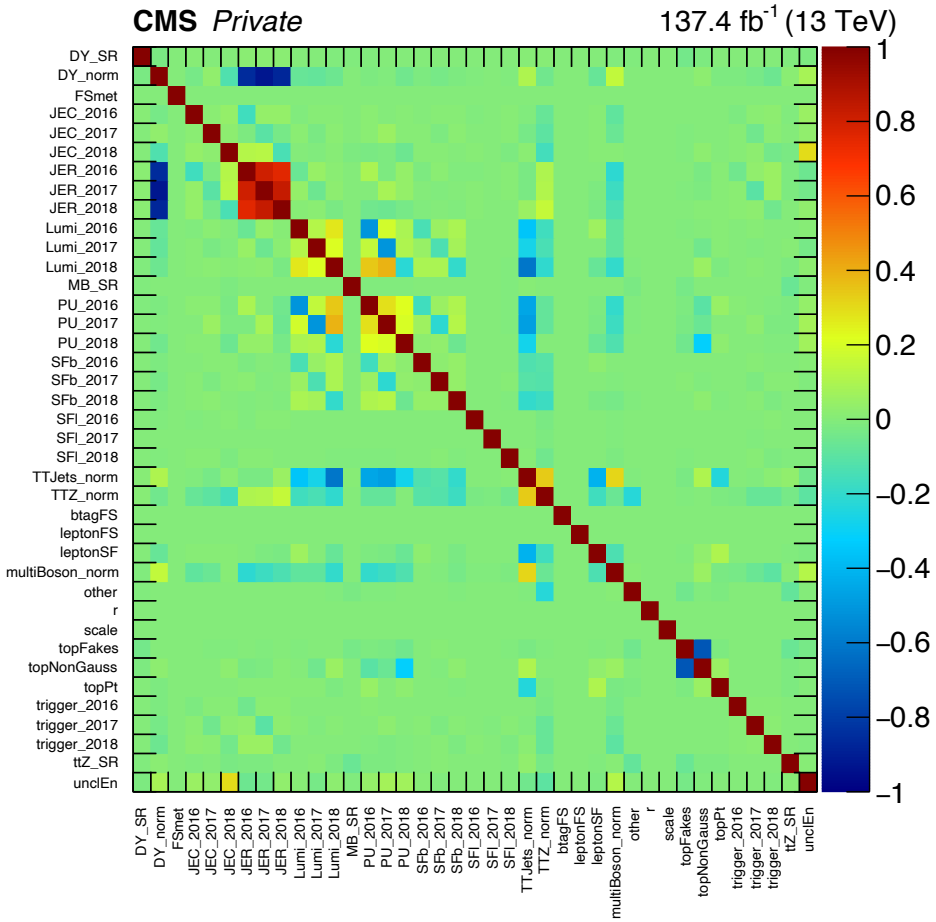

Figure B.4: Correlation pattern of the systematic uncertainties after the combined fit.

List of Figures

1.1 SM gauge bosons and the interactions they mediate. 3

1.2 Different generations of SM fermions. The small coloured circles symbolise each particle's charges under the fundamental forces in the SM. . 4

1.3 One-loop corrections to the Higgs mass parameter Δm_H^2. 12

1.4 Two-loop renormalisation group evolution of the inverse gauge couplings $\alpha^{-1}(Q)$ in the Standard Model (dashed lines) and the MSSM (solid lines) [26]. 16

1.5 Leading order Feynman diagrams (quark-antiquark annihilation and gluon-gluon fusion) for top squark pair production. 17

1.6 SUSY Signals 18

1.7 Illustration of the masses of the intermediate chargino $\widetilde{\chi}_1^{\pm}$ and slepton $\tilde{\ell}$ for the `T8bbllnunu` model. 19

2.1 Schematic illustration of CERN's accelerator complex [35]. 22

2.2 Illustration of LHC dipole magnet [30]. 23

3.1 Schematic illustration of the CMS detector components. The person next to the forward calorimeter is to get an idea for the size of the detector [36]. 25

3.2 Slice of the CMS detector structure [39]. 26

3.3 Illustration of the detector components and the η region they belong to [40]. 27

3.4 Predicted magnitude of the B-field (left) and the field lines (right) in the volume covered by the CMS detector [41]. 28

3.5 Schematic cross section through the CMS tracker. Each line represents a detector module [32]. 29

3.6 Layout of the ECAL showing the arrangement of crystal modules [32]. . 30

3.7 Longitudinal view of the CMS detector showing the locations of the hadron barrel (HB), endcap (HE), outer (HO) and forward (HF) calorimeters [32]. 31

3.8 Longitudinal layout of one quadrant of the CMS detector, showcasing the muon system. The four DT stations in the barrel (green), the four CSC stations in the endcap (blue), and the RPC stations (red) are shown [45]. 33

3.9 Architecture of the Level-1 Trigger [32]. 33

5.1 Trigger efficiencies for the ee (top), $e\mu$ (center) and $\mu\mu$ (bottom) channel, for 2016, 2017 and 2018 (from left to right). 44

5.2 $M_{\mathrm{T2}}\,(\ell\ell)$ distribution showcasing its disriminative power. $t\bar{t}$ (light blue) has an upper bound at the W boson mass around 100 GeV, while the signals (black lines) show no upper bound. 47

5.3 Dependence of the average significance $\mathcal{S}$ on pileup, for dimuon events and single-electron events. For processes with no genuine $p_{\mathrm{T}}^{\mathrm{miss}}$ a small dependence is observed, whereas in events with intrinsic $p_{\mathrm{T}}^{\mathrm{miss}}$ the behavior of $\mathcal{S}$ depends strongly on pileup. 49

5.4 Distribution of $\boldsymbol{p}_{\mathrm{T}}^{\mathrm{miss}}$ significance in a $Z \to \ell\ell$ selection, requiring at least two jets, none of which is b-tagged. Events with no genuine $\boldsymbol{p}_{\mathrm{T}}^{\mathrm{miss}}$ like Drell-Yan follow a χ^2 distribution with two degrees of freedom (red line). 50

5.5 Pileup distributions for 2016, 2017, and 2018 [63]. 51

5.6 Distribution of $p_{\mathrm{T}}^{\mathrm{miss}}$, the "kinematical" $p_{\mathrm{T}}^{\mathrm{miss}}$ significance and $\mathcal{S}$ for varying pileup in 2016 simulation for a least two jets and two leptons consistent with a Z boson. 52

5.7 Simulated $\mathcal{S}$ distribution after a $N_{\text{jets}} > 2$, $N_{\text{b-jets}} > 1$ preselection. . . . 52

5.8 Comparison of the expected limits in the $m_{\tilde{t}}$-$m_{\tilde{\chi}_1^0}$ mass plane for the signal regions defined in [53] and the ones in Table 5.5, respectively. . 53

5.9 Distribution of vertex multiplicity, missing transverse energy and $p_{\mathrm{T}}^{\mathrm{miss}}$ significance where the DY contribution is split in bins of $\mathcal{S}$ (a) and N_{PV} (b and c). 54

5.10 Distribution of vertex multiplicity in 2018 data in a SF selection with a Z candidate and $N_{\text{jets}} \geq 2$ and $N_{\text{b-jets}} = 0$ for three different values for the minimum bias cross section used in the PU reweighting. 54

5.11 Distribution of $p_{\mathrm{T}}^{\mathrm{miss}}$ in 2018 SF data in a selection with a Z candidate and $N_{\text{jets}} \geq 2$ and $N_{\text{b-jets}} = 0$, and with nominal PU reweighting and with a minimum bias cross section of 76.1mb. 55

5.12 Distribution of $\mathcal{S}$ in the $N_{\text{jets}} \geq 2$ and $N_{\text{b-jets}} = 0$ control region. 58

5.13 Main backgrounds in this analysis. 65

5.14 $M_{\mathrm{T2}}(\ell\ell)$ distributions of $t\bar{t}$ background in $\mu\mu$ channel with $N_{\text{jets}} \geq 2$, $N_{\text{b-jets}} \geq 1$ for the respective years. 66

5.15 Distribution of $M_{\mathrm{T2}}(\ell\ell)$ in the same flavour channel of the $N_{\text{jets}} \geq 2$, $N_{\text{b-jets}} = 0$ selection without the $\mathcal{S} > 12$ requirement for the three data taking periods. 67

5.16 Fake and non-prompt $t\bar{t}$ backgrounds. 67

5.17 $M_{\mathrm{T2}}(\ell\ell)$ distributions in the three lepton control region with all lepton channels combined for the years 2016, 2017 and 2018. Changes of flavour and p_{T} due to the lepton swapping are taken into account. MC yields are normalised to data using the yields at $M_{\mathrm{T2}}(\ell\ell) < 100$ GeV. 68

5.18 Comparison of the three lepton simulation (blue area) and the two-lepton simulation with inverted isolation requirements on one of the leptons (red line), normalised at $M_{\mathrm{T2}}(\ell\ell) > 100$ GeV. The plot is reproduced from the 2016 analysis [53]. 69

5.19 Transverse mass for non-isolated leptons (top); $M_{T2}(\ell\ell)$ for lepton pair consisting of one isolated and one non-isolated lepton (bottom) for 2016, 2017 and 2018 (from left to right). 70

5.20 Isolation of the loose lepton when the veto on loose leptons is lifted for muons (top) and electrons (bottom) for 2016 (left), 2017 (middle), and 2018 (right). 71

5.21 Distribution of $\mathcal{S}$, $M_{\mathrm{T2}}(b\ell b\ell)$, and $M_{\mathrm{T2}}(\ell\ell)$ in the same flavour $N_{\text{jets}} \geq 2$, $N_{\text{b-jets}} = 0$ selection with the $\mathcal{S} > 12$ requirement and with $|m_{\ell\ell} - m_Z| \leq 15$. The hashed band represents the experimental systematic uncertainties. The plots are normalised by luminosity. 72

5.22 $t\bar{t} + Z$ background processes with three or four lepton final state. . . . 73

5.23 Distributions of the Z boson p_{T}, $p_{\mathrm{T}}^{\text{miss}}$ and p_{T} of the leading lepton in the 3ℓ control region. 74

5.24 $t\bar{t}+Z$ control regions used to extract the normalisation factor, with scale factors applied. 74

5.25 Distributions of $M_{\mathrm{T2}}(\ell\ell)$ with the p_{T} of the Z boson candidate added to $p_{\mathrm{T}}^{\text{miss}}$(left), the modified $p_{\mathrm{T}}^{\text{miss}}$ (center), and the mass of the best Z boson candidate (right). 75

5.26 Control regions with systematic uncertainties, before and after the maximum likelihood fit. 79

5.27 Signal regions with a $N_{\text{jets}} \geq 2$, $N_{\text{b-jets}} \geq 1$ selection, for SF and OF combined. The usual preselections are applied. For the first two plots MC yields are normalised to data using the yields at $M_{\text{T2}}(\ell\ell) > 100$ GeV. The $M_{\text{T2}}(b\ell b\ell)$ plot is normalised by luminosity and a cut $M_{\text{T2}}(\ell\ell) > 100$ GeV is applied to select the signal region distribution. The hashed band represents the experimental systematic uncertainties. 80

5.28 Predicted background and signal yields for the control and signal regions, compared to observation before performing the maximum likelihood fit (pre-fit). The $M_{\text{T2}}(b\ell b\ell)$ region are devided into low and high $p_{\text{T}}^{\text{miss}}$ significance, and further split into same flavour and opposite flavour events. For reference, the signal region definitions are given in Table 5.5. 82

5.29 95% CL upper limit for the `T2tt` and for the `T2bW` model. 83

5.30 95% CL upper limit for `T8bbllnunu` model with three different slepton mass parameterisations, according to Eq. (5.11). 84

A.1 Same flavour control region (all three years combined) with a $N_{\text{jets}} \geq 2$, $N_{\text{b-jets}} = 0$ selection reversing the Z mass window $|m_{\ell\ell} - m_Z| \leq 15$. The normal preselection is applied. For the $\mathcal{S}$ plot, MC yields are normalised to data using the yields for $M_{\text{T2}}(\ell\ell) < 100$ GeV to reflect the background estimation for $t\bar{t}$. The second and third plot is luminosity normalised. The hashed band represents the experimental systematic uncertainties. 89

A.2 Opposite flavour (μe, all three years combined) control region with a $N_{\text{jets}} \geq 2$, $N_{\text{b-jets}} = 0$ selection. All other preselection cuts are applied. For the first two plots MC yields are normalised to data using the yields at $M_{\text{T2}}(\ell\ell) < 100$ GeV. The $M_{\text{T2}}(b\ell b\ell)$ plot is normalised by luminosity. The hashed band represents the experimental systematic uncertainties. 90

A.3 Control regions (all three years combined) with a $N_{\text{jets}} \geq 2$, $N_{\text{b-jets}} = 0$ selection, combined for SF and OF. All other preselection cuts are applied. For $\mathcal{S}$ and $M_{\text{T2}}(\ell\ell)$ plots MC yields are normalised to data using the yields at $M_{\text{T2}}(\ell\ell) < 100$ GeV. The $M_{\text{T2}}(b\ell b\ell)$ plot is normalised by luminosity. The hashed band represents the experimental systematic uncertainties. 90

B.1 Pulls and constraints on the systematic uncertainties for the 2016, 2017 and 2018 data taking periods. 91

B.2 Impact of the leading nuisances of the combined fit ranked by $\hat{r}$ for T2tt_800_100. 92

B.3 Impact of the leading nuisances of the combined fit ranked by $\hat{r}$ for T2tt_800_100. 93

B.4 Correlation pattern of the systematic uncertainties after the combined fit. 94

List of Tables

1.1 SM particle masses and their electric charges [13]. 4

1.2 Chiral supermultiplets in the MSSM [26]. 14

1.3 Gauge supermultiplets in the MSSM [26]. 14

1.4 The MSSM particle content (with sfermion mixing for the first two families assumed to be negligible) [26]. 15

2.1 LHC beam parameters relevant for the peak luminosity [30]. 24

5.1 Parameters modifying σ_{p_T} in the covariance matrix for jets in bins of $|\eta|$, as well as parameters used for the covariance matrix of the unclustered energy. Values are given separately for simulation and data. 50

5.2 Selection criteria for electrons and muons. 56

5.3 Summary of the event selection. 59

5.4 Cut flow table for background yields combining all three years. 59

5.5 Definition of the signal regions on top of the preselection in Table 5.3. . 60

5.6 Definition of the control regions with respect to the preselection in Table 5.3. 61

5.7 Overview of systematic uncertainties. 62

5.8 Correlation pattern of the nuisances and rate parameters related to the background estimation procedures. The experimental uncertainties (JER, JEC, *b*-tagging, leptonSF etc.) are accounted for but not shown here. 79

5.9 Normalisation factors for the backgrounds extracted by the fit to data in the control regions for all years separately and combined, with the corresponding uncertainty assigned on the normalisation. 80

5.10 Upper bounds of the exclusion limits for Full Run 2 (this analysis), CMS 2016 data [53] and ATLAS 2016 data [73]. 85

Bibliography

[1] **ATLAS** Collaboration, "Observation of a new particle in the search for the Standard Model Higgs boson with the ATLAS detector at the LHC", *Phys. Lett.* **B716** (2012) 1–29, doi:10.1016/j.physletb.2012.08.020, arXiv:1207.7214.

[2] **CMS** Collaboration, "Observation of a New Boson at a Mass of 125 GeV with the CMS Experiment at the LHC", *Phys. Lett.* **B716** (2012) 30–61, doi:10.1016/j.physletb.2012.08.021, arXiv:1207.7235.

[3] **Planck** Collaboration, "Planck 2018 results. VI. Cosmological parameters", arXiv:1807.06209.

[4] D. Clowe et al., "A direct empirical proof of the existence of dark matter", *Astrophys. J.* **648** (2006) L109–L113, doi:10.1086/508162, arXiv:astro-ph/0608407.

[5] **Super-Kamiokande** Collaboration, "Evidence for oscillation of atmospheric neutrinos", *Phys. Rev. Lett.* **81** (1998) 1562–1567, doi:10.1103/PhysRevLett.81.1562, arXiv:hep-ex/9807003.

[6] **SNO** Collaboration, "Measurement of the rate of $\nu_e + d \to p + p + e^-$ interactions produced by ^8B solar neutrinos at the Sudbury Neutrino Observatory", *Phys. Rev. Lett.* **87** (2001) 071301, doi:10.1103/PhysRevLett.87.071301, arXiv:nucl-ex/0106015.

[7] E. Noether, "Invariant Variation Problems", *Gott. Nachr.* **1918** (1918) 235–257, doi:10.1080/00411457108231446, arXiv:physics/0503066. [Transp. Theory Statist. Phys.1,186(1971)].

[8] **UA1** Collaboration, "Experimental Observation of Isolated Large Transverse Energy Electrons with Associated Missing Energy at s**(1/2) = 540-GeV", *Phys. Lett.* **122B** (1983) 103–116, doi:10.1016/0370-2693(83)91177-2. [,611(1983)].

[9] **UA2** Collaboration, "Observation of Single Isolated Electrons of High Transverse Momentum in Events with Missing Transverse Energy at the CERN anti-p p Collider", *Phys. Lett.* **122B** (1983) 476–485, doi:10.1016/0370-2693(83)91605-2. [,7.45(1983)].

[10] **UA2** Collaboration, "Evidence for Z0 —> e+ e- at the CERN anti-p p Collider", *Phys. Lett.* **129B** (1983) 130–140, doi:10.1016/0370-2693(83)90744-X. [,7.69(1983)].

[11] **UA1** Collaboration, "Experimental Observation of Lepton Pairs of Invariant Mass Around 95-GeV/c**2 at the CERN SPS Collider", *Phys. Lett.* **126B** (1983) 398–410, doi:10.1016/0370-2693(83)90188-0. [,7.55(1983)].

[12] A. Zee, "Group Theory in a Nutshell for Physicists". Princeton University Press, USA, 2016.

[13] **Particle Data Group** Collaboration, "Review of Particle Physics", *Phys. Rev.* **D98** (2018), no. 3, 030001, doi:10.1103/PhysRevD.98.030001.

[14] D. J. Gross and F. Wilczek, "Ultraviolet Behavior of Nonabelian Gauge Theories", *Phys. Rev. Lett.* **30** (1973) 1343–1346, doi:10.1103/PhysRevLett.30.1343. [,271(1973)].

[15] H. D. Politzer, "Reliable Perturbative Results for Strong Interactions?", *Phys. Rev. Lett.* **30** (1973) 1346–1349, doi:10.1103/PhysRevLett.30.1346. [,274(1973)].

[16] W. N. Cottingham and D. A. Greenwood, "An introduction to the standard model of particle physics". Cambridge University Press, 2007.

[17] S. L. Glashow, "The renormalizability of vector meson interactions", *Nucl. Phys.* **10** (1959) 107–117, doi:10.1016/0029-5582(59)90196-8.

[18] A. Salam and J. C. Ward, "Weak and electromagnetic interactions", *Nuovo Cim.* **11** (1959) 568–577, doi:10.1007/BF02726525.

[19] S. Weinberg, "A Model of Leptons", *Phys. Rev. Lett.* **19** (1967) 1264–1266, doi:10.1103/PhysRevLett.19.1264.

[20] P. W. Higgs, "Broken Symmetries and the Masses of Gauge Bosons", *Phys. Rev. Lett.* **13** (1964) 508–509, doi:10.1103/PhysRevLett.13.508. [,160(1964)].

[21] F. Englert and R. Brout, "Broken Symmetry and the Mass of Gauge Vector Mesons", *Phys. Rev. Lett.* **13** (1964) 321–323, doi:10.1103/PhysRevLett.13.321. [,157(1964)].

[22] B. C. Odom, D. Hanneke, B. D'Urso, and G. Gabrielse, "New Measurement of the Electron Magnetic Moment Using a One-Electron Quantum Cyclotron", *Phys. Rev. Lett.* **97** (2006) 030801. [Erratum: Phys. Rev. Lett.99,039902(2007)].

[23] R. Massey, T. Kitching, and J. Richard, "The dark matter of gravitational lensing", *Rept. Prog. Phys.* **73** (2010) 086901, doi:10.1088/0034-4885/73/8/086901, arXiv:1001.1739.

[24] E. Corbelli and P. Salucci, "The Extended Rotation Curve and the Dark Matter Halo of M33", *Mon. Not. Roy. Astron. Soc.* **311** (2000) 441–447, doi:10.1046/j.1365-8711.2000.03075.x, arXiv:astro-ph/9909252.

[25] N. Padmanabhan and D. P. Finkbeiner, "Detecting dark matter annihilation with CMB polarization: Signatures and experimental prospects", *Phys. Rev.* **D72** (2005) 023508, doi:10.1103/PhysRevD.72.023508, arXiv:astro-ph/0503486.

[26] S. P. Martin, "A Supersymmetry primer", doi:10.1142/9789812839657_0001,10.1142/9789814307505_0001, arXiv:hep-ph/9709356. [Adv. Ser. Direct. High Energy Phys.18,1(1998)].

[27] D. Feldman, P. Fileviez Perez, and P. Nath, "R-parity Conservation via the Stueckelberg Mechanism: LHC and Dark Matter Signals", *JHEP* **01** (2012) 038, doi:10.1007/JHEP01(2012)038, arXiv:1109.2901.

[28] R. Barbier et al., "R-parity violating supersymmetry", *Phys. Rept.* **420** (2005) 1–202, doi:10.1016/j.physrep.2005.08.006, arXiv:hep-ph/0406039.

[29] W. Beenakker et al., "Stop production at hadron colliders", *Nucl. Phys.* **B515** (1998) 3–14, doi:10.1016/S0550-3213(98)00014-5, arXiv:hep-ph/9710451.

[30] O. S. Bruning et al., "LHC Design Report Vol.1: The LHC Main Ring", doi:10.5170/CERN-2004-003-V-1.

[31] **ATLAS** Collaboration, "The ATLAS Experiment at the CERN Large Hadron Collider", *JINST* **3** (2008) S08003, doi:10.1088/1748-0221/3/08/S08003.

[32] **CMS** Collaboration, "The CMS Experiment at the CERN LHC", *JINST* **3** (2008) S08004, doi:10.1088/1748-0221/3/08/S08004.

[33] **LHCb** Collaboration, "The LHCb Detector at the LHC", *JINST* **3** (2008) S08005, doi:10.1088/1748-0221/3/08/S08005.

[34] **ALICE** Collaboration, "The ALICE experiment at the CERN LHC", *JINST* **3** (2008) S08002, doi:10.1088/1748-0221/3/08/S08002.

[35] E. Mobs, "The CERN accelerator complex - August 2018. Complexe des accélérateurs du CERN - Août 2018",. General Photo.

[36] T. Sakuma and T. McCauley, "Detector and Event Visualization with SketchUp at the CMS Experiment", *J. Phys. Conf. Ser.* **513** (2014) 022032, doi:10.1088/1742-6596/513/2/022032, arXiv:1311.4942.

[37] **CMS** Collaboration, "CMS Technical Design Report Volume I: Detector Performance and Software",.

[38] **CMS** Collaboration, "CMS Technical Design Report Volume II: Physics performance", *J. Phys.* **G34** (2007), no. 6, 995–1579, doi:10.1088/0954-3899/34/6/S01.

[39] D. Barney, "CMS Detector Slice", (Jan, 2016). CMS Collection.

[40] M. Friedl, "The CMS Silicon Strip Tracker and its Electronic Readout". PhD thesis, Vienna University of Technology, 2001.

[41] **CMS** Collaboration, "Precise Mapping of the Magnetic Field in the CMS Barrel Yoke using Cosmic Rays", *JINST* **5** (2010) T03021, doi:10.1088/1748-0221/5/03/T03021, arXiv:0910.5530.

[42] **CMS** Collaboration, "Energy Calibration and Resolution of the CMS Electromagnetic Calorimeter in *pp* Collisions at $\sqrt{s} = 7$ TeV", *JINST* **8** (2013) P09009, doi:10.1088/1748-0221/8/09/P09009, arXiv:1306.2016. [JINST8,9009(2013)].

[43] V. D. Elvira, "Measurement of the Pion Energy Response and Resolution in the CMS HCAL Test Beam 2002 Experiment",.

[44] **USCMS, ECAL/HCAL** Collaboration, "The CMS barrel calorimeter response to particle beams from 2-GeV/c to 350-GeV/c", *Eur. Phys. J.* **C60** (2009) 359–373, doi:10.1140/epjc/s10052-009-0959-5,10.1140/epjc/s10052-009-1024-0. [Erratum: Eur. Phys. J.C61,353(2009)].

[45] **CMS** Collaboration, "Performance of CMS Muon Reconstruction in *pp* Collision Events at $\sqrt{s} = 7$ TeV", *JINST* **7** (2012) P10002, doi:10.1088/1748-0221/7/10/P10002, arXiv:1206.4071.

[46] **CMS** Collaboration, "Particle-flow reconstruction and global event description with the CMS detector", *JINST* **12** (2017), no. 10, P10003, doi:10.1088/1748-0221/12/10/P10003, arXiv:1706.04965.

[47] **CMS** Collaboration, "Description and performance of track and primary-vertex reconstruction with the CMS tracker", *JINST* **9** (2014), no. 10, P10009, doi:10.1088/1748-0221/9/10/P10009, arXiv:1405.6569.

[48] **CMS** Collaboration, "Performance of Electron Reconstruction and Selection with the CMS Detector in Proton-Proton Collisions at ?s = 8 TeV", *JINST* **10** (2015), no. 06, P06005, doi:10.1088/1748-0221/10/06/P06005, arXiv:1502.02701.

[49] M. Cacciari, G. P. Salam, and G. Soyez, "The anti-k_t jet clustering algorithm", *JHEP* **04** (2008) 063, doi:10.1088/1126-6708/2008/04/063, arXiv:0802.1189.

[50] **CMS** Collaboration, "Determination of Jet Energy Calibration and Transverse Momentum Resolution in CMS", *JINST* **6** (2011) P11002, doi:10.1088/1748-0221/6/11/P11002, arXiv:1107.4277.

[51] **CMS** Collaboration, "Jet energy scale and resolution performances with 13TeV data", (June, 2016).

[52] **CMS** Collaboration, "Identification of heavy-flavour jets with the CMS detector in pp collisions at 13 TeV", *JINST* **13** (2018), no. 05, P05011, doi:10.1088/1748-0221/13/05/P05011, arXiv:1712.07158.

[53] **CMS** Collaboration, "Search for top squarks and dark matter particles in opposite-charge dilepton final states at $\sqrt{s} = 13$ TeV", *Phys. Rev.* **D97** (2018), no. 3, 032009, doi:10.1103/PhysRevD.97.032009, arXiv:1711.00752.

[54] S. Alioli, P. Nason, C. Oleari, and E. Re, "NLO single-top production matched with shower in POWHEG: s- and t-channel contributions", *JHEP* **09** (2009) 111, doi:10.1007/JHEP02(2010)011,10.1088/1126-6708/2009/09/111, arXiv:0907.4076. [Erratum: JHEP02,011(2010)].

[55] E. Re, "Single-top Wt-channel production matched with parton showers using the POWHEG method", *Eur. Phys. J.* **C71** (2011) 1547, doi:10.1140/epjc/s10052-011-1547-z, arXiv:1009.2450.

[56] J. Alwall et al., "MadGraph 5 : Going Beyond", *JHEP* **06** (2011) 128, doi:10.1007/JHEP06(2011)128, arXiv:1106.0522.

[57] T. Sjöstrand et al., "An Introduction to PYTHIA 8.2", *Comput. Phys. Commun.* **191** (2015) 159–177, doi:10.1016/j.cpc.2015.01.024, arXiv:1410.3012.

[58] J. Alwall et al., "The automated computation of tree-level and next-to-leading order differential cross sections, and their matching to parton shower simulations", *JHEP* **07** (2014) 079, doi:10.1007/JHEP07(2014)079, arXiv:1405.0301.

[59] **CMS** Collaboration, "Performance of missing transverse momentum in pp collisions at sqrt(s)=13 TeV using the CMS detector",.

[60] C. G. Lester and D. J. Summers, "Measuring masses of semiinvisibly decaying particles pair produced at hadron colliders", *Phys. Lett.* **B463** (1999) 99–103, doi:10.1016/S0370-2693(99)00945-4, arXiv:hep-ph/9906349.

[61] **CMS** Collaboration, "Missing transverse energy performance of the CMS detector", *JINST* **6** (2011) P09001, doi:10.1088/1748-0221/6/09/P09001, arXiv:1106.5048.

[62] **CMS** Collaboration, "Performance of the CMS missing transverse momentum reconstruction in pp data at $\sqrt{s} = 8$ TeV", *JINST* **10** (2015), no. 02, P02006, doi:10.1088/1748-0221/10/02/P02006, arXiv:1411.0511.

[63] **CMS** Collaboration, "Pileup mitigation at CMS in 13 TeV data", arXiv:2003.00503.

[64] **CMS Collaboration** Collaboration, "Heavy flavor identification at CMS with deep neural networks",.

[65] **CMS** Collaboration, "Jet energy scale and resolution in the CMS experiment in pp collisions at 8 TeV", *JINST* **12** (2017), no. 02, P02014, doi:10.1088/1748-0221/12/02/P02014, arXiv:1607.03663.

[66] **CMS** Collaboration, "Measurement of Differential Top-Quark Pair Production Cross Sections in *pp* collisions at $\sqrt{s} = 7$ TeV", *Eur. Phys. J.* **C73** (2013), no. 3, 2339, doi:10.1140/epjc/s10052-013-2339-4, arXiv:1211.2220.

[67] **CMS** Collaboration, "Measurement of the differential cross section for top quark pair production in pp collisions at $\sqrt{s} = 8\,\text{TeV}$", *Eur. Phys. J.* **C75** (2015), no. 11, 542, doi:10.1140/epjc/s10052-015-3709-x, arXiv:1505.04480.

[68] N. Kidonakis, "NNLL threshold resummation for top-pair and single-top production", *Phys. Part. Nucl.* **45** (2014), no. 4, 714–722, doi:10.1134/S1063779614040091, arXiv:1210.7813.

[69] **CMS** Collaboration, "Measurement of top quark pair production in association with a Z boson in proton-proton collisions at $\sqrt{s} = 13$ TeV", arXiv:1907.11270.

[70] A. L. Read, "Presentation of search results: The CL(s) technique", *J. Phys.* **G28** (2002) 2693–2704, doi:10.1088/0954-3899/28/10/313. [,11(2002)].

[71] G. Cowan, K. Cranmer, E. Gross, and O. Vitells, "Asymptotic formulae for likelihood-based tests of new physics", *Eur. Phys. J.* **C71** (2011) 1554, doi:10.1140/epjc/s10052-011-1554-0,10.1140/epjc/s10052-013-2501-z, arXiv:1007.1727. [Erratum: Eur. Phys. J.C73,2501(2013)].

[72] T. Junk, "Confidence level computation for combining searches with small statistics", *Nucl. Instrum. Meth.* **A434** (1999) 435–443, doi:10.1016/S0168-9002(99)00498-2, arXiv:hep-ex/9902006.

[73] **ATLAS** Collaboration, "Search for direct top squark pair production in final states with two leptons in $\sqrt{s} = 13$ TeV *pp* collisions with the ATLAS detector", *Eur. Phys. J.* **C77** (2017), no. 12, 898, doi:10.1140/epjc/s10052-017-5445-x, arXiv:1708.03247.